UC San Diego

UC San Diego Electronic Theses and Dissertations

Title

Modeling and Control of Power Flow in Electrical Energy Storage and Delivery Systems

Permalink

https://escholarship.org/uc/item/5bt17944

Author

Zhao, Xin

Publication Date

2016

Peer reviewed|Thesis/dissertation

eScholarship.org Powered by the California Digital Library
University of California

UNIVERSITY OF CALIFORNIA, SAN DIEGO

Modeling and Control of Power Flow in Electrical Energy Storage and Delivery Systems

A Dissertation submitted in partial satisfaction of the
requirements for the degree
Doctor of Philosophy

in

Engineering Sciences (Mechanical Engineering)

by

Xin Zhao

Committee in charge:

Professor Raymond A. de Callafon, Chair
Professor Robert R. Bitmead
Professor Philip E. Gill
Professor Jan P. Kleissl
Professor Michael D. Todd

2016

Copyright
Xin Zhao, 2016
All rights reserved.

The Dissertation of Xin Zhao is approved, and it is acceptable in quality and form for publication on microfilm and electronically:

_____

_____

_____

_____

_____

Chair

University of California, San Diego

2016

DEDICATION

To my parents.

TABLE OF CONTENTS

LIST OF FIGURES

LIST OF TABLES

ACKNOWLEDGEMENTS

I would like to express my most sincere gratitude to my advisor Professor Raymond A. de Callafon for his continuous guidance and support throughout the years of my research in UC San Diego. Without his insightful and knowledgeable guidance as well as his patience and trust on me, I cannot complete my thesis research.

I also would like to express sincere appreciation to my doctoral dissertation committee members Professor Robert Bitmead, Professor Philip Gill, Professor Jan Kleissl, and Professor Michael Todd.

It is grateful that some parts of my research was financially supported by California Energy Commission (CEC). I would like to thank Program Director William Torre for his kind support and guidance.

Special thanks are to Mr. Lou Shrinkle, without whose support and mentoring I couldn't have an opportunity of working on an Electric Vehicle project that I love.

During the past few years, I was fortunate to have a few internship opportunities. I would like to thank Dr. Todd Evans, Dr. Wen Wu, Dr. Guoxiao Guo, Dr. Jianguo Zhou, and Mr. Khaled Hassounah for their kind support and mentoring during my internships in General Atomics, Western Digital Corp., and Ample Inc., respectively.

It is my fortune to meet all my lab mates here in UC San Diego, especially Dr. Huazhen Fang and Dr. Chad Holcomb. Their talent, insight, and dedication not only inspired me, but also led me through tough moments during research.

I also want to thank all my dear friends who cared about me and encouraged me through all the tough time, especially Dr. Kai Wang and Dr. Jun Li.

Last but not the least, my deepest appreciation is to my parents. Without

their unconditional love and support, I cannot be brave enough to overcome the obstacles I ever faced and become a better man.

Chapter 2 and Chapter 5, in part, are based on the material that appears in Proceedings of IFAC Symposium on System Identification (SYSID) 2015, Pages 63–68. Zhao, Xin; van de Ven, Maurice L. J.; de Callafon, Raymond A.; Torre, William. "Real-Time Demodulation of Real Power Oscillations." The dissertation author was the primary author of this paper.

Chapter 3, in part, is based on the material that appears in Proceedings of American Control Conference (ACC) 2013, Pages 1908–1913. Zhao, Xin; de Callafon, Raymond A.. "Data-based Modeling of a Lithium Iron Phosphate Battery as an Energy Storage and Delivery System." The dissertation author was the primary author of this paper.

Chapter 3, in part, is based on the material that appears in Applied Energy, vol. 180, Pages 823–833. Zhao, Xin; de Callafon, Raymond A.. "Modeling of Battery Dynamics and Hysteresis for Power Delivery Prediction and SOC Estimation." The dissertation author was the primary author of this paper.

Chapter 4, in part, is a reprint of the material as it appears in Proceedings of IFAC World Congress 2014, Pages 2112–2117. Zhao, Xin; de Callafon, Raymond A.; Shrinkle Lou. "Current Scheduling for Parallel Buck Regulated Battery Modules." The dissertation author was the primary author of this paper.

Chapter 5, in part, is based on the material that is currently being prepared for submission for publication. Zhao, Xin; Gwynn, Benjamin T.; de Callafon, Raymond A.; Torre, William. "Power Flow Disturbance Rejection Control on Micro-Grid." The dissertation author is the primary author of this paper.

VITA

2007	B.S. in Automotive Engineering, Tsinghua University, China
2010	M.S. in Power Engineering, Tsinghua University, China
2013	Research Intern, General Atomics, San Diego, USA
2014	Engineering Intern, Western Digital Corp., Irvine, USA
2015	Engineering Intern, Ample Inc., San Francisco, USA
2016	Doctor of Philosophy in Engineering Sciences (Mechanical Engineering), University of California, San Diego

PUBLICATIONS

Journal Publications

X. Zhao, R. A. de Callafon, "Modeling of battery dynamics and hysteresis for power delivery prediction and SOC estimation", *Applied Energy*, vol. 180, pp. 823-833, 2016.

B. Xia, X. Zhao, R. A. de Callafon, H. Garnier, T. Nguyen, C. Mi, "Accurate Lithium-ion battery parameter estimation with continuous-time system identification methods", *Applied Energy*, vol. 179, pp. 426-436, 2016.

Y. Jiang, X. Zhao, A. Valibeygi, R. A. de Callafon, "Dynamic prediction of power storage and delivery by data-based fractional differential models of a lithium iron phosphate battery", *Energies*, vol. 9 (8), pp. 590, 2016.

H. Fang, X. Zhao, Y. Wang, Z. Sahinoglu, T. Wada, S. Hara and R. A. de Callafon, "Improved adaptive state-of-charge estimation for batteries using a multi-model approach", *Journal of Power Sources*, vol. 254, pp. 258-267, 2014.

Conference Proceedings

B. Xia, X. Zhao, R. A. de Callafon, T. Nguyen, C. Mi, "Accurate battery parameter estimation with improved continuous time system identification methods", in *Proceedings of the 8th IEEE Energy Conversion Congress and Exposition (ECCE)*, to appear, 2016.

X. Zhao, M.L.J. van de Van, R. A. de Callafon, W. Torre, "Real-time demodulation of real power oscillations", in *Proceedings of the 17th IFAC Symposium on System Identification (SYSID)*, pp. 63-68, Beijing, China, Oct. 19-21, 2015.

X. Zhao, R. A. de Callafon, L. Shrinkle, "Current scheduling for parallel Buck regulated battery modules", in *Proceedings of the 19th IFAC World Congress*, pp. 2112-2117, Cape Town, South Africa, Aug. 24-29, 2014.

H. Fang, X. Zhao, Y. Wang, Z. Sahinoglu, T. Wada, S. Hara and R.A. de Callafon, "State-of-charge estimation for batteries: A multi-model approach", in *Proceedings of 2014 American Control Conference (ACC)*, pp. 2779-2785, Portland, USA, Jun. 4-6, 2014.

X. Zhao, R. A. de Callafon, "Data-based modeling of a Lithium Iron Phosphate battery as an energy storage and delivery system", in *Proceedings of 2013 American Control Conference (ACC)*, pp. 1908-1913, Washington D.C., USA, Jun. 17-19, 2013.

H. Fang, X. Zhao, R. A. de Callafon, "Agile bayesian filtering", in *Proceedings of the 52nd IEEE Conference on Decision and Control (CDC)*, pp. 7690-7695, Florence, Italy, Dec. 10-13, 2013.

ABSTRACT OF THE DISSERTATION

Modeling and Control of Power Flow in Electrical Energy Storage and Delivery Systems

by

Xin Zhao

Doctor of Philosophy in Engineering Sciences (Mechanical Engineering)

University of California, San Diego, 2016

Professor Raymond A. de Callafon, Chair

In order to meet emerging requirements for better utilization of electrical energy, some novel modeling and control approaches for battery systems and electric grids are proposed and validated in this dissertation.

To better utilize a single battery system, the energy delivery capability and available energy stored in the battery needs to be understood first. A battery modeling approach is proposed to characterize power delivery dynamics, given charge and discharge demand as an input, and also estimate the state-of-charge of a battery, not only in normal operating range, but also in extreme cases, such as battery over-

charging. The model is composed of separated voltage and current models. Several non-linear models, including Hammerstein model, open-circuit voltage characteristics, and Takacs hysteresis model, are combined in the voltage and the current model, respectively. The state-of-charge of the battery is estimated in a recursive optimization fashion. The parameterization and estimation methods of the model are described and validated on experimental data from a lithium iron phosphate cell.

Several individual battery systems are usually connected in parallel to expand the total capacity of a network. To coordinate the output of each battery system, three current scheduling strategies are proposed. Besides simultaneous and sequential discharge scheduling algorithms, a hybrid algorithm is formulated by solving a Quadratic Programming problem. The simulation results indicate the feasibility of the proposed scheduling algorithms and motivate the use of parallel connected battery modules despite changes in battery operating parameters. The simultaneous and sequential discharge scheduling algorithms are extended to power scheduling. A complete modular battery system for an experimental Electric Vehicle with the same topology is developed for future experimental validation and research.

Integrating inverters in battery systems or other DC sources is required when connecting to electric girds. To maintain the stability of the grid, disturbance rejection control aiming to mitigate fluctuations in AC power flow is studied based on an experimental setup created to mimic a local electric grid. Through demodulating real power oscillations, modeling of actuator and disturbance, and implementing controller designed by combining the internal model principle and optimal control, the feasibility of proposed control method is validated.

Chapter 1

Introduction

1.1 Electrical Energy Storage and Delivery System (EESDS)

In physics, energy is the capacity of an object to perform work. It is a property of objects which can be transferred to other objects or converted into different forms, but cannot be created or destroyed. As stated in the law of conservation of energy, the total energy of an isolated system is conserved over time. More importantly, it is pointed out by the second law of thermodynamics that the entropy of an isolated system always increases over time in a natural process. Therefore, it has been an everlasting challenge for human beings to "manually" utilize the energy, which means to discover existing natural processes of energy conversion and then organize all of them in a certain pattern so as to work for humans.

The development of human society highly depends on the capability of converting and utilizing energy. Energy exists everywhere in the nature, but in different

forms. Most energy forms cannot be applied directly to human's activities, therefore a medium is required. For instance, a human body is not able to perform photosynthesis to convert light energy into chemical energy that sustains organisms' activities, but can complete the process through digesting plants. Here, the plant is a medium.

In energetics, the concepts of primary energy and energy carrier, which is also referred to secondary energy, are proposed to better categorize and distinguish different energy forms in a process of energy utilization [1]. Primary energy is an energy form found in nature that has not been subjected to any conversion or transformation process; while secondary energy is an energy form which has been transformed from primary energy source.

A typical process of energy utilization is depicted as in Fig. 1.1. Energy generation, energy consumption, and energy storage are all processes of energy conversion. They are distinguished by their roles in the system: Energy generation converts primary energy to the secondary energy form utilized in the system; energy consumption converts the secondary energy to other energy forms that can work for humans; and energy storage buffers the gap between energy generation and energy consumption at a given time through the capability of storing extra energy and supplementing demanded energy when required. Energy storage can represent any process that has bidirectional energy conversion.

To better utilize energy, it is crucial to find an energy form that can be handled by humans. Since the fundamental principles of electricity generation were discovered by the British scientist Micheal Faraday during the 1820s and early 1830s [2], electrical energy is widely applied as a secondary energy till today due to its capability of being converted to other forms such as heat, light, motion, etc..

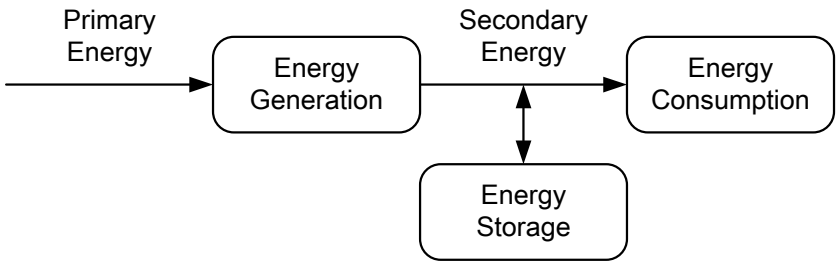

Figure 1.1: Diagram of an energy utilization process including energy generation, energy consumption, and energy storage.

For instance, an electric grid shown as in Fig. 1.2 is composed by all the components in an electrical energy utilization [3]. A Photo-Voltaic (PV) system acts as energy generation and converts solar energy to electrical energy. The generated electrical energy supplies eletrical loads such as households, factories, etc.. An energy storage system, which is usually a battery system or capacitor banks, buffers the energy gap with the supplement from the main grid. If the energy storage system is scaled well, then such local electrical energy system can be islanded from the main grid and form a stand-alone micro-grid [4].

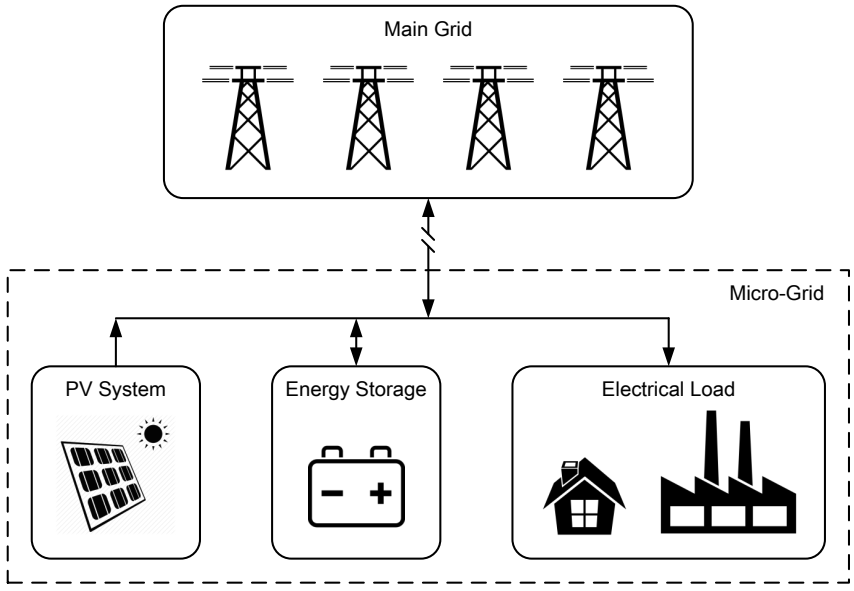

Figure 1.2: Diagram of a micro-grid including power generation via a Photo-Voltaic (PV) system, energy storage, and load.

Transportation is another application field of electrical energy. As shown in Fig. 1.3, the powertrain of a Battery Electric Vehicle (BEV) is composed by battery and electric drive [5, 6]. Electrical energy is provided by a charger, which is an interface to the electrical energy generation, and stored in a battery. When driving, the powertrain is disconnected from the charger, and then electric drive system transforms the electrical energy provided by battery to mechanical motion.

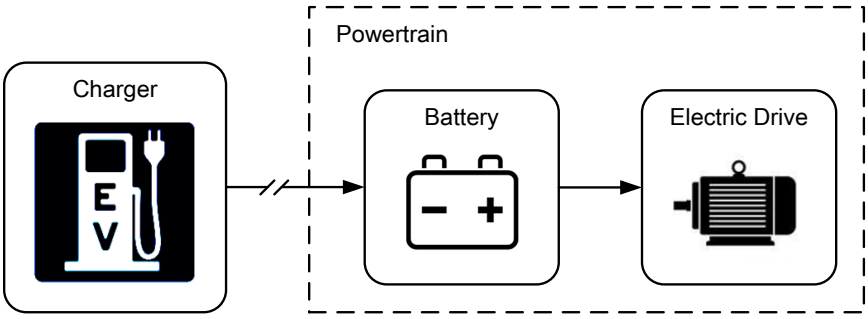

Figure 1.3: Diagram of the powertrain of a Battery Electric Vehicle.

Although each component in an electrical energy system is worth researching, in this dissertation an Electrical Energy Storage and Delivery System (EESDS) is of interest, which includes the storage and delivery process of electrical energy.

1.2 Motivating Problems

Electrification was one of significant marks of the Second Industrial Revolution in the final third of the 19th century and the beginning of the 20th. It used to be the cutting edge of research and engineering development back then. However, the well-established power industry, which is one of the main achievements in that period, has become more conservative over time due to stability concerns. After tremendous development of energy storage, power electronics, and communication technologies

[7, 8, 9, 10, 11], a requirement for reconstruction of the way of utilizing electrical energy arises at different levels from battery cells to an electric grid [12, 13]. A systematic view and solution is based on advanced control technology. After decades of development of modern control theory, the up-to-date control technology is ready to reshape the field of application of electrical energy.

In this dissertation, the modeling of a battery system is motivated by exploring the possibility of a modeling approach from a control prospective, which is different from conventional modeling approaches. The challenge aims at characterizing the power delivery capability of a battery system and also understanding the available energy remained in the system.

When connecting individual battery systems in parallel in a network, challenges arises for coordinating/scheduling the power output of each system especially when batteries may have different operating parameters such as state-of-charge (SoC), open-circuit voltage (OCV), internal resistance or battery chemistry.

By integrating inverters into a battery system or other DC sources, DC power flows are transformed to AC power flows in electric grids. To merge and distribute these flows smoothly, special care should be taken. Stability is required for different levels of electric network, therefore any feedback control aiming to mitigate or stabilize the power flow is of interest in research.

1.3 Summary of Contributions

In the dissertation, the research is dedicated to apply system identification technology, optimization algorithms, and optimal control methodology for better utilization of electrical energy in battery systems and electric grids. Several novel mod-

eling approaches and control strategies are proposed for battery modeling, current scheduling, and disturbance rejection control. Three sets of experimental setup are created for validating the proposed approaches and strategies, respectively. The following is a summary of the main contributions.

- **Battery Modeling:** A battery modeling approach is proposed aiming to predict power delivery dynamics, given charge and discharge demand as a control input, which is a different approaches from the conventional equivalent circuit models and electrochemical models. The state-of-charge of the battery can also be estimated in a recursive optimization fashion by the model. The model is composed of separated voltage and current models. Several non-linear models, including Hammerstein model, non-linear open-circuit voltage characteristics, and Takacs hysteresis model are combined in the voltage and the current model, respectively, to allow the model valid not only in normal operating range of batteries, but also in extreme cases, such as battery over-charging. The parameterization and estimation methods of the model are described and also demonstrated on experimental data from a lithium iron phosphate cell.

- **Current Scheduling:** Three current scheduling strategies are proposed for a parallel connection of battery modules integrating buck regulators in each module. Besides simultaneous and sequential discharge scheduling algorithms, a hybrid algorithm is formulated by solving a Quadratic Programming (QP) problem. The simulation results indicate the feasibility of the scheduling algorithms and motivate the use of parallel connected battery modules despite changes in battery operating parameters. It also motivates future research on applying optimization algorithms to scheduling of power flow.

- **Development of Modular Battery System:** A complete modular battery system for Electric Vehicle is developed. Each battery module integrates a Battery Management System (BMS) for real-time monitoring and charge balancing, and a buck regulator for controlling the power output. To execute real-time feedback control, a 2.4GHz wireless star network is integrated in the system with a base station collecting real-time information from each battery module and coordinating the output of each module. The developed system is the instrument for future research on battery modeling and power scheduling.

- **Disturbance Rejection Control:** A disturbance rejection control to mitigate the fluctuation of AC power flow by modulating (real) power via a controllable DC to AC inverter is demonstrated through implementation in an experimental setup. The experimental setup integrates a controllable grid-tied inverter (GTI), a three-phase Resistor-Inductor-Capacitor (RLC) network, sensors and an embedded controller. The created experimental setup is the instrument for future research on implementation of advanced control for power flow.

1.4 Organization

The remainder of the dissertation is organized as follows: Chapter 2 presents power definitions in DC power system, single-phase AC system, and three-phase AC system, which form the fundamental variables of interest in modeling and control of power flow. A real-time real power analysis is also given for demodulating real power oscillations; Chapter 3 proposes and validates a modeling approach for a single battery system as an Electrical Energy Storage System to predict power delivery dynamics

and to estimate state-of-charge of it; Chapter 4 proposes and simulates three current scheduling strategies for a parallel-connected battery systems to coordinate the output of each individual system, and shows the design of such a battery system called M-BEAM for an experimental Electric Vehicle; Chapter 5 proposes and validates a disturbance rejection control to mitigate the fluctuation of AC power flow; Chapter 6 concludes this thesis and provides suggestions on future research.

Chapter 2

Power Definitions and Power Flow

In power engineering, electric power is defined based on voltage and current. Voltage is the difference in electric potential between two points in an electrical system. Current is a flow of electric charge.

Conventionally, explaining the flow of electrical energy from source to load also relies on the flow of electric charges. It is usually visualized by the movement of a large amount of particles, which is also seen in the explanation of fluid flow in fluid dynamics. A major drawback of this model becomes apparent when we try to explain the situations where the energy is stored in, or transferred through, dielectrics immersed in alternating electromagnetic fields [14].

Engineers dealing with antennae, microwaves, and other high frequency applications utilize a more advanced explanation based on the representation of the rate of flow of the energy density at any point in space by means of Poynting vector

$$\overrightarrow{\mathscr{P}} = \overrightarrow{E} \times \overrightarrow{H}, \tag{2.1}$$

where $\overrightarrow{E}$ and $\overrightarrow{H}$ are the electric and magnetic field vectors at the considered point.

As stated in Section 1.2, this dissertation aims to solve some problems from a control perspective. It means that the definitions presented in this chapter are only used to form the variable/signal of interest in a modeling or control problem. Therefore, some commonly-used power definitions in power engineering are summarized in order to form the fundamental for the problems to be solved in the rest of the dissertation.

2.1 DC Power Flow

In a Direct Current (DC) system, the instantaneous power is defined as

$$p_{\mathrm{DC}}(t) = v_{\mathrm{DC}}(t) \cdot i_{\mathrm{DC}}(t). \tag{2.2}$$

Since the polarity of voltage $v_{\mathrm{DC}}(t)$ is invariant, the direction of DC power flow, which is usually indicated by the sign of $p_{\mathrm{DC}}(t)$, only depends on the direction of current $i_{\mathrm{DC}}(t)$.

2.2 AC Power Flow

In an Alternating Current (AC) system, the power definition becomes more complicated. In this section, the power definitions mainly follow IEEE Std. 1459-2010 [15]. In the standard, the power definitions are categorized into three components: apparent power, active power, and non-active power. One may refer to [14] for more background introduction and discussions about the standard. In the power definition

for three-phase AC system, the instantaneous reactive power p-q theory is introduced, since it provides an alternative to explain the physical mechanism of power flow in this case.

2.2.1 Single-Phase AC Power

Single-Phase Sinusoidal Case

A sinusoidal voltage source

$$v = \sqrt{2}V \sin(\omega t) \tag{2.3}$$

supplying a linear load will produce a sinusoidal current (assumed lagging the voltage) of

$$i = \sqrt{2}I \sin(\omega t - \theta), \tag{2.4}$$

where

V is the root-mean-square (RMS) value of the voltage (V);

I is the RMS value of the current (A);

ω is the angular frequency $2\pi f$ (rad/s);

f is the fundamental power system frequency (Hz);

θ is the phase angle between the current and the voltage (rad);

t is the time (s).

Then the active power is defined as

$$P = VI \cos\theta. \tag{2.5}$$

The reactive power is defined as

$$Q = VI \sin\theta. \tag{2.6}$$

The apparent power is defined as

$$S = VI. \tag{2.7}$$

Moreover, the complex power is a complex quantity in which the active power is the real part and the reactive power is the imaginary part

$$\mathbf{S} = P + jQ = \vec{\mathbf{V}}\vec{\mathbf{I}}^*, \tag{2.8}$$

where

$\vec{\mathbf{V}}$ is the voltage phasor;

$\vec{\mathbf{I}}^*$ is the complex conjugate of the current phasor.

In particular, the voltage phasor for (2.3) is

$$\begin{aligned} & v(t) = \sqrt{2}V \sin(\omega t) = \sqrt{2}V \cos(\omega t - \frac{\pi}{2}) \\ \Leftrightarrow \quad & \vec{\mathbf{V}} = Ve^{j\cdot(-\frac{\pi}{2})} = V[\cos(-\frac{\pi}{2}) + j\sin(-\frac{\pi}{2})], \end{aligned} \tag{2.9}$$

and the current phasor for (2.4) is

$$\begin{aligned} & i(t) = \sqrt{2}I \sin(\omega t - \theta) = \sqrt{2}I \cos(\omega t - \frac{\pi}{2} - \theta) \\ \Leftrightarrow \quad & \vec{\mathbf{I}} = Ie^{j\cdot(-\frac{\pi}{2}-\theta)} = V[\cos(-\frac{\pi}{2} - \theta) + j\sin(-\frac{\pi}{2} - \theta)]. \end{aligned} \tag{2.10}$$

One may refer to [16] for more details about the phasor representation and its appli-

cation in electric grids.

Single-Phase Nonsinusoidal Case

For steady-state conditions, a nonsinusoidal periodical instantaneous voltage or current has two distinct components: the power system frequency components v_1 and i_1 and the remaining term v_H and i_H, respectively.

$$\begin{aligned} v &= v_1 + v_H, \\ i &= i_1 + i_H, \end{aligned} \tag{2.11}$$

where

$$\begin{aligned} v_1 &= \sqrt{2V_1}\sin(\omega t \alpha_1); \\ i_1 &= \sqrt{2I_1}\sin(\omega t \beta_1); \\ v_H &= V_0 + \sqrt{2}\sum_{h\neq 1} V_h \sin(h\omega t - \alpha_h); \\ i_H &= I_0 + \sqrt{2}\sum_{h\neq 1} I_h \sin(h\omega t - \beta_h). \end{aligned} \tag{2.12}$$

The corresponding RMS values squared are as follows:

$$\begin{aligned} V^2 &= V_1^2 + V_H^2, \\ I^2 &= I_1^2 + I_H^2, \end{aligned} \tag{2.13}$$

where

$$\begin{aligned} V_H^2 &= V_0^2 + \sum_{h\neq 1} V_H^2, \\ I_H^2 &= I_0^2 + \sum_{h\neq 1} I_H^2, \end{aligned} \tag{2.14}$$

are the squares of the RMS values of v_H and i_H, respectively.

The active power is then defined as

$$P = P_1 + P_H, \tag{2.15}$$

where

the fundamental active power $P_1 = V_1 I_1 \cos\theta_1$;

the harmonic active power $P_H = V_0 I_0 + \Sigma_{h\neq 1}(V_h I_h \cos\theta_h)$.

The fundamental reactive power is defined as

$$Q_1 = V_1 I_1 \sin\theta_1. \tag{2.16}$$

The apparent power is defined as

$$S = VI. \tag{2.17}$$

2.2.2 Three-Phase AC Power

The complicated case scenarios, e.g. three-phase nonsinusoidal and unbalanced case, are out of scope of this dissertation. Therefore only the simplest case, i.e. three-phase sinusoidal balanced case, is presented in this section.

Three-Phase Sinusoidal Balanced Case

In this case assuming a counterclockwise rotating positive-sequence system, a, b, c, the line-to-neutral voltages are as follows:

$$\begin{aligned} v_a &= \sqrt{2}V\sin(\omega t); \\ v_b &= \sqrt{2}V\sin(\omega t - 120^\circ); \\ v_c &= \sqrt{2}V\sin(\omega t + 120^\circ). \end{aligned} \tag{2.18}$$

The line currents have similar expressions, and they are as follows:

$$\begin{aligned} i_a &= \sqrt{2}I\sin(\omega t - \theta); \\ i_b &= \sqrt{2}I\sin(\omega t - \theta - 120^\circ); \\ i_c &= \sqrt{2}I\sin(\omega t - \theta + 120^\circ). \end{aligned} \tag{2.19}$$

Then the active power is defined as

$$P = 3VI\cos\theta = \sqrt{3}V_{ll}I\cos\theta, \tag{2.20}$$

where

V is line-to-neutral RMS voltage in a four-wire system;

V_{ll} is line-to-line RMS voltage in a three-wire system.

The reactive power is defined as

$$Q = 3VI\sin\theta = \sqrt{3}V_{ll}I\sin\theta. \tag{2.21}$$

The apparent power is defined as

$$P = 3VI = \sqrt{3}V_{ll}I. \tag{2.22}$$

Instantaneous Reactive Power *p-q* Theory

In 1982, Akagi et al. proposed the concept of instantaneous active and reactive power [17]. Later it is formulated into a comprehensive instantaneous power theory, which is usually called "*p-q* Theory", and widely applied in power conditioning [18].

The *p-q* Theory is based on a set of instantaneous power defined in the time domain. No restrictions are imposed on the voltage or current waveforms, and it can be applied to three-phase systems with or without a neutral wire for three-phase generic voltage and current waveforms. Thus, it is not only in the steady state, but also in the transient state. The significant difference of the *p-q* Theory from other traditional concepts of power is that it treats the three-phase system as a whole, not a superposition or sum of three single-phase circuits.

For different power systems, the definition of the instantaneous power is slightly different with respect to voltage and current components. Here the *p-q* Theory applied in three-phase, four-wire systems is given as an example to illustrate a typical procedure of obtaining instantaneous power components.

First, the three-phase instantaneous voltages in the *abc* phases, v_a, v_b, and v_c, are mapped into the instantaneous voltages on the $\alpha\beta$0-axes, v_α, v_β, and v_0, via the

$\alpha\beta 0$ transformation, or so-called Clarke transformation:

$$\begin{bmatrix} v_0 \\ v_\alpha \\ v_\beta \end{bmatrix} = \sqrt{\frac{2}{3}} \begin{bmatrix} \frac{1}{\sqrt{2}} & \frac{1}{\sqrt{2}} & \frac{1}{\sqrt{2}} \\ 1 & -\frac{1}{2} & -\frac{1}{2} \\ 0 & \frac{\sqrt{3}}{2} & -\frac{\sqrt{3}}{2} \end{bmatrix} \begin{bmatrix} v_a \\ v_b \\ v_c \end{bmatrix}. \tag{2.23}$$

Similarly, three-phase generic instantaneous line currents, i_a, i_b, and i_c, can be transformed on the $\alpha\beta 0$ axes by

$$\begin{bmatrix} i_0 \\ i_\alpha \\ i_\beta \end{bmatrix} = \sqrt{\frac{2}{3}} \begin{bmatrix} \frac{1}{\sqrt{2}} & \frac{1}{\sqrt{2}} & \frac{1}{\sqrt{2}} \\ 1 & -\frac{1}{2} & -\frac{1}{2} \\ 0 & \frac{\sqrt{3}}{2} & -\frac{\sqrt{3}}{2} \end{bmatrix} \begin{bmatrix} i_a \\ i_b \\ i_c \end{bmatrix}. \tag{2.24}$$

Then three instantaneous powers, the instantaneous zero-sequence power p_0, the instantaneous real power p, and the instantaneous imaginary power q, are defined from the instantaneous phase voltages and line currents on the $\alpha\beta 0$ axes as

$$\begin{bmatrix} p_0 \\ p \\ q \end{bmatrix} = \begin{bmatrix} v_0 & 0 & 0 \\ 0 & v_\alpha & v_\beta \\ 0 & v_\beta & -v_\alpha \end{bmatrix} \begin{bmatrix} i_0 \\ i_\alpha \\ i_\beta \end{bmatrix}. \tag{2.25}$$

The three-phase instantaneous active power is defined as

$$p_{3\phi} = v_a i_a + v_b i_b + v_c i_c = v_\alpha i_\alpha + v_\beta i_\beta + v_0 i_0 = p + p_0. \tag{2.26}$$

The physical meaning of all the instantaneous powers is depicted in Fig. 2.1 and summarized as follows:

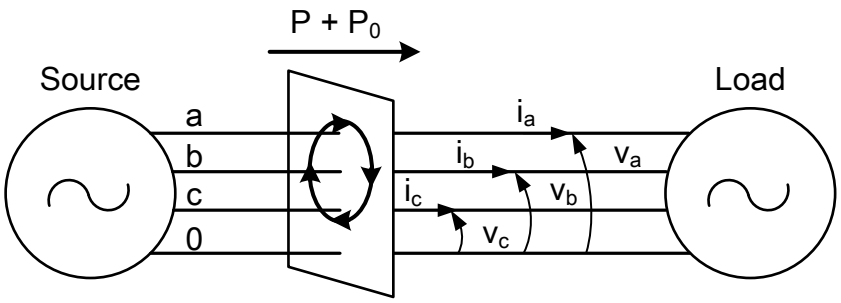

Figure 2.1: Physical meaning of the instantaneous powers defined in the *abc* reference frame.

- Zero-sequence components in the fundamental voltage and current and/or in the harmonics do not contribute to the real power p or to the imaginary power q.

- The total instantaneous energy flow per time unit, that is, the three-phase instantaneous active power, even in a distorted and unbalanced system, is always equal to the sum of the real power and the zero-sequence power ($p_{3\phi} = p + p_0$), and may contain average and oscillating parts.

- The imaginary power q, independent of the presence of harmonic or unbalances, represents the energy quantity that is being exchanged between the phases of the system. This means tht the imaginary power does not contribute to energy transfer between the source and the load at any time.

Although the p-q Theory is not perfect in terms of interpretation of some power phenomena, it is still very useful as long as it is applied for a control algorithm [19]. This also indicates that control algorithm can be designed as long as a specific set of power definitions is given as the control objective.

2.3 Real-Time Real Power Analysis

For control or mitigation of real or complex power oscillations, special care should be given to the time varying nature of the moving average values of the power signals. In the following discussion, the time varying behavior of the power signals can be derived as a multiplication of the AC grid frequency $\omega = 2\pi f$, $f = 60$Hz and the oscillations due to power fluctuations that may have a smaller oscillation frequency $f_d < f$. For real-time control, only the power oscillations with the frequency $f_d < f$ are of interest and detection of these power oscillations requires a demodulation of the power signals.

2.3.1 Analysis of Transient Effects

For the analysis of the transient effect, it is assumed that the three-phase voltage signals are time synchronized according to

$$v_A(t) = V\cos(\omega t) \tag{2.27}$$

$$v_B(t) = V\cos(\omega t - \frac{2}{3}\pi) \tag{2.28}$$

$$v_C(t) = V\cos(\omega t - \frac{4}{3}\pi). \tag{2.29}$$

and higher order harmonics are ignored initially, to simplify the analysis. It will be shown that low pass filtering is used to reduce the effect of higher harmonics on the 3 phase AC voltage and current signals.

A three-phase symmetric RLC circuit is used in this section to serve as a case study for the power oscillations and is used in the derivation of the results. Based on second order linear time-variant (LTI) dynamics of an RLC circuit, the transient

effects in the current signals can be represented by

$$\begin{aligned} i_A(t) &= I\cos(\omega t-\alpha)+I_d^A e^{\lambda t}\cos(\omega_d t-\beta) \\ & \quad I_d^A = I_d\cos(\omega t_d) \\ i_B(t) &= I\cos(\omega t-\alpha-\tfrac{2}{3}\pi)+I_d^B e^{\lambda t}\cos(\omega_d t-\beta) \\ & \quad I_d^B = I_d\cos(\omega t_d-\tfrac{2}{3}\pi) \\ i_C(t) &= I\cos(\omega t-\alpha-\tfrac{4}{3}\pi)+I_d^C e^{\lambda t}\cos(\omega_d t-\beta) \\ & \quad I_d^C = I_d\cos(\omega t_d-\tfrac{4}{3}\pi) \end{aligned}$$

where $\omega_d = 2\pi f_d < \omega$ is the (damped) oscillation frequency of the (power) transient with a phase shift of β and an exponential decay $\lambda < 0$. It should be noted that due to the three phase time synchronization, each current signal has a different initial condition I_d^A, I_d^B and I_d^C.

Taking Phase A as an example, the instantaneous power $p_A(t) = v_A(t)i_A(t)$ can now be written as

$$\begin{aligned} p_A(t) &= VI\cos(\omega t)\cos(\omega t-\alpha) \\ & \quad +VI_d\cos(\omega t_d)e^{\lambda t}\cos(\omega t)\cos(\omega_d t-\beta) \\ &= \tfrac{VI}{2}\cos\alpha+\tfrac{VI}{2}\cos(2\omega t-\alpha) \\ &+ \tfrac{VI_d}{2}\cos(\omega t_d)e^{\lambda t}\cos((\omega-\omega_d)t+\beta) \\ &+ \tfrac{VI_d}{2}\cos(\omega t_d)e^{\lambda t}\cos((\omega+\omega_d)t-\beta) \end{aligned} \tag{2.30}$$

showing the mixed effects of both the AC frequency ω and the transient oscillation frequency ω_d. The AC frequency ω may be known, but the (damped) oscillation frequency $\omega_d < \omega$ with its exponential decay λ may be unknown and need to be observed from real-time measurements of the AC power for dynamic modeling and

control purposes.

2.3.2 Demodulation of Single-Phase Real Power Oscillations

Modulating the instantaneous power of Phase A obtained from (2.30) with $\cos(\omega t)$ results in an expression for $p_A(t)\cos(\omega t)$ given by

$$\begin{aligned}
&\tfrac{VI}{2}\cos\alpha\cos(\omega t)\\
&+\tfrac{VI}{2}\cos(2\omega t-\alpha)\cos(\omega t)\\
&+\tfrac{VI_d}{2}\cos(\omega t_d)e^{\lambda t}\cos((\omega-\omega_d)t+\beta)\cos(\omega t)\\
&+\tfrac{VI_d}{2}\cos(\omega t_d)e^{\lambda t}\cos((\omega+\omega_d)t-\beta)\cos(\omega t)
\end{aligned} \tag{2.31}$$

where $\cos(\omega t) = v(t)/V$ can be obtained from (2.27). Using trigonometric identities, the expression for $p_A(t)\cos(\omega t)$ in (2.31) can be reorganized to

$$\begin{aligned}
&\tfrac{VI}{2}\cos\alpha\cos(\omega t)\\
&+\tfrac{VI}{4}\cos(\omega t-\alpha)+\tfrac{VI}{4}\cos(3\omega t-\alpha)\\
&+\tfrac{VI_d}{2}\cos(\omega t_d)e^{\lambda t}\cos(\omega_d t-\beta)\\
&+\tfrac{VI_d}{4}\cos(\omega t_d)e^{\lambda t}\cos((2\omega-\omega_d)t+\beta)\\
&+\tfrac{VI_d}{4}\cos(\omega t_d)e^{\lambda t}\cos((2\omega+\omega_d)t-\beta)
\end{aligned} \tag{2.32}$$

From (2.32) it is clear that by computing a moving average over a single period of $\frac{2\pi}{\omega}$, the first three cosine terms in (2.32) reduce to zero. Moving average filtering can be implemented in real-time using a discrete-time Finite Impulse Response (FIR) filter $F_{FIR}(q)$. The last two terms have a frequency $2\omega \pm \omega_d$ and do not reduce to zero with a moving average, but since $2\omega \pm \omega_d > \omega_d$, these terms can be reduced significantly by a discrete-time low pass filter $F_{LP}(q)$ with a cut-off frequency just above ω. Low pass

filtering will also reduce any higher harmonics that may be present on the 3 phase voltage and current signals. Hence, through filtering and modulation, a power signal $P_{dA}(t) = F(q)p_A(t)\cos(\omega t)$ is obtained that can be approximated by

$$A_F(\omega_d) \cdot \frac{VI_d}{2}\cos(\omega t_d)e^{\lambda t}\cos(\omega_d t - \beta + \phi(\omega_d)) \tag{2.33}$$

where $F(q) = F_{FIR}(q)F_{LP}(q)$ is the discrete-time filter combination of the FIR filter and a low-pass filter as described above, $A_F(\omega_d)$ and $\phi(\omega_d)$ are the gain and the phase shift of filter $F(q)$ at the frequency ω_d, respectively. For the other two phases, the same procedure can be applied to obtain the modulated real power $P_{dB}(t)$ for phase B given by

$$A_F(\omega_d) \cdot \frac{VI_d}{2}\cos(\omega t_d - \frac{2}{3}\pi)e^{\lambda t}\cos(\omega_d t - \beta + \phi(\omega_d)) \tag{2.34}$$

and the modulated real power $P_{dC}(t)$ for phase C as

$$A_F(\omega_d) \cdot \frac{VI_d}{2}\cos(\omega t_d - \frac{4}{3}\pi)e^{\lambda t}\cos(\omega_d t - \beta + \phi(\omega_d)) \tag{2.35}$$

The modulated real power signals for each phase can now be used to compute the three-phase real power oscillations.

2.3.3 Reconstruction of Three-Phase Real Power Oscillations

Applying the Clarke transformation to single-phase components obtained from (2.33), (2.34) and (2.35), the phasors are projected onto a decoupled coordinate $\alpha - \beta$

given by

$$\begin{bmatrix} P_\alpha(t) \\ P_\beta(t) \end{bmatrix} = \frac{2}{3} \begin{bmatrix} 1 & -\frac{1}{2} & -\frac{1}{2} \\ 0 & \frac{\sqrt{3}}{2} & -\frac{\sqrt{3}}{2} \end{bmatrix} \begin{bmatrix} P_{dA}(t) \\ P_{dB}(t) \\ P_{dC}(t) \end{bmatrix} =$$

$$A_F(\omega_d) \cdot \tfrac{VI_d}{2} e^{\lambda t} \cos(\omega_d t - \beta + \phi(\omega_d)) \begin{bmatrix} \cos(\omega t_d) \\ \sin(\omega t_d) \end{bmatrix}.$$

Then it can be seen that $P_\alpha(t)^2 + P_\beta(t)^2$ satisfies

$$\left[A_F(\omega_d) \cdot \tfrac{VI_d}{2} e^{\lambda t} \cos(\omega_d t - \beta + \phi(\omega_d)) \right]^2$$

In practice, the direction of real power is usually *a priori* knowledge. As such, the three-phase real power oscillation can be reconstructed from the demodulated single-phase components.

2.4 Acknowledgment

Chapter 2, in part, is based on the material that appears in Proceedings of IFAC Symposium on System Identification (SYSID) 2015, Pages 63–68. Zhao, Xin; van de Ven, Maurice L. J.; de Callafon, Raymond A.; Torre, William. "Real-Time Demodulation of Real Power Oscillations." The dissertation author was the primary author of this paper.

Chapter 3

Modeling of Battery System

3.1 Introduction

Electrical energy storage system (EESS) is fundamental and crucial in an electric power system [9]. Since the generated electrical energy is hardly equal to the energy consumed at a given time, an EESS is needed to buffer gaps in energy delivery. With the proliferation of distributed renewable energy resources such as photo-voltaic (PV) plants, more intermittent power is produced [20]. An EESS is utilized to store extra energy generated by a PV power plant and then supplement the demand from electric loads as required, as depicted in Fig. 1.2.

The power flow scheduling of EESS can be controlled by controllable inverters, as shown in Fig. 3.1. A local power system can be islanded and become a micro-grid when the energy capacity and power storage/delivery capability of local EESS are scaled properly to eliminate the power demand from the main electrical grid [21, 13].

Battery banks are often utilized as an EESS to store and supply extra energy. When a battery system is operating, the available peak power at a given time, which

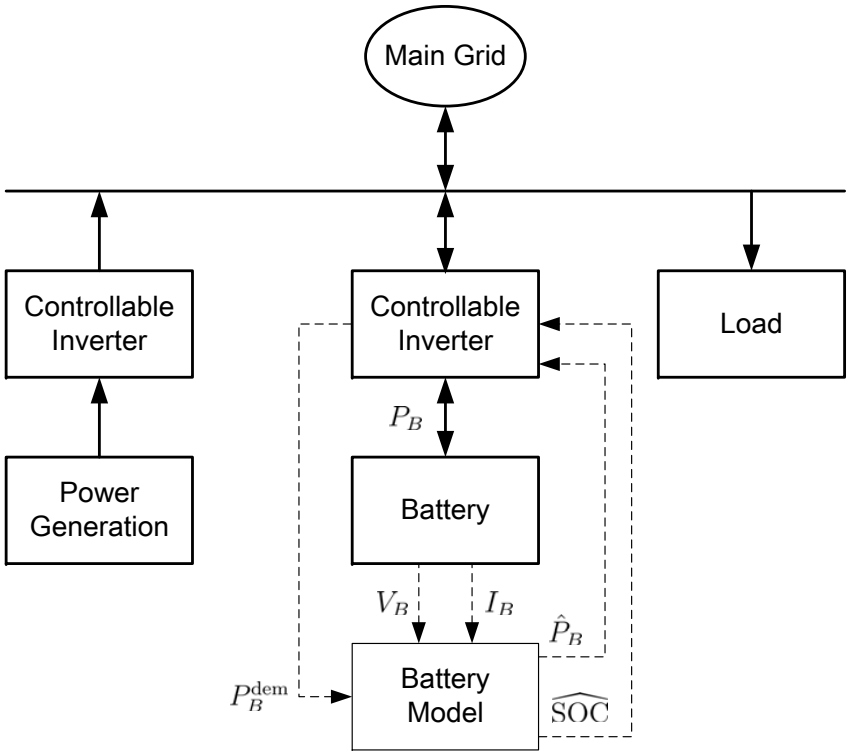

Figure 3.1: The functionality of the battery model is to predict power delivery dynamics and estimate SOC given charge and discharge demand.

is also called state of power (SOP), is monitored to evaluate the maximum charge and discharge capability of the battery [22, 23]. The increasing demand of batteries and more efficient usage of battery systems requires to not only passively monitor the status, but also actively, dynamically control the storage and delivery processes of EESS. Particularly, the dynamic power output capability of a battery system given power demand is of interest in terms of the performance optimization [24, 25, 26]. Therefore, it is necessary to have a dynamic power storage and delivery model of battery.

A battery is a complicated system due to its internal electrochemical processes, which behave significant nonlinear dynamics. Major modeling approaches used to describe nonlinear dynamics of batteries can be categorized in electrochemical models

and equivalent circuit models (ECM).

The electrochemical modeling approaches of batteries are based on first principles. In electrochemical models, a system of partial differential equations describes the internal physical and chemical processes of batteries. A well-known electrochemical model for Li-ion batteries is developed by Doyle, Fuller, and Newman (DFN) [27, 28]. Forman et al. identified the full set of DFN model parameters from cycling data using a genetic algorithm (GA) [29]. Though accurate estimation can be obtained, electrochemical models are difficult to be implemented, especially in applications that require a battery management system (BMS) or real-time control due to the complexity. To overcome such obstacle, simplified electrochemical models such as single particle model (SPM) have been studied in the literature [30, 31]. However, the required computational effort still makes simplified electrochemical models not easy to be implemented in low-cost BMS for online estimation [32].

The ECM eases the implementation difficulty of a battery model. An ECM aims to model a battery system originating from its electric characteristics, which results in a lumped model consisting of a resistance-capacitance (RC) network, static open-circuit voltage (OCV), and hysteresis [33].

The RC network in an ECM describes the diffusion impedance, which can also be interpreted as the linear dynamics of a battery. First-order and second-order RC models are usually utilized in practice [33, 34, 35], although essentially infinite RC ladder elements are required to obtain an accurate model [36]. A feasible approach to bypass high-order RC network is to integrate a fractional-order model into ECM [37, 38].

The behavior of OCV is commonly utilized to describe the remaining non-

linear dynamics of a battery. The measured OCV characteristics through off-line tests can be either applied through a look-up table [33], or described by mathematical forms [39]. Since OCV highly depends on the state of charge (SOC) of a battery, it is crucial to estimate SOC in real-time applications. Extensive research has been conducted to SOC estimation of batteries and the reader may refer to [40] for a survey. A single model can be employed for SOC estimation [41, 42], and multiple-models can also be utilized by fusing the estimation of each one to achieve accurate results [43, 44].

Besides static OCV characteristics, prominent hysteretic phenomena is also observed in nickel-metal-hydride (NiMH) and lithium iron phosphate ($LiFePO_4$) batteries [45]. The hysteresis of batteries depends on the latest short term history of charge and discharge, SOC, and also SOH [46]. Simple hysteresis models of battery can be achieved by curve fitting [47] or integrating a simple one-state hysteresis model [48]. In addition, general hysteresis models, such as Preisach model and Takacs model, have been applied in modeling of battery hysteresis to obtain more robust and precise estimation. The Preisach model consists of a finite number of parallel-connected independent relay hysterons, which provides corresponding high degrees of freedom to describe hysteretic effect. Tang et al. proposed a discrete Preisach model for NiMH battery [49]. Zhu et al. employed a Preisach model for $LiFePO_4$ with an adaptive estimation [50]. Another group of hysteresis models is developed by Takacs [51]. It was successfully applied to describe hysteresis effect seen in magnetic field over materials [52, 53]. The Takacs hysteresis model is especially useful when describing significant hysteretic phenomena. For instance, Windarko and Choi employed it in the modeling of NiMH battery's major hysteresis loop [54]. However, [50] claimed that it was not suitable to describe minor hysteresis loops using the Takacs model. One of the main

contributions of this paper is that we are able to use the Takacs hysteresis model to describe minor hysteresis loops seen during charging and discharging of a $LiFePO_4$ battery.

The specific linear dynamics, static OCV characteristics, and non-linear hysteresis effects revealed by the battery models introduced above are crucial and fundamental for describing voltage and current characteristics seen in a battery. Different modeling approaches of battery dynamics can be achieved or initialized by properly integrating those dynamic models.

3.2 Problem Formulation

In this dissertation, a battery modeling approach is proposed from a control system perspective. In particular, the power delivery dynamics of a battery system with an input of charge and discharge demand is modeled. The proposed approach is different from the conventional ECM or electrochemical models, as the power delivery dynamics, not the current-voltage dynamics, is of interest. The model aims to not only model how fast a battery can store and deliver energy as a function of time, but also provide the potential of controlling a battery system as an electrical energy storage and delivery system.

3.3 Experimental Setup

To validate and demonstrate the proposed modeling approach, an experimental setup is created where a charge/discharge demand signal can be applied while measuring the voltage and the current of the battery in real time. The schematic is

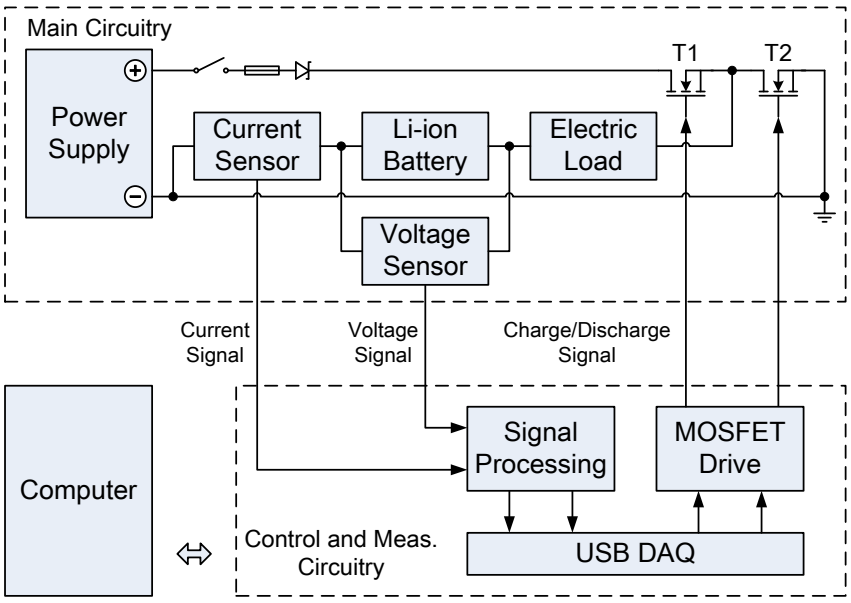

Figure 3.2: Schematic of the experimental setup.

shown as in Fig. 3.2.

In the main circuitry, the charge/discharge cycles are directed by the MOSFETs T_1 and T_2. Fast switching of the MOSFETS is driven by high-side and low-side drivers with proper bias and signal isolation, respectively. These MOSFETs applied in the tester are power MOSFETs with low drain-to-source on-resistance that is suitable for high current flow. When T_1 is turned on and T_2 is off, the battery is connected to the power supply and charged. While T_1 is turned off and T_2 is on, the battery is disconnected with the power supply and discharged. The MOSFETs are switched by the corresponding control signals sent from a National Instruments USB DAQ device. The DAQ device is also employed to acquire the measured signals, and it can communicate with the computer via USB cable. In the computer, a LabVIEW program is developed to automatically load cycle signals from existing files and save measured signals. Thus the test can be repeated using the same time sequence of charge/discharge demand signals.

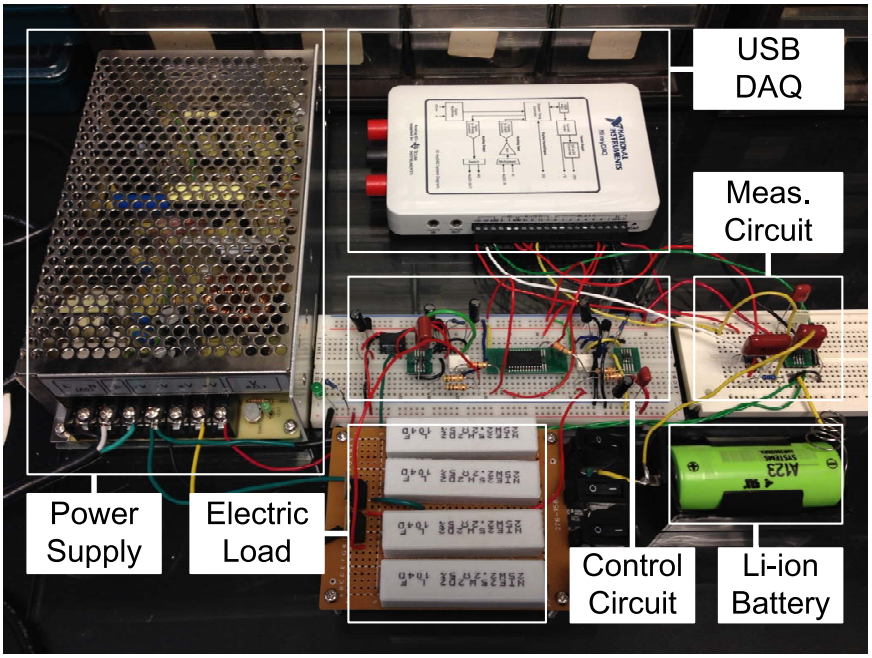

Figure 3.3: Photograph of the experimental battery tester.

The electric load is composed by a parallel connection of load resistors that behaves as a current limiter while the battery is charged, and it is the load when the battery is discharged. By switching in and out different number of load resistors, the charge/discharge can be at multiple levels.

In the measurement circuitry, the current sensor ACS714 has a bandwidth of 80 kHZ with a typical total output error of 1.5% at $T_A = 25$ °C. The absolute accuracy of analog-to-digital channels of the DAQ device is 22.8 mV typically at 23 °C in a range of ±10 V. Several low-order Butterworth low-pass filtering circuitries are reserved to process the measured signals for aliasing effects if necessary.

The description of the experimental setup is completed by a photograph of the experimental battery tester depicted in Fig. 3.3. The battery utilized in the test is a 2.3 Ah - 3.3 V $LiFePO_4$ battery cell ANR26650m1A from A123 Systems. The maximum continuous discharge current of the cell is 70 A. The pulse discharge current

can be 120 A. Hence the cell is suitable for transient high-power applications.

3.4 Preliminary Modeling Approach

3.4.1 Linear Model and Estimation

In building a dynamic model of a battery as a power storage and delivery system, the power charge/discharge demand signal $r(t)$ acts as an input signal, while the voltage signal $v(t)$ and the current signal $i(t)$ of the battery act as observable output signals. Multiplication of output signals leads to a power storage/delivery signal $p(t)$, as indicated in Fig. 3.4.

The preliminary modeling approach is done by linear models with an Auto-Regression with eXogeneous variables (ARX) model structure [55] for separate dynamic models between $r(t)$ as input and $v(t)$ and $i(t)$ as output, respectively. For ARX models, one can then estimate the parameters by a least-squares method and facilitate the use of a recursive implementation for real-time parameter estimation.

The procedure of building the ARX models between $r(t)$ and $v(t)$ or $i(t)$ is the same. For brevity, we only present the data-based modeling procedure for the voltage model with the input $r(t)$ and the output $v(t)$. Specifically, the voltage model is in the form

$$v(t) = \frac{B(q,\theta)}{A(q,\theta)} r(t) + \frac{1}{A(q,\theta)} \varepsilon(t,\theta) \tag{3.1}$$

where

$$\begin{aligned} A(q,\theta) &= 1 + a_1 q^{-1} + \cdots + a_{n_a} q^{-n_a} \\ B(q,\theta) &= b_1 q^{-1} + \cdots + b_{n_b} q^{-n_b} \end{aligned}$$

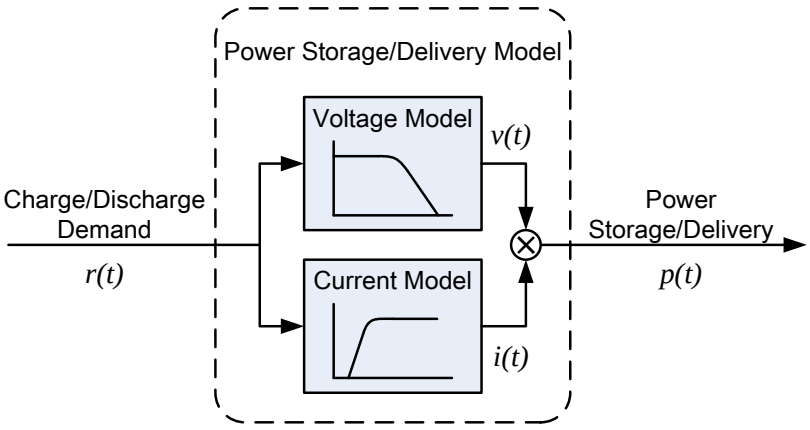

Figure 3.4: Diagram of the power storage/delivery model

in which q is forward time-shift: $qr(t) = r(t+1)$ and the parameter vector

$$\theta = \begin{bmatrix} a_1 & \cdots & a_{n_a} & b_1 & \cdots & b_{n_b} \end{bmatrix}^T \tag{3.2}$$

captures the unknown coefficients in the $A(q,\theta)$ and $B(q,\theta)$ polynomials.

To estimate the parameters, the error $\varepsilon(t,\theta)$ is written in a linear regression form

$$\varepsilon(t,\theta) = \varphi^T(t)\theta \tag{3.3}$$

where the regression vector

$$\begin{aligned} \varphi(t) = [&-v(t-1) \quad \cdots \quad -v(t-n_a) \\ &r(t-1) \quad \cdots \quad r(t-n_b)]^T \end{aligned} \tag{3.4}$$

consists of past voltage measurements $v(s),\ \ s < t$ and past charge/discharge demand signal $r(s),\ \ s < t$. We assume an inherent one-step time delay between the voltage and the charge/dischrage demand signal.

Due to the linear regression, the parameters can be estimated by the least-

squares method, which minimizes the least-squares criterion

$$V_N(\theta, Z^N) = \frac{1}{N}\sum_{t=1}^{N}\frac{1}{2}[v(t) - \varphi^T(t)\theta]^2 \tag{3.5}$$

The criterion can be minimized analytically, which gives the least-squares estimate (LSE) [55]

$$\hat{\theta}_N^{LS} = \arg\min V_N(\theta, Z^N) = R^{-1}(N) \cdot f(N) \tag{3.6}$$

provided the inverse of $R(N)$ exists, where

$$R(N) = \frac{1}{N}\sum_{t=1}^{N}\varphi(t)\varphi^T(t), \quad f(N) = \frac{1}{N}\sum_{t=1}^{N}\varphi(t)v(t)$$

To quantify the output variation that is explained by the model, the k-step-ahead predictor $\hat{v}(t|t-k)$ is introduced as

$$\hat{v}(t|t-k) = W_k(q)G(q)r(t) + [1 - W_k(q)]v(t) \tag{3.7}$$

$$W_k(q) \triangleq \bar{H}_k(q)H^{-1}(q), \quad \bar{H}_k(q) = \sum_{l=0}^{k-1}h(l)q^{-l} \tag{3.8}$$

where $h(l)$ is the impulse response of $H(q)$. For an ARX model, the filters $G(q,\theta)$ and $H(q,\theta)$ are parametrized as

$$G(q,\theta) = \frac{B(q,\theta)}{A(q,\theta)}, \quad H(q,\theta) = \frac{1}{A(q,\theta)} \tag{3.9}$$

Substituting (3.8) and (3.9) into (3.7), then the k-step-ahead predictor can be

rewritten as (omitting the parameter θ dependency for brevity)

$$\hat{v}(t|t-k) = \bar{H}_k(q)B(q)r(t) + [1 - \bar{H}_k(q)A(q)]v(t) \tag{3.10}$$

Finally, the model fit ratio is introduced:

$$\alpha_v = (1 - \frac{\|\hat{v}(t|t-k) - v\|}{\|v - \bar{v}\|}) \times 100\% \tag{3.11}$$

where $\bar{v}$ is the mean value of output.

Following the same procedure, we can also get the estimated parameters $\hat{\theta}_N^{LS}$ for the current model and the k-step-ahead predictor $\hat{i}(t|t-k)$. Then we can define the k-step-ahead predictor for the power storage and delivery model as

$$\hat{p}(t|t-k) = \hat{v}(t|t-k) \cdot \hat{i}(t|t-k) \tag{3.12}$$

Thus we can also get the model fit ratios α_i and α_p to quantify the prediction ability of the model.

In practice, if the number of data is large enough, then the data can be separated into two sets, which are for estimation and validation respectively. Furthermore, a few tests are taken to estimate the model order. With the model order increases, there exists one that can achieve the best model fit. If the model performance does not improve at higher orders, low-order models might fit the data equally well. The process of determining the model order can be taken iteratively.

3.4.2 Recursive Implementation

Recursive estimation of the parameter estimate $\hat{\theta}_t^{LS}$ as a function of time t allows real-time monitoring of the energy storage dynamics of the battery. Instead of batch-wise estimation using N data points to obtain $\hat{\theta}_N^{LS}$ given in (3.6), we compute the parameter estimate as the data from the power demand signal $r(t)$, the voltage $v(t)$ and current $i(t)$ is measured.

To formulate a computational effective recursive estimation for $\hat{\theta}_t^{LS}$, we first derive the relationship between $R(t-1)$ and $R(t)$. With

$$R(t) = \frac{1}{t}\sum_{\tau=1}^{t} \varphi(\tau)\varphi^T(\tau)$$

we have

$$R(t) = \frac{t-1}{t}R(t-1) + \frac{1}{t}\varphi(t)\varphi^T(t) \tag{3.13}$$

Note that matrix $R(t)$ is directly related to the inverse of the *covariance of the parameter estimate* $\hat{\theta}_t$ [55]. Similarly, we can also derive the relationship between $f(t-1)$ and $f(t)$

$$f(t) = \frac{t-1}{t}f(t-1) + \frac{1}{t}\varphi(t)y(t) \tag{3.14}$$

To allow for a recursive formulation of the parameter estimate $\hat{\theta}_t^{LS}$, we first rewrite $\hat{\theta}_t^{LS} = R^{-1}(t)f(t)$ as

$$\hat{\theta}_t^{LS} = R^{-1}(t)\left[\frac{t-1}{t}f(t-1) + \frac{1}{t}\varphi(t)y(t)\right]$$

To write this as a function of $\hat{\theta}_{t-1}^{LS}$, we now use the fact that $\hat{\theta}_{t-1}^{LS} = R^{-1}(t-$

$1)f(t-1)$ or $f(t-1) = R(t-1)\hat{\theta}_{t-1}^{LS}$ and substitution yields

$$\hat{\theta}_t^{LS} = R^{-1}(t)\left[\frac{t-1}{t}R(t-1)\hat{\theta}_{t-1}^{LS} + \frac{1}{t}\varphi(t)y(t)\right]$$

Finally we use (3.13) to substitute

$$R(t-1) = \frac{t}{t-1}R(t) - \frac{1}{t-1}\varphi(t)\varphi^T(t)$$

and we obtain

$$\begin{aligned}\hat{\theta}_t^{LS} &= R^{-1}(t)\left[\left(R(t) - \frac{1}{t}\varphi(t)\varphi^T(t)\right)\hat{\theta}_{t-1}^{LS} + \frac{1}{t}\varphi(t)y(t)\right] \\ &= \hat{\theta}_{t-1}^{LS} + \frac{1}{t}R(t)^{-1}\varphi(t)[y(t) - \varphi^T(t)\hat{\theta}_{t-1}^{LS}] \qquad (3.15)\end{aligned}$$

If we now define

$$\varepsilon(t, \hat{\theta}_{t-1}^{LS}) = y(t) - \varphi^T(t)\hat{\theta}_{t-1}^{LS} \qquad (3.16)$$

as the *a posteriori* prediction error, we can formulate a recursive parameter update by the order of (3.16), (3.13), and (3.15). In practice, the update of $R(t)$ can also be replaced by the update of the inverse of $R(t)$ (covariance update) and combined with the matrix inversion lemma to improve computational efficiency. Specifically, introduce the covariance matrix

$$P(t) \triangleq [tR(t)]^{-1} = \frac{1}{t}R^{-1}(t) \qquad (3.17)$$

Apply the matrix inversion lemma (3.18) to (3.17).

$$[A + BCD]^{-1} = A^{-1} - A^{-1}B[DA^{-1}B + C^{-1}]^{-1}DA^{-1} \tag{3.18}$$

With (3.13), taking $A = (t-1)R(t-1) = P^{-1}(t-1)$, $B = D^T = \varphi(t)$, and $C = 1$ gives

$$\begin{aligned} P(t) &= [tR(t)]^{-1} \\ &= [(t-1)R(t-1) + \varphi(t)\varphi^T(t)]^{-1} \\ &= P(t-1) - \frac{P(t-1)\varphi(t)\varphi^T(t)P(t-1)}{\varphi^T(t)P(t-1)\varphi(t) + 1} \end{aligned} \tag{3.19}$$

Thus, the recursive parameter update can be formulated by the following three steps:

- *a posteriori* prediction error update

$$\varepsilon(t, \hat{\theta}^{LS}_{t-1}) = y(t) - \varphi^T(t)\hat{\theta}^{LS}_{t-1} \tag{3.20}$$

- covariance update

$$P(t) = P(t-1) - \frac{P(t-1)\varphi(t)\varphi^T(t)P(t-1)}{\varphi^T(t)P(t-1)\varphi(t) + 1} \tag{3.21}$$

- parameter update

$$\hat{\theta}^{LS}_t = \hat{\theta}^{LS}_{t-1} + P(t)\varphi(t)\varepsilon(t, \hat{\theta}^{LS}_{t-1}) \tag{3.22}$$

It should be noted that the above three steps at $t = N$ gives the exact same parameter value $\hat{\theta}^{LS}_N$ as in (3.6), but the result is now written in terms of the previous

parameter estimate $\hat{\theta}_{t-1}^{LS}$ in a recursive fashion.

Furthermore we see that

$$\begin{aligned} \lim_{t\to\infty} R(t) &= \lim_{t\to\infty} \frac{1}{t} \sum_{\tau=1}^{t} \varphi(\tau)\varphi^T(\tau) \\ &= \Sigma_{\varphi,\varphi}(0) \text{ w.p. } 1 \end{aligned} \tag{3.23}$$

making $R(t)$ converge to the zero delay auto covariance (matrix) Σ of the regressor $\varphi(t)$ as $t \to \infty$.

Provided $R_{\varphi,\varphi}(0)$ is non-singular, thus

$$\lim_{t\to\infty} P(t) = \lim_{t\to\infty} \frac{1}{t} R^{-1}(t) = 0 \text{ w.p. } 1 \tag{3.24}$$

which allows the recursive parameter update to *converge to a stationary point* $\theta^\star$ *of the recursion*

$$\lim_{t\to\infty} \hat{\theta}_t^{LS} = \lim_{t\to\infty} \hat{\theta}_{t-1}^{LS} = \theta^\star \text{ w.p. } 1 \tag{3.25}$$

The convergence is desired when the parameter θ is not changing. However, to account for changes in θ, we adjust the covariance update with the disturbance factor λ to

$$P(t) = P(t-1) - \frac{P(t-1)\varphi(t)\varphi^T(t)P(t-1)}{\varphi^T(t)P(t-1)\varphi(t) + 1} + \lambda I \tag{3.26}$$

where $0 < \lambda \ll 1$.

With the additional term λI, the convergence w.p. 1 of the parameter estimate is sacrificed to allow parameter adaptation.

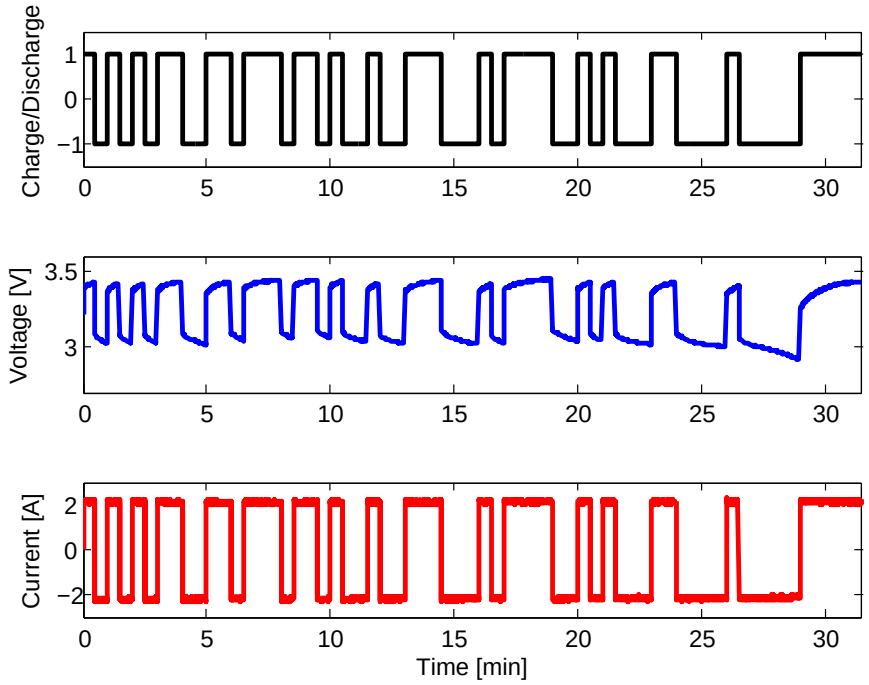

Figure 3.5: Experimental results (cycle, voltage, current)

3.4.3 Modeling Results

The charge/discharge cycle shown in Fig. 3.5 is utilized in the test, where the charge/discharge signal +1 represents charging and -1 represents discharging. The cycle is created by a stretched pseudo-random binary signal (PRBS) of order 6. Though the stretching leads to the loss of white-noise-like properties, the sequence still contains all the possibilities of binary combinations of order 6.

The measured signals of voltage and current are also shown in Fig. 3.5. The signals vary with the alternating between charge and discharge as expected. Due to the design of the circuitry, the charge and discharge current is approximately at the rate of 1C, which is 2.3A. As shown in Fig. 3.5, the dynamic model of the voltage can be considered as a low-pass filter, while the dynamic model of the current can be treated as a high-pass filter or a gain function.

Experimental data-based modeling

For identification and model validation purposes, the data is separated into two sets. The measured data of first 15 minutes is used to estimate the parameters, and the rest of the data is applied to validate the models. Both a batch-wise estimation and a recursive estimation is used on the first 15 minutes of experimental data. Following the data-based modeling presented in the previous section, the batch-wise estimation leads to the following linear voltage model and the linear current model respectively:

- Voltage Model

$$v(t) = \frac{0.167q^{-1} - 0.08295q^{-2} - 0.08387q^{-3}}{1 - 0.5031q^{-1} - 0.4969q^{-2}} r(t) + \frac{1}{1 - 0.5031q^{-1} - 0.4969q^{-2}} e(t)$$

- Current Model

$$i(t) = \frac{2.09q^{-1}}{1 - 0.03149q^{-1}} r(t) + \frac{1}{1 - 0.03149q^{-1}} e(t)$$

To validate the model, the prediction quality of the model is tested. As mentioned above, the k-step-ahead predictor $\hat{v}(t|t-k)$, $\hat{i}(t|t-k)$, and $\hat{p}(t|t-k)$ is computed from past data, including k-step-ahead outputs and up-to-now inputs. The 5-step-ahead prediction of voltage and current is shown in Fig. 3.6, comparing with the measured data. As shown in Fig. 3.6, the prediction of voltage and current is close to the measured data. Combining two individual dynamic models obtained above, the power storage/delivery model is built. The 5-step-ahead prediction of power is shown in Fig. 3.7. The model fit ratios of the voltage model, the current model, and

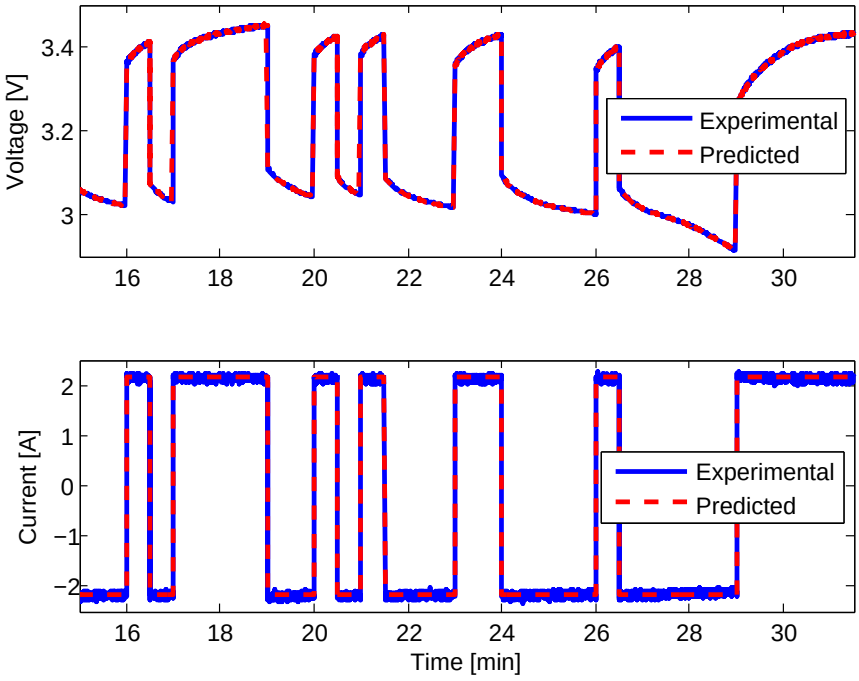

Figure 3.6: 5-step-ahead prediction of the voltage and current models

the power storage/delivery model are shown in Table 3.1.

Table 3.1: Model Fit Ratios α

Voltage Model	α_v	99.112%
Current Model	α_i	97.979%
Power Storage/Delivery Model	α_p	97.994%

The estimation results indicate that a fairly simple model created by the multiplication of two linear models in a signal setting from the charge/discharge demand signal $r(t)$ to the power storage and delivery signal $p(t) = v(t) \cdot i(t)$ is able to capture the energy storage dynamics of the battery very well. The model has been validated on data not used during the identification.

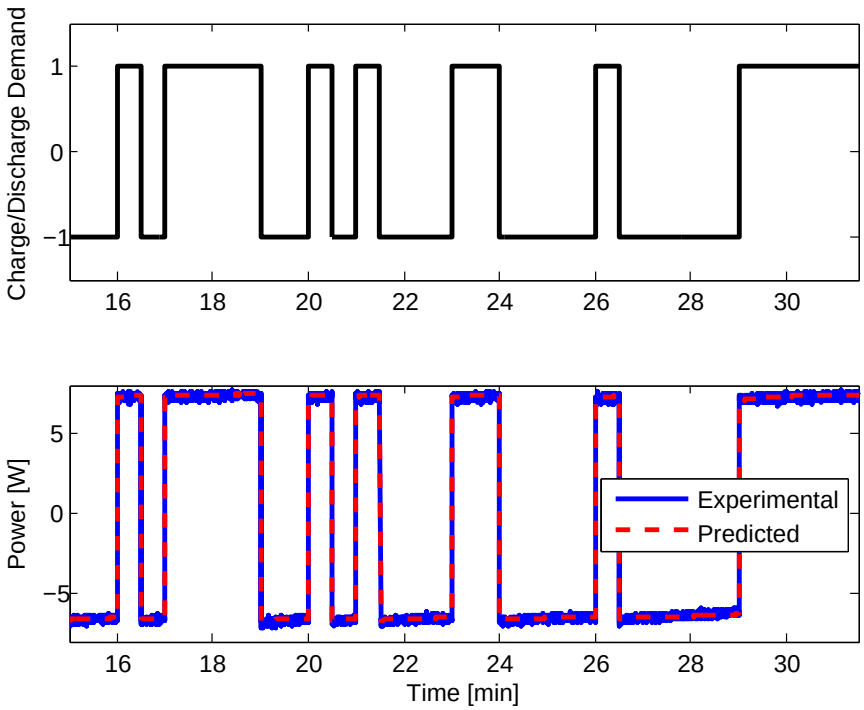

Figure 3.7: 5-step-ahead prediction of the power storage/delivery model

Recursive implementation of parameter estimate

Applying the recursive parameter update procedure (3.20), (3.21), and (3.22), we can get the recursive estimated parameters of linear voltage and current models shown in Fig. 3.8. As expected, the estimated parameters indicated as solid lines converge to the parameters estimated by (3.6) indicated as dashed lines. Hence the recursive implementation can also estimate the parameters of the required linear models of voltage and current.

When the disturbance factor λ is non-zero, the recursive estimated parameters do not converge but become more sensitive to the latest measured signals as shown in Fig. 3.9.

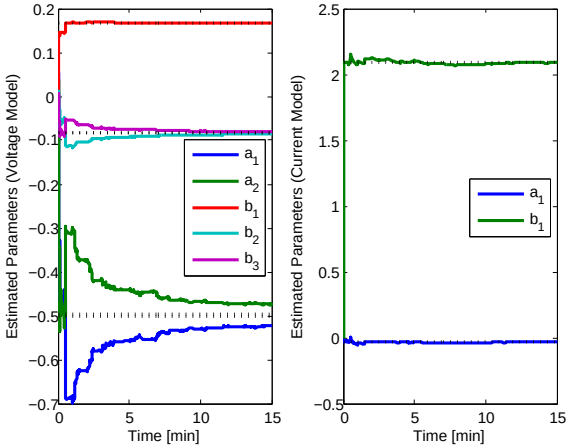

Figure 3.8: Estimated parameters of voltage and current models ($\lambda = 0$)

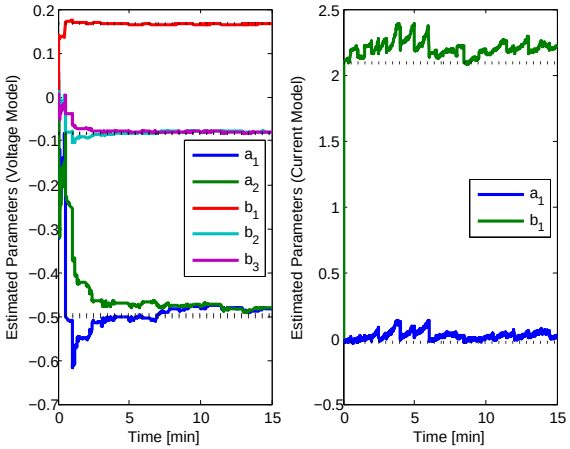

Figure 3.9: Estimated parameters of voltage and current models ($\lambda = 0.005$)

3.5 Non-linear Modeling Approach

The preliminary modeling approach introduced in the previous section is able to capture linear dynamics of the system and predict the output 5-step ahead, which can be applied for monitoring purposes. However, a complete model which can capture all the critical dynamics of the system is still of interest. As introduced in Section 3.1, there exists non-linearities in a battery, such as the OCV characteristics and hysteresis. Therefore, some research need to be conducted to obtain a completed model which can not only capture linear dynamics, but also non-linear dynamics in

a battery system.

3.5.1 Model Framework and Parameterization

The battery model proposed in this paper is composed by separated voltage and current models as indicated in Fig. 3.10. The non-linearity generated by the product of the voltage and current dynamics can be treated separately through such modeling. The model input is the charge and discharge demand to the battery $r(k)$, and the output is the stored or delivered power of the battery

$$p(k) = v(k) \cdot i(k), \tag{3.27}$$

where $v(k)$ is the terminal voltage of battery, and $i(k)$ is the current.

In practice, $r(k)$ can represent any applicable power demand or control signal to a battery system, as long as it is monotonic with the power output. Therefore, $r(k)$ can even be unit-less.

Model Components

All the components inserted into the model framework are used to cover the dynamic and non-linear behavior over a wider operating range of battery needs to be handled. The motivation of the use of various model components can be explained by taking a quick glance at a set of experimental data as indicated in Fig. 3.11. The voltage dynamics w.r.t. charge/discharge demand in Region I and II, which is the normal operating range of the battery, can be possibly captured by a linear model with static non-linearity combining the OCV characteristics to adjust the offset along the time. However, when the battery is operating in slightly over-charging scenario,

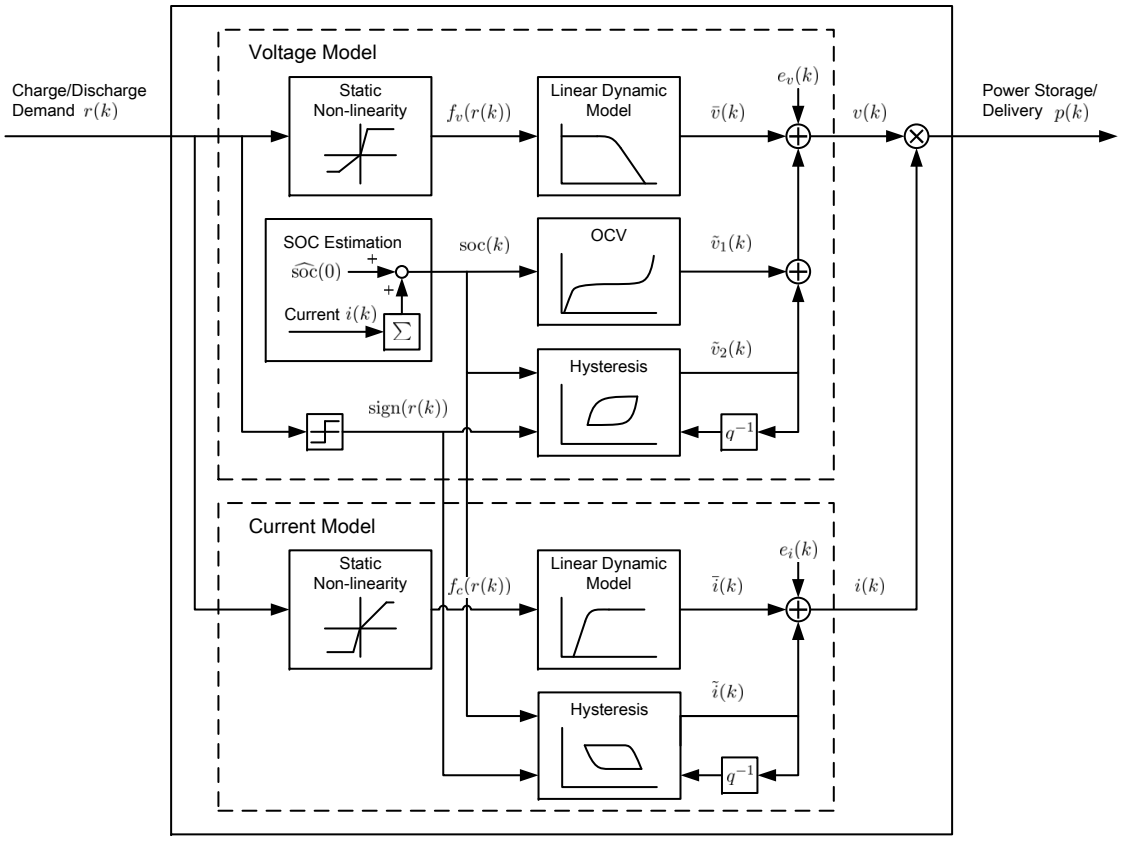

Figure 3.10: Diagram of the proposed battery model composed of separated voltage and current models.

i.e. Region III, the voltage dynamics may exhibit significant hysteresis phenomena. Therefore a hysteresis model is added in order to handle a dynamic non-linearity in such case.

Combing the above mentioned observations, the voltage model is built up by the following model components: a Hammerstein model, the OCV characteristics, and a hysteresis model. This results in a voltage model output

$$v(k) = \bar{v}(k) + \tilde{v}_1(k) + \tilde{v}_2(k) + e_v(k), \tag{3.28}$$

where

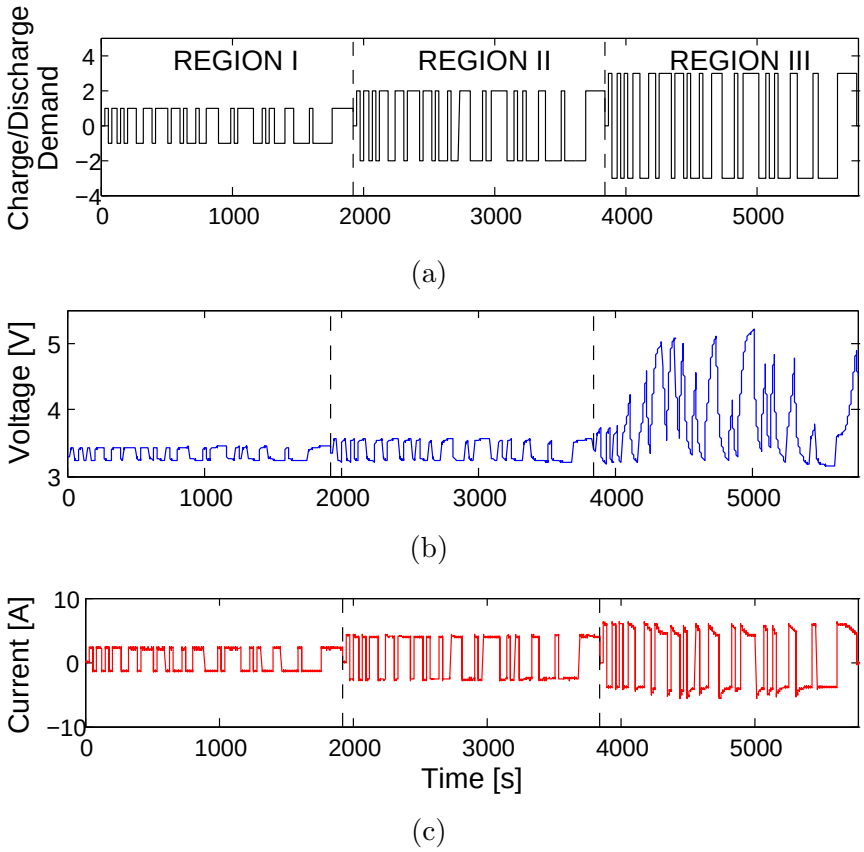

Figure 3.11: Experimental data of a battery system. (a) System input - charge/discharge demand signal P_B^{dem}; (b) System output - battery terminal voltage V_B; (c) System output - battery current I_B.

$\bar{v}(k)$ is the output of Hammerstein model;

$\tilde{v}_1(k)$ is the OCV;

$\tilde{v}_2(k)$ is the output of hysteresis model;

$e_v(k)$ is the voltage measurement noise.

In practice, each component is effective in a certain operating range of the battery. For instance, the hysteresis model should be weighted more in the battery over-charging scenario, while the OCV characteristics is able to sufficiently compensate the non-linearity in most of normal operation range of the battery system. Some further analysis in Section 3.5.3 explains these observations in more details.

Since the static system non-linearity and hysteresis phenomena also exist in the current output of the system, the current model structure is built up similar to that of the voltage model, but without the necessity of compensation by the OCV characteristics. Thus, the current model combines a Hammerstein model and a hysteresis model. The dynamic output of the current model is then given by

$$i(k) = \bar{i}(k) + \tilde{i}(k) + e_i(k), \tag{3.29}$$

where

$\bar{i}(k)$ is the output of Hammerstein model;

$\tilde{i}(k)$ is the output of hysteresis model;

$e_i(k)$ is the current measurement noise.

At first glance, the proposed battery model to capture static non-linearities, linear dynamics, and hysteresis in both the voltage and current signal seems highly complex, it is shown that each individual model component has only a finite number of parameters that can be estimated from data. Moreover, as motivated earlier, these three model components, static non-linearity, linear dynamics, and hysteresis, are shown to be required to capture the full operating range of the battery in both normal and possibly over/under-charging conditions. More details on the individual model components now follow.

Voltage Model Parameterization

- *Hammerstein Model*

  A Hammerstein model cascades a linear dynamic model with an static input

non-linearity [55]:

$$\bar{v}(k) = G_v(q, \theta) f_v(r(k)). \tag{3.30}$$

It includes a static non-linearity and linear dynamics of the voltage model with respect to charge and discharge demand input. Linear regression model structure can be applied to re-shape the model

$$\bar{v}(k) = \varphi_v^T(k)\theta_v, \tag{3.31}$$

where

θ_v is the parameter vector;

$\varphi_v(k)$ is the regression matrix containing past inputs with static non-linearity $f_v(r(k))$, and past outputs $\bar{v}(k)$. In particular, the voltage regressor is given by

$$\varphi_v(k) = \begin{bmatrix} f_v(r(k - n_{b,v} + 1)) \\ f_v(r(k - n_{b,v} + 2)) \\ \vdots \\ f_v(r(k)) \\ \bar{v}(k - n_{a,v} + 1) \\ \bar{v}(k - n_{a,v} + 2) \\ \vdots \\ \bar{v}(k - 1) \end{bmatrix}, \tag{3.32}$$

where $n_{b,v}$ and $n_{a,v}$ determines the order of the model. To ensure that the model is causal, $n_{b,v} \leq n_{a,v}$.

- *OCV Characteristics*

Since lithium-ion batteries are of interest in this paper, and the Hammerstein model introduced in Section 3.5.1 already includes linear dynamics, the OCV model is obtained by modifying the proposed model in [39] to

$$\tilde{v}_1(k) = g_{\text{ocv}}(\text{soc}(k), i(k), \text{sign}(r(k))). \tag{3.33}$$

In particular,

$$\begin{aligned} g^{+}_{\text{ocv}} &= E_0 - K\frac{Q}{Q-\text{soc}(k)}\text{soc}(k) - K\frac{Q}{Q-\text{soc}(k)}i(k) \\ &\quad + A\cdot e^{-B\cdot\text{soc}(k)}; \\ g^{-}_{\text{ocv}} &= E_0 - K\frac{Q}{Q-\text{soc}(k)}\text{soc}(k) - K\frac{Q}{\text{soc}(k)-0.1\cdot Q}i(k) \\ &\quad + A\cdot e^{-B\cdot\text{soc}(k)}, \end{aligned} \tag{3.34}$$

where

$g^{+}_{\text{ocv},v}$ is the charge scenario;

$g^{-}_{\text{ocv},v}$ is the discharge scenario;

E_0 is the battery constant voltage (V);

K is the polarization constant (V/(Ah)) or polarization resistance (Ω);

Q is the nominal battery capacity (Ah);

A is exponential zone amplitude (V);

B is exponential zone time constant inverse ($(\text{Ah})^{-1}$).

The charge and discharge is determined by $\text{sign}(r(k))$, where $\text{sign}(r(k)) = 1$ indicates the battery is charging; $\text{sign}(r(k)) = -1$ indicates the battery is discharging.

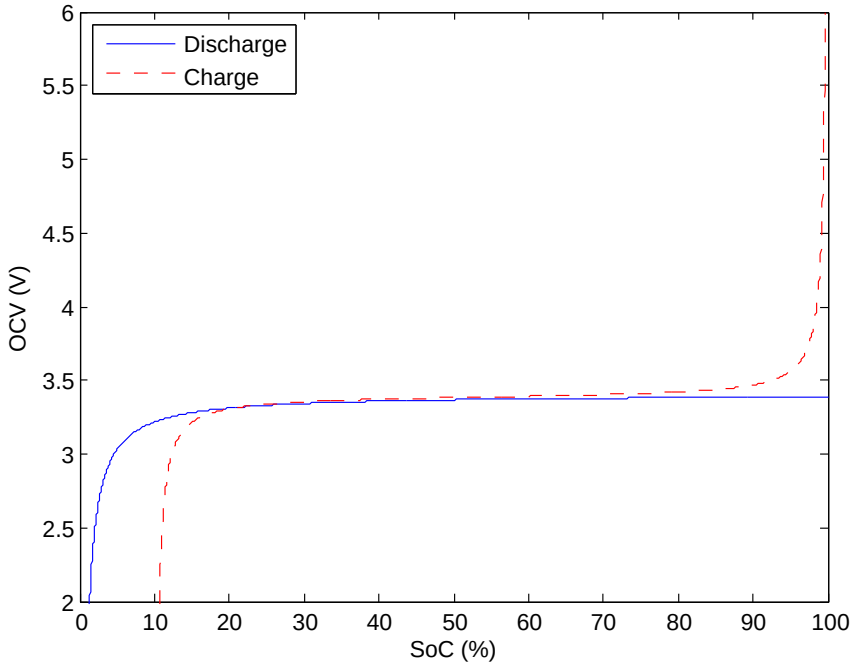

Figure 3.12: OCV characteristics of 1 C charge and discharge of the battery under tests. The unit C indicates the current rate by which the battery can be fully charged or discharged in one hour.

According to the specifications of the battery under tests, the OCV characteristics can be determined. The OCV characteristics of one of the batteries under 1 C charge and discharge is given as an example in Fig. 3.12.

- *Takacs Hysteresis Model*

  The hysteresis model is parameterized based on Takacs hysteresis model [51]:

$$\tilde{v}_2(k) = g_{\text{hys},v}(\text{soc}(k), \tilde{v}_2^0(k), \text{sign}(r(k))). \tag{3.35}$$

In particular,

$$g_{\text{hys},v}^{+}(k) = \tanh(\text{soc}(k) + a_0) - b_c + A_0 \cdot \text{soc}(k); \tag{3.36}$$

$$g_{\text{hys},v}^{-}(k) = \tanh(\text{soc}(k) - a_0) + b_d + A_0 \cdot \text{soc}(k), \tag{3.37}$$

where

$g^{+}_{\mathrm{hys},v}$ represents the charge scenario;

$g^{-}_{\mathrm{hys},v}$ is the discharge scenario.

Similarly, the charge and discharge is determined by $\mathrm{sign}(r(k))$. Moreover, the parameters

$$\begin{aligned} b_c = b_3 \cdot \frac{\tanh(-x_m + d_0 + a_0) - \tanh(\mathrm{soc}(k) + a_0)}{\tanh(-x_m + d_0 + a_0) - \tanh(x_m + d_0 + a_0)} \\ + b_4 \cdot \frac{\tanh(x_m + d_0 + a_0) - \tanh(\mathrm{soc}(k) + a_0)}{\tanh(x_m + d_0 + a_0) - \tanh(-x_m + d_0 + a_0)}, \end{aligned} \tag{3.38}$$

$$\begin{aligned} b_d = b_3 \cdot \frac{\tanh(-x_m + d_0 - a_0)}{\tanh(-x_m + d_0 - a_0) - \tanh(x_m + d_0 - a_0)} \\ + b_4 \cdot \frac{\tanh(x_m + d_0 - a_0) - \tanh(\mathrm{soc}(k) - a_0)}{\tanh(x_m + d_0 - a_0) - \tanh(-x_m + d_0 - a_0)}. \end{aligned} \tag{3.39}$$

b_3 and b_4 are parameters to shift the crossover points x_m and $-x_m$ by the magnitude of d_0:

$$b_3 = [\tanh(x_m + d_0 + a_0) - \tanh(x_m + d_0 - a_0)]/2; \tag{3.40}$$

$$b_4 = [\tanh(-x_m + d_0 + a_0) - \tanh(-x_m + d_0 - a_0)]/2. \tag{3.41}$$

$\tilde{v}_2^0(k)$ denotes the initial voltage $\tilde{v}_2$ of the current continuous charge or discharge. Since $\tilde{v}_2$ during charge and discharge is continuous, $\tilde{v}_2^0(k)$ determines the particular hysteresis loop by which $\tilde{v}_2(k)$ changes. As depicted in Fig. 3.13, $\tilde{v}_2^0(k)$ determines d_0 in charge scenarios, while it determines a_0 in discharge scenarios.

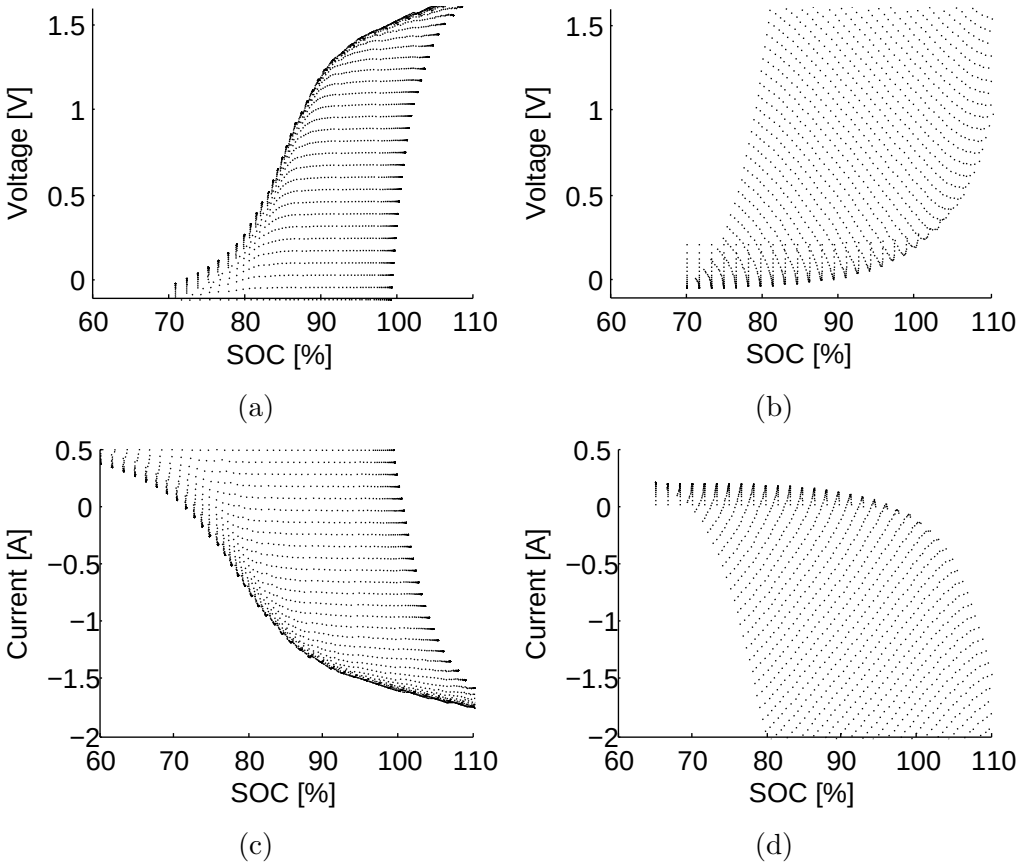

Figure 3.13: Takacs hysteresis model for voltage and current models. (a) charge scenario of voltage model; (b) discharge scenario of voltage model; (c) charge scenario of current model; (d) discharge scenario of current model.

Current Model Parameterization

The parameterization of the current model is similar to that of the voltage model. In particular, the Hammerstein model is parameterized by

$$\bar{i}(k) = G_i(q,\theta) f_i(r(k)) = \varphi_i^T(k)\theta_i, \tag{3.42}$$

where the current regressor

$$\varphi_i(k) = \begin{bmatrix} f_i(r(k-n_{b,i}+1)) \\ f_i(r(k-n_{b,i}+2)) \\ \vdots \\ f_i(r(k)) \\ \bar{i}(k-n_{a,i}+1) \\ \bar{i}(k-n_{a,i}+2) \\ \vdots \\ \bar{i}(k-1) \end{bmatrix}; \tag{3.43}$$

and the hysteresis model is given by

$$\tilde{i}(k) = g_{\text{hys},i}(\text{soc}(k), \tilde{i}^0(k), \text{sign}(r(k))), \tag{3.44}$$

where

$$g^+_{\text{hys},i}(k) = -[\tanh(\text{soc}(k) + a_0) - b_c + A_0 \cdot \text{soc}(k)]; \tag{3.45}$$

$$g^-_{\text{hys},i}(k) = -[\tanh(\text{soc}(k) - a_0) + b_d + A_0 \cdot \text{soc}(k)]. \tag{3.46}$$

The parameters b_c, b_d, b_3, and b_4 are defined as given by (3.38)–(3.41). Similarly, $\tilde{i}^0(k)$ determines d_0 in charge scenarios, while it determines a_0 in discharge scenarios.

3.5.2 Model Estimation Methods

As introduced in Section 3.1, the static OCV characteristics are usually measured and given through off-line tests. Therefore, identification of the rest of models, including Hammerstein model, Takacs hysteresis model, and SOC estimation, is introduced in details in this section.

Identification of Hammerstein Model

The identification methods of a Hammerstein model are developed extensively [56]. In this paper, the static input non-linearity is *a priori* knowledge, therefore the identification of the Hammerstein model is simplified to the parameter estimation of the linear regression model given by (3.31) and (3.42). Particularly, the parameter estimation is achieved by Bootstrap Instrumental-Variable (BIV) method with batch-wise data, which can be further applied as an on-line estimation in practical applications.

- *Bootstrap IV Method*

  When the regression matrix (3.32) and (3.43) is *a priori* knowledge, that is, the order and the terms containing past inputs and past outputs are known, the model is obtained once the parameter vectors θ_v and θ_i are estimated. For simplicity, a general linear regression model with an output $y(k)$ is given for the description and further analysis:

$$\hat{y}(k|\theta) = \varphi^T(k)\theta, \tag{3.47}$$

  where $\hat{y}(k|\theta)$ denotes the estimated model output given a certain parameter

vector θ. The regressor $\varphi(k)$ consists of a set of delayed output values $y(l)$, $l = k - n_b + 1, k - n_b + 2, \cdots, k$, and input values $u(l)$, $l = k - n_a + 1, k - n_a + 2, \cdots, k - 1$, which is similar to $\varphi_v(k)$ in (3.32) and $\varphi_i(k)$ in (3.43).

The objective of estimating parameters θ is to minimize the difference between the actual system output $y(k)$ and the estimated output $\hat{y}(k|\theta)$. A widely-applied approach is the Least-Squares Estimate (LSE), which is a special case under the prediction-error identification framework. Provided finite N samples, the estimated parameter by LSE is found by minimizing

$$\underset{\theta}{\operatorname{argmin}} \|\hat{y}(k|\theta) - y(k)\|_2^2 . \tag{3.48}$$

The solution is given by

$$\hat{\theta}_N^{LS} = \left[\frac{1}{N}\sum_{k=0}^{N-1}\varphi(k)\varphi^T(k)\right]^{-1}\left[\frac{1}{N}\sum_{k=0}^{N-1}\varphi(k)y(k)\right]. \tag{3.49}$$

However, the estimated parameter $\hat{\theta}_N^{LS}$ through LSE will not tend to θ_0 due to the correlation between $\varphi(t)$ and the noise in system $v_0(t)$ [55]. To eliminate the noise effect, Instrumental-Variable (IV) method is introduced as follows:

$$\hat{\theta}_N^{IV} = \left[\frac{1}{N}\sum_{k=0}^{N-1}\zeta(k)\varphi^T(k)\right]^{-1}\left[\frac{1}{N}\sum_{k=0}^{N-1}\zeta(k)y(k)\right]. \tag{3.50}$$

Notice that LSE is a special case of IV method. By properly designing the instrument matrix $\zeta(k)$, $\hat{\theta}_N^{IV}$ can tend to θ_0 despite the correlation between the regression matrix and noises.

There are multiple kinds of IV methods, which can be categorized by the instru-

ment variant design, e.g. four-step IV algorithm [55]. In this paper, one of these methods named Bootstrap IV (BIV) method, is utilized within the parameter estimation. A typical BIV is an iterative algorithm:

$$\hat{\theta}_N^{j+1} = \left[\frac{1}{N}\sum_{k=0}^{N-1}\zeta(k,\hat{\theta}^j)\varphi^T(k)\right]^{-1}\left[\frac{1}{N}\sum_{k=0}^{N-1}\zeta(k,\hat{\theta}^j)y(k)\right]. \tag{3.51}$$

where $\zeta(k,\hat{\theta}^j)$ denotes either a voltage or current regressor. The main difference between $\zeta(k,\hat{\theta}^j)$ and the regressors $\varphi_v(k)$ in (3.32) and $\varphi_i(k)$ in (3.43) lies in the fact that the measured (noisy) voltage measurement $\bar{v}(k)$ and current measurement $\bar{i}(k)$ are replaced by "noise-free" (simulated) signals obtained from a model $G_v(q,\hat{\theta}^j)$ in (3.30) and $G_i(q,\hat{\theta}^j)$ in (3.42) based on an initial or previous parameter estimate $\hat{\theta}^j$. More precisely,

$$\zeta_v(k,\hat{\theta}^j) = \begin{bmatrix} f_v(r(k-n_{b,v}+1)) \\ f_v(r(k-n_{b,v}+2)) \\ \vdots \\ f_v(r(k)) \\ x_v(k-n_{a,v}+1) \\ x_v(k-n_{a,v}+2) \\ \vdots \\ x_v(k-1) \end{bmatrix}, \tag{3.52}$$

where

$$x_v(k) = G_v(q,\hat{\theta}^j)f_v(r(k)). \tag{3.53}$$

A similar structure is for the regressor $\zeta_i(k,\hat{\theta}^j)$. The parameter set $\hat{\theta}_N^{IV}(N-1)$

is initialized by the LSE (3.49) provided the first data set of N samples, which are data points at time index $k = 0, 1, \cdots, N-1$. Then for subsequent data points at $k > N-1$, the estimated parameter set is updated from $\hat{\theta}_N^{IV}(k-1)$.

- *Convergence Analysis of Bootstrap IV Method*

  For simplicity, only a Single-Input-Single-Output (SISO) system is analyzed. Let $N \to \infty$, (3.51) becomes

$$\hat{\theta}^{j+1} = \left[\mathrm{E}\zeta(k, \hat{\theta}^j)\varphi^T(k)\right]^{-1} \left[\mathrm{E}\zeta(k, \hat{\theta}^j)y(k)\right]. \tag{3.54}$$

  If $\bar{\theta}$ is an equilibrium point, then

$$\mathrm{E}\zeta(k, \bar{\theta}) \left[y(k) - \varphi^T(k)\bar{\theta}\right] = 0. \tag{3.55}$$

  Therefore through a linearization,

$$\begin{aligned} \hat{\theta}^{j+1} - \bar{\theta} &= \left[\mathrm{E}\zeta(k, \hat{\theta}^j)\varphi^T(k)\right]^{-1} \mathrm{E}\zeta(k, \hat{\theta}^j) \left[y(k) - \varphi^T(k)\bar{\theta}\right] \\ &= \left[\mathrm{E}\zeta(k, \hat{\theta}^j)\varphi^T(k)\right]^{-1} \mathrm{E}\left[\frac{\partial \zeta}{\partial \theta}(k, \theta)|_{\theta=\bar{\theta}}\{y(k) - \varphi^T(k)\bar{\theta}\}\right] \\ &\quad \cdot (\hat{\theta}^j - \bar{\theta}) + \left\|\hat{\theta}^j - \bar{\theta}\right\|^2. \end{aligned} \tag{3.56}$$

  Thus, $\hat{\theta}^j$ is locally convergent to $\bar{\theta}$ provided the matrix

$$\mathcal{A} = \left[\mathrm{E}\zeta(k, \hat{\theta}^j)\varphi^T(k)\right]^{-1} \mathrm{E}\left[\frac{\partial \zeta}{\partial \theta}(k, \theta)|_{\theta=\bar{\theta}}\{y(k) - \varphi^T(k)\bar{\theta}\}\right] \tag{3.57}$$

  has all eigenvalues within the unit circle. A necessary condition for the matrix $\mathrm{E}\zeta(k, \hat{\theta}^j)\varphi^T(k)$ to be nonsingular is that the input $u(k)$ included in $\varphi(k)$ is

persistently exciting of order $n_a + n_b$ [57], that is, the auto-spectrum $\Phi_u(\omega)$ is different from zero on at least $n_a + n_b$ points in the interval $-\pi \leqslant \omega \leqslant \pi$ [55]. Another obvious condition for non-singularity is the existence of a non-zero correlation between the instrument $\zeta(k)$ and the original regressor $\varphi(k)$, i.e. the instrument cannot be chosen to be completely independent of the I/O signals $\{u(k), y(k)\}$ of the system. Both conditions are satisfied with the choice of the instrument $\zeta(k)$ that consists of a combination of the measured noise-free input $u(k) = f_v(r(k))$ as in (3.32) and noise-free simulated outputs $x_v(k) = G_v(q, \hat{\theta}^j) f_v(r(k))$ as in (3.53) obtained from the iterative parameter estimation update.

- *Initial Condition Estimate*

  A typical regression matrix $\varphi(k)$ and instrument matrix $\zeta(k)$ consists of shifted data. Given finite number N samples in a time interval $[0, N-1]$, the unknown initial conditions for $k < 0$ need to be dealt with. When N is sufficiently large, which means the data set contains sufficient information, some data can be truncated to ensure the estimation is taken only with known data.

  When N is small, a second approach, which treats n_{ic} unknown initial conditions as to-be-estimated parameters θ_{ic}, is also a solution. For a causal system, the current output depends only on past inputs and past outputs, therefore N samples of input and output of system (3.47) can be reformed as

$$\mathbf{Y_N} = \begin{bmatrix} \mathbf{\Phi}_{ic} & \mathbf{I} \\ \mathbf{\Phi} & \mathbf{0} \end{bmatrix} \begin{bmatrix} \theta \\ \theta_{ic} \end{bmatrix} \tag{3.58}$$

where

$$\mathbf{Y_N} = \begin{bmatrix} y(0) & \cdots & y(n_{ic}) & \cdots & y(N-1) \end{bmatrix}^T, \tag{3.59}$$

$$\mathbf{\Phi} = \begin{bmatrix} \varphi(n_{ic}+1) & \varphi(n_{ic}+2) & \cdots & \varphi(N-1) \end{bmatrix}^T, \tag{3.60}$$

and $\mathbf{\Phi}_{ic}$ is the adjusted regression matrix excluding corresponding terms which consist of unknown initial conditions.

SOC Estimation

There exist a large number of SOC estimation algorithms in the literature, as introduced in Section 3.1. Those estimation approaches can be candidates for SOC estimation in the proposed model framework depicted in Fig. 3.10, given proper inputs. In this paper, the SOC is estimated in a simple but effective recursive optimization pattern, which can be easily integrated into the model framework.

At a given time T, the SOC can be calculated through coulomb-counting

$$\mathrm{soc}(T) = \mathrm{soc}_0 + \sum_{k=0}^{T-1} i(k) \cdot T_s/Q. \tag{3.61}$$

where T_s is the sampling time, Q is the nominal battery capacity.

Since $i(k), k = 0, 1, \cdots, T-1$, is measured and given, the estimation of $\mathrm{soc}(T)$ is then converted to the estimation of soc_0, which is the constant initial SOC in a continuous charge and discharge process of battery. The estimation of soc_0 is obtained in the voltage model by

$$\widehat{\mathrm{soc}}_0(T) = \underset{\mathrm{soc}_0}{\mathrm{argmin}} \frac{1}{T} \left\| \widehat{\mathbf{V}}_T - \mathbf{V}_T \right\|_2^2, \tag{3.62}$$

where

$$\widehat{\mathbf{V}}_T = \begin{bmatrix} \hat{v}(0) & \hat{v}(1) & \cdots & \hat{v}(T-1) \end{bmatrix}^T, \tag{3.63}$$

$$\mathbf{V}_T = \begin{bmatrix} v(0) & v(1) & \cdots & v(T-1) \end{bmatrix}^T, \tag{3.64}$$

and

$$\hat{v}(k) = \varphi^T(k)\hat{\theta}_N^{IV}(k) + g_{\text{ocv}}(\widehat{\text{soc}}(k), i(k), \text{sign}(r(k))). \tag{3.65}$$

Although $\widehat{\mathbf{V}}_T$ is non-linear w.r.t. $\text{soc}_0(T)$, $\widehat{\text{soc}}_0(T)$ can be achieved via a line search for each parameter $\hat{\theta}_N^{IV}(k)$ estimated, since $\text{soc}_0 \in \mathbf{R}$ and bounded.

Identification of Takacs Hysteresis Model

In this section, the hysteresis phenomena occurring when the battery is in large SOC is of interest, as depicted in Fig. 3.13. Take voltage hysteresis model for example, the estimation is completed first by proper mapping, and then determining parameters by

$$\text{sign}(r(k)) = 1 : d_0(\tilde{v}_2^0(k)) = \underset{d_0}{\text{argmin}} \frac{1}{n} \left\| \widehat{\tilde{\mathbf{V}}}_n - \tilde{\mathbf{V}}_n \right\|_2^2; \tag{3.66}$$

$$\text{sign}(r(k)) = -1 : a_0(\tilde{v}_2^0(k)) = \underset{a_0}{\text{argmin}} \frac{1}{n} \left\| \widehat{\tilde{\mathbf{V}}}_n - \tilde{\mathbf{V}}_n \right\|_2^2, \tag{3.67}$$

given n samples in a continuous charge and discharge.

$$\widehat{\tilde{\mathbf{V}}}_n = \begin{bmatrix} \hat{\tilde{v}}_2(0) & \hat{\tilde{v}}_2(1) & \cdots & \hat{\tilde{v}}_2(n-1) \end{bmatrix}^T, \tag{3.68}$$

$$\tilde{\mathbf{V}}_n = \begin{bmatrix} \tilde{v}_2(0) & \tilde{v}_2(1) & \cdots & \tilde{v}_2(n-1) \end{bmatrix}^T, \tag{3.69}$$

where $\hat{\tilde{v}}_2(k)$ is given by (3.36), (3.37); and

$$\tilde{v}_2(k) = v(k) - \varphi^T(k)\hat{\theta}_N^{IV}(k) - g_{\text{ocv}}(\widehat{\text{soc}}(k), i(k), \text{sign}(r(k))). \tag{3.70}$$

Similarly, the solution to $d_0(\tilde{v}_2^0(k))$ and $a_0(\tilde{v}_2^0(k))$ can also be achieved via line search.

3.5.3 Modeling and Analysis

Extensive experiments are conducted with the experimental setup. A data set of interest is selected to be applied as the data base for validation of the modeling approach. The data set is already shown as in Fig. 3.11, where 3 regions of charge/discharge demand levels are used to characterize the possible non-linear dynamics of the battery system being tested. The sampling rate is 10 Hz. In particular, three-levels of Pseudo Random Binary Sequence (PRBS) of input signal is implemented. The presented charge/discharge cycle in the experimental data is typical of battery used for ancillary services in an electric grid to provide maximum charge/discharge rates to store/deliver energy at desired moments to account for load and/or energy production demands [24, 25].

For further analysis, the results are divided into Region I, II, and III according to different levels of input excitation. In Region I and II, similar dynamics of voltage and current is measured. However, significantly different dynamics are obtained in Region III, since the battery is already over charged, which can be indicated by the terminal voltage. In fact, the battery cell exploded due to over-charge in the end of the experiment.

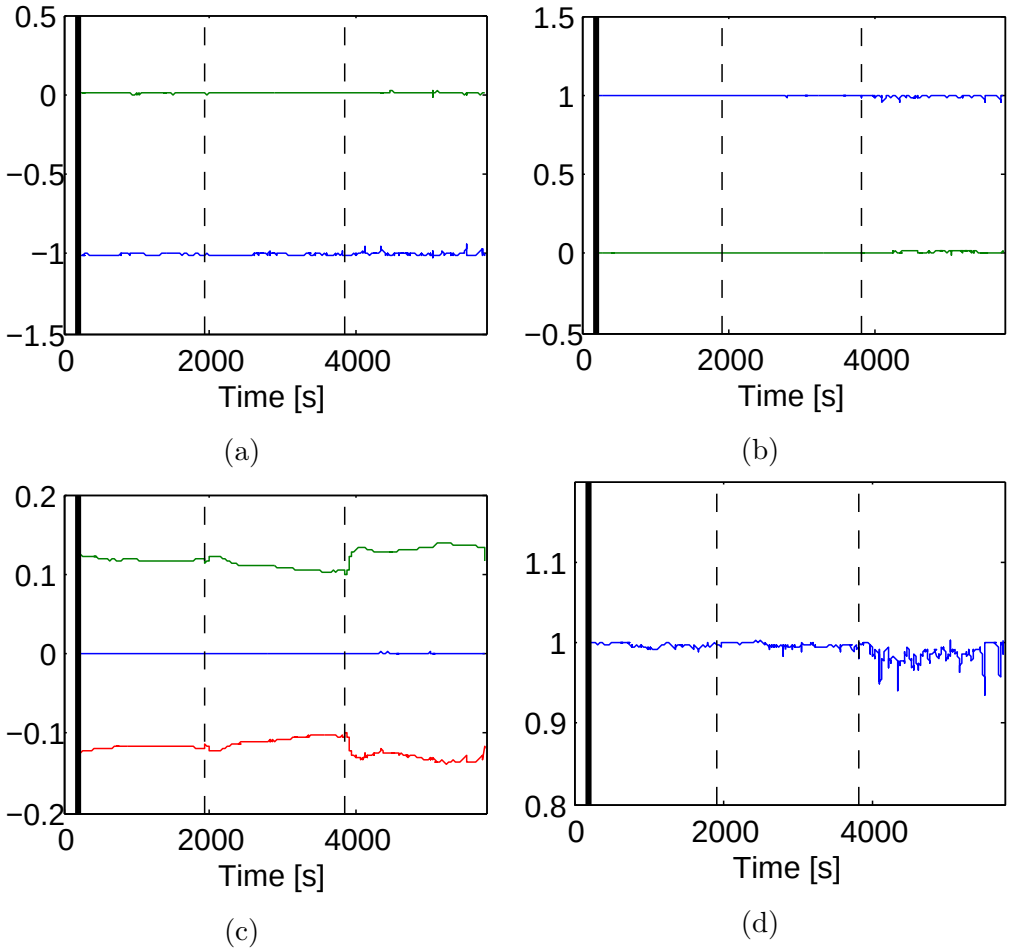

Figure 3.14: Estimated parameters of linear model component in the voltage model. (a) denominator coefficients; (b) pole locations; (c) numerator coefficients; (d) zero locations.

Applying the model framework proposed in Section 3.5.1 and the corresponding estimation methods introduced in Section 3.5.2, a complete power delivery model is obtained through the approaches described as follows.

Voltage Model

In the example, a moving time frame of $N = 2000$ data points is used for parameter estimation at any given time k. Such implementation not only ensures the persistent condition mentioned in Section 3.5.2 is fulfilled, but also demonstrates the

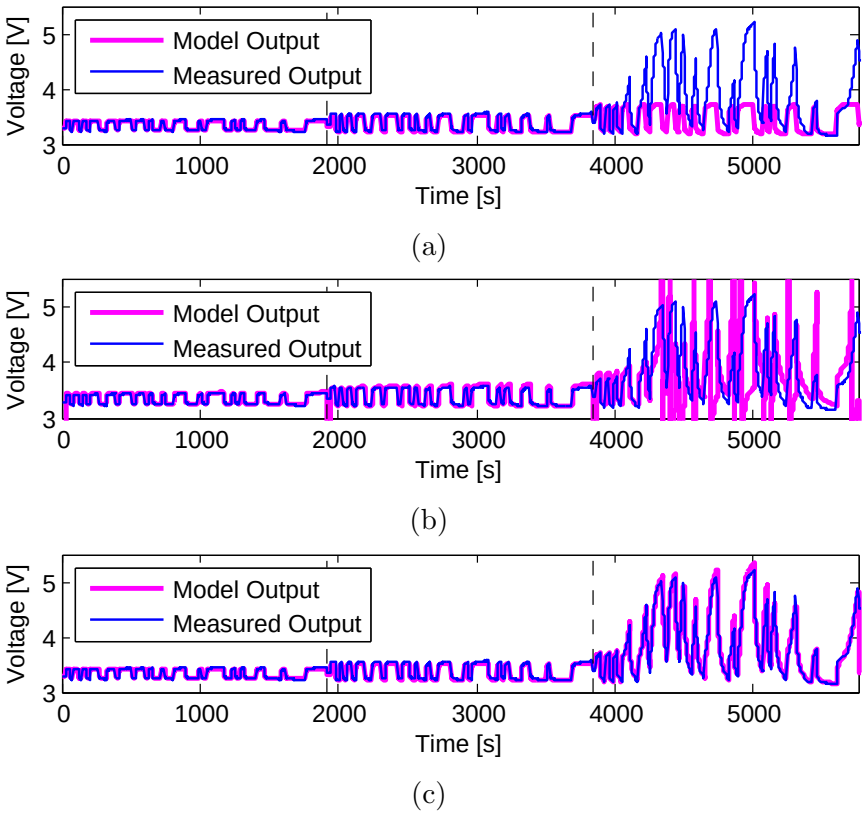

Figure 3.15: A comparison between different identified model components in the voltage model. (a) Hammerstein model; (b) Synthesizing Hammerstein model and the OCV characteristics; (c) Synthesizing Hammerstein model, the OCV characteristics, and hysteresis model.

feasibility of on-line recursive estimation of the model.

As indicated in Fig. 3.14, the estimated parameters of the linear regression model varies little in Region I and II, while the variance becomes large in Region III. In the estimation, no time delay is assumed, but the result $\hat{b}_0$, which is approximately 0 all the time, indicates that there is one time delay in the model. It also leads to the duplicated zero locations. The pole locations indicate that there is one fast dynamic phenomena and one slow dynamic phenomena.

The comparison given in Fig. 3.15 indicates the requirement of combining Hammerstein model, OCV characteristics, and Hysteresis model. To quantize the

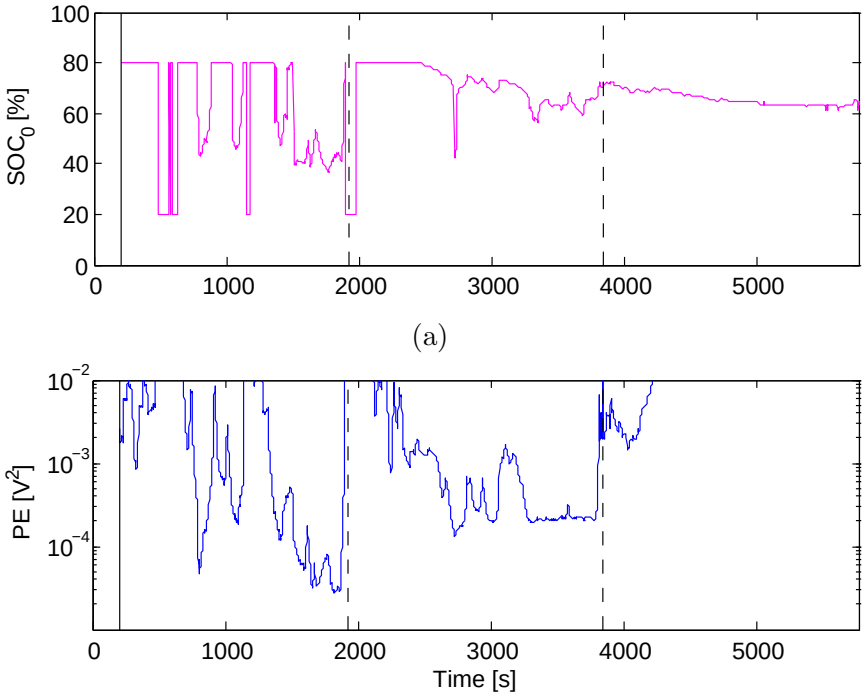

Figure 3.16: SOC estimation results. (a) Estimate of initial SOC at $t = 0$; (b) The minimum prediction error achieved via line search over $\text{soc}_0(T)$.

performance of obtained models, define the standard estimate error

$$\sigma_{\text{est}} = \frac{1}{\sqrt{N}} \left\| \widehat{\mathbf{Y}} - \mathbf{Y} \right\|, \tag{3.71}$$

where $\widehat{\mathbf{Y}}$ contains N model outputs, $\mathbf{Y}$ contains N measured outputs at the same given time series.

The comparison of σ_{est} between different combinations for the voltage model in Region III is summarized in Table 3.2.

With a single Hammerstein model, the simulate output is acceptable during Region I and II. However, the extension of the linear model with the non-linear OCV and hysteresis effect significantly improves the performance of the obtained model, especially in Region III where both a high C-rate and overcharging of the

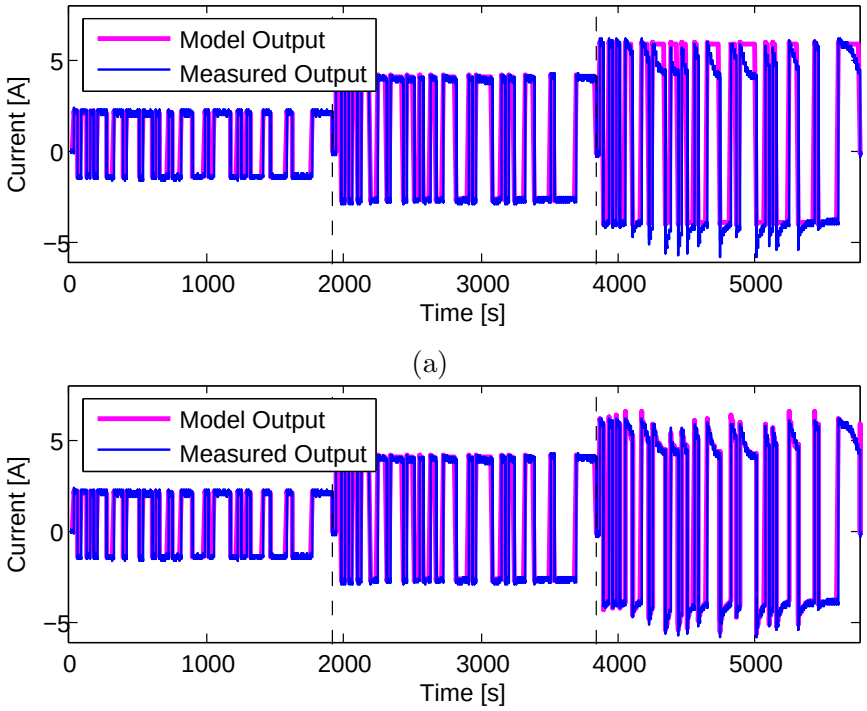

(a)

(b)

Figure 3.17: A comparison between different identified model components in the current model. (a) Hammerstein model; (b) Synthesizing Hammerstein model and hysteresis model.

battery is observed in the data. It actually provides potential possibility to extend the application range of a battery system, since the dynamic behavior can be predicted sufficiently well for proper control.

The SOC estimation result is also obtained as shown in Fig. 3.16. The search range with respect to initial SOC is restricted within $[20\%, 80\%]$, which can be adjusted accordingly in practice. In Region I, the estimation is not reliable, since the

Table 3.2: σ_{est} in Region III of Voltage Model

$\bar{v}(k)$	0.596V
$\bar{v}(k) + \tilde{v}_1(k)$	24.047V
$\bar{v}(k) + \tilde{v}_1(k) + \tilde{v}_2(k)$	0.080V

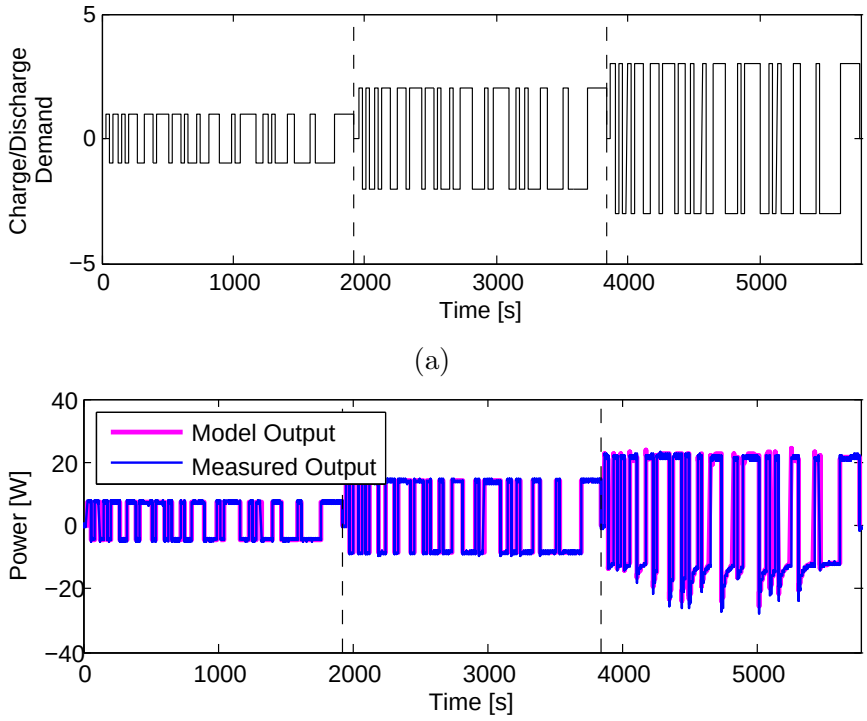

Figure 3.18: The output of the completed estimated power model with the charge/discharge demand as the input.

battery is operating in a range where the OCV is fairly flat as shown in Fig. 3.12. It is a common problem observed in the application of $LiFePO_4$ batteries. In the middle of Region II, the estimated initial SOC eventually converges to a certain value, while the prediction error also decreases. It can be concluded that the simple SOC estimation based on voltage dynamics performs better while operating in the region where OCV changes more significantly due to changes of SOC.

Current Model

Similar to the identification of voltage model, the current model composed by only Hammerstein model is sufficient for Region I and II, but failed to capture the dynamics in Region III. Through the addition of the Takacs hysteresis model,

Table 3.3: σ_{est} in Region III of Current Model

$\bar{i}(k)$	0.727A
$\bar{i}(k) + \tilde{i}(k)$	0.139A

the current model is able to capture all dynamics through Region I, II, and III, as shown in Fig. 3.17. Also Table 3.3 indicates a better fit with the compensation of the hysteresis model, especially in Region III.

Power Model

By combining the output of voltage model and current model, a completed power storage and delivery model with an input of charge/discharge demand is obtained as shown in Fig. 3.18. The result validates that the estimated model is able to capture non-linear power dynamics, even in Region III when battery is over-charged. σ_{est} of the power model in Region III and all regions are 0.741 W and 0.477 W, respectively. The result depicted in Fig. 3.18 is powerful: both voltage and current data can be combined to reliably predict power dynamics.

3.6 Acknowledgment

Chapter 3, in part, is based on the material that appears in Proceedings of American Control Conference (ACC) 2013, Pages 1908–1913. Zhao, Xin; de Callafon, Raymond A.. "Data-based Modeling of a Lithium Iron Phosphate Battery as an Energy Storage and Delivery System." The dissertation author was the primary author of this paper.

Chapter 3, in part, is based on the material that appears in Applied Energy,

vol. 180, Pages 823–833. Zhao, Xin; de Callafon, Raymond A.. "Modeling of Battery Dynamics and Hysteresis for Power Delivery Prediction and SOC Estimation." The dissertation author was the primary author of this paper.

Chapter 4

Current Scheduling for Parallel-Connected Electrical Energy Storage System

4.1 Introduction

Electrical energy storage and delivery systems (EESDS) are important in industrial applications that include power grids, second life battery systems, and electric vehicles [58, 59, 60] with intermittent power delivery demands. The development of high-performance battery cells [7] and advanced battery management technologies [30] make batteries critical components in enhancing the performance of EESDS.

As the bus voltage of an EESDS is typically constrained, a parallel connection of battery modules is a solution to increase the energy storage capability and the delivered power. For instance, in Battery Electric Vehicles (BEV), the power-train is driven purely by electric power, thus a parallel battery architecture is especially

needed to fulfil the capacity and power requirements to ensure an acceptable range and the performance of vehicles [61]. Similar parallel connection of batteries with different operating parameters can be found in second life applications to provide ancillary grid services.

Currently, parallel battery modules are mostly formed as one compact pack, which is applicable for small-scale applications such as portable devices. However, a compact battery pack employed in the large-scale implementation results in a maintenance problem, that is, replacing a portion of the battery pack is either not feasible or fairly complicated in practice. While the technology of fast charging battery cells is evolving quickly [8], there still exists some significant challenges for fast charging large-scale battery packs [62].

A battery architecture with exchangeable modular and parallel connected batteries is a promising solution for increasing storage capacity. Instead of forming all the battery cells into one pack, the pack is sectioned into several independent modules that are designed to be exchangeable. Multiple such modules are connected in parallel onto the bus, as shown in Fig. 4.1. With the implementation of such architecture, the robustness of the battery system is enhanced significantly: when a cell or a module failure occurs, a portion of the battery pack is exchangeable, which also reduces the cost of maintenance. Furthermore, the possibility of rapidly exchanging battery modules shortens the wait time to obtain a fully-charged battery system, which is a critical requirement for the feasibility of long-distance travel with a BEV.

The exchangeable modular battery architecture poses several challenges for the battery management system. By replacing one or multiple battery modules, each module may have different SoCs, i.e., the ratio of the instantaneous battery capacity

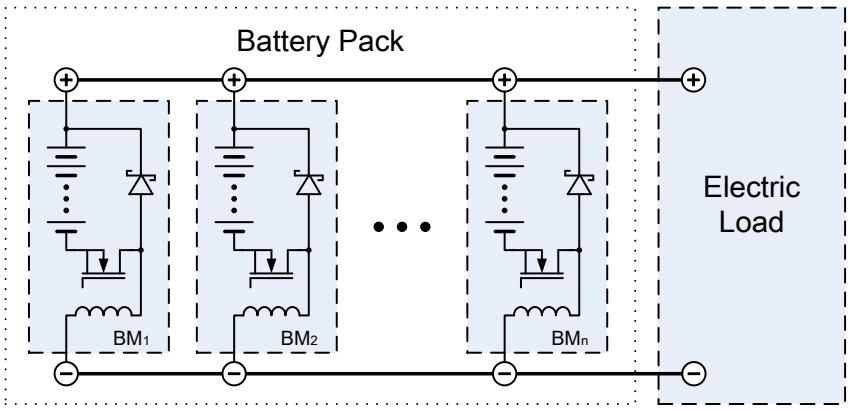

Figure 4.1: System diagram of parallel buck regulated battery modules.

over its nominal capacity. Furthermore, the cells of each module may be built with different materials, thus have different electrochemical characteristics such as charging and discharging profiles [63]. These challenges lead to scheduling issues when charging or discharging battery modules. In addition, the internal impedance in each battery module causes power loss, hence the control of these modules can also be formulated as an optimization problem to minimize energy loss that can be solved by Quadratic Programming (QP) [64, 65], Semidefinite Programming (SDP) [66], depending on the constraints taken into consideration.

There exist several solutions to similar scheduling problems in the literature. For instance, a thorough solution of a stand-alone energy storage system with parallel battery architecture is proposed via on/off switching control in Kaiser's [67]. The approach in this paper, however, provides a new level of control by actively managing the individual power flow of each module via Pulse-Width Modulation (PWM) control. In the paper, the battery system is first modeled for current scheduling. Then the scheduling algorithms under constrained DC bus voltage are introduced, including simultaneous, sequential, and hybrid algorithms for discharge scheduling. Finally, the scheduling algorithms are simulated in a dynamic power demand simulation using

a driving profile of a BEV.

4.2 Problem Formulation

4.2.1 Model Formulation

In this paper, the current scheduling of parallel battery modules is executed by buck regulators, which is composed by a pulse-width modulated MOSFET, a fly-by diode, and an inductor, as indicated in Fig. 4.1. In each battery module, the battery cells are connected in series and then buck regulated. Several such battery modules are connected in parallel by DC bus, which ultimately form a battery pack and is connected to the electric load.

Notice that the number of modules n is arbitrary, which means that the battery pack can be fully or partially loaded with battery modules. This feature further enhances the flexibility of the application of such battery system.

For the derivation of the current scheduling algorithm, the system of parallel buck regulated battery modules is approximated as a parallel connection of adjustable power supplies, as indicated in Fig. 4.2. Specifically, each battery module with a serial of multiple cells is modeled as two components in serial: an ideal battery with an open-circuit voltage $V_{OC,i}$ and an internal resistance R_i [68], where $i = 1, 2, \ldots, n$, which essentially influences the current scheduling. The open-circuit voltage is buck regulated to a lower voltage

$$V_i = D_i \cdot V_{OC,i}$$

where D_i is the PWM duty cycle of MOSFET, and $D_i \in [0, 1]$.

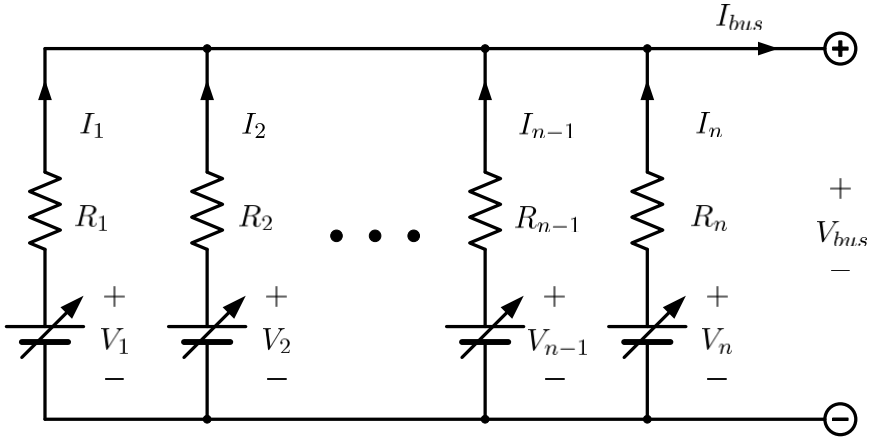

Figure 4.2: Model for current scheduling.

4.2.2 Formulation of Constraints

With the formulated model, the system constraints can be derived. Applying Kirchhoff's laws yields

$$V_i - R_i \cdot I_i + R_{i+1} \cdot I_{i+1} - V_{i+1} = 0 \tag{4.1}$$

where $i = 1, 2, \ldots, n-1$, and

$$V_n - R_n \cdot I_n - V_{bus} = 0 \tag{4.2}$$

$$\sum_{i=1}^{n} I_i = I_{bus} \tag{4.3}$$

(4.1) - (4.3) formulate the fundamental equalities for the system. In addition, there exist inequality constraints in the system. Since $D_i \in [0, 1]$, the voltage constraint for each battery module is:

$$0 \leqslant V_i \leqslant V_{OC,i} \tag{4.4}$$

Furthermore, there also exists the current constraint for each module due to the limitations of the battery cells:

$$0 \leqslant I_i \leqslant I_i^{\max} \tag{4.5}$$

Notice that the inequality constraints are intended to be independent for each module, since the current scheduling is aimed to be applicable for implementation on battery modules with different operating parameters such as SoC, internal resistance and moreover, with different electrochemical features.

Accordingly, the current scheduling is generally to determine the feasible solution that is subject to (4.1) - (4.3) with the constraints (4.4) and (4.5). The constraints are subject to change depending on the actual system design.

4.3 Current Scheduling Algorithms under Constrained DC Bus Voltage

In some applications, the electric load imposes constraints on the DC bus voltage:

$$V_{bus}^{\min} \leqslant V_{bus} \leqslant V_{bus}^{\max} \tag{4.6}$$

In practice, the SoC of each module is evaluated and utilized as a crucial reference [69, 70]. Therefore, the SoC of each module is taken into account while determining the scheduling strategy. Furthermore, the real-time SoC and internal resistance can be estimated and applied for control purpose [71], which enables the implementation of on-line scheduling.

4.3.1 Simultaneous Discharge (SimD) Scheduling

The SimD scheduling is defined by a current of each module scheduled according to

$$I_i = \alpha_i \cdot I_{bus} \tag{4.7}$$

where the current scheduling ratio α_i is given by

$$\alpha_i = \frac{\mathrm{SoC}_i}{\sum_{i=1}^{n} \mathrm{SoC}_i}. \tag{4.8}$$

It means that the modules with higher SoC are scheduled to deliver more current, while the ones with lower SoC can operate at a relatively low rate. Intuitively, all the modules ultimately deplete completely at the same time. Clearly the SimD scheduling causes a simultaneous and constant current delivery for each module when the bus current is required to be constant.

By (4.1) and (4.2), once the current of each module I_i is determined, the buck regulated voltage of each module V_i is essentially determined by V_{bus}:

$$V_i = V_{bus} + R_i \cdot I_i \tag{4.9}$$

where $i \in \{1, 2, \ldots, n\}$ and V_{bus} is constrained by (4.6).

Toggling the MOSFETs introduces undesirable parasitic power loss and decreases the module efficiency, hence at least one MOSFET should be set to operate in the full duty cycle, that is, to find a feasible solution under the equality constraint $V_i = V_{OC,i}$, which is transformed from one of the inequality constraints (4.4).

The SimD scheduling is illustrated by a constant current demand simulation

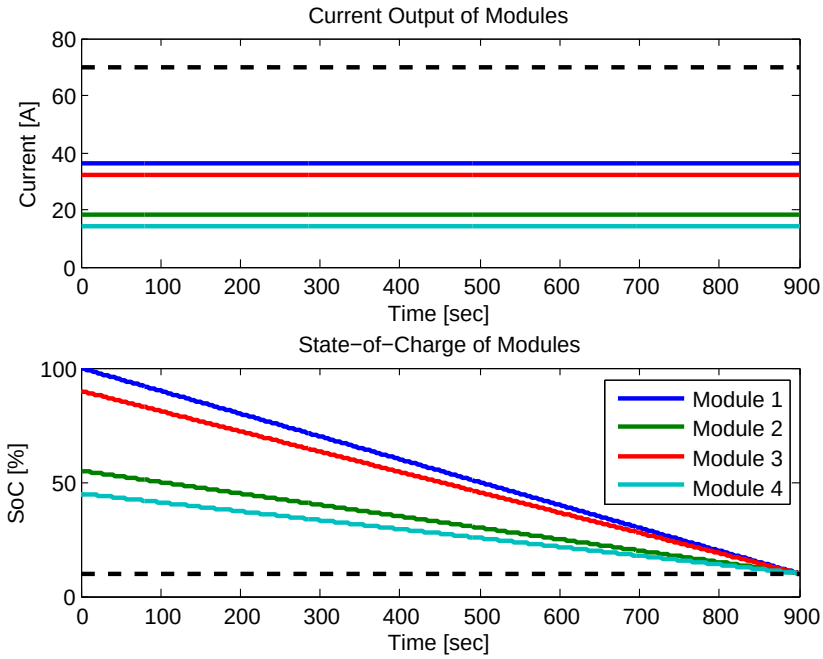

Figure 4.3: SimD scheduling for constant current demand with current in each module in top figure and SoC in bottom figure. Dashed lines indicate constraints.

as shown in Fig. 4.3. The desired bus current is 100A. Initially, the SoC of the modules are 100%, 55%, 90%, and 45%, respectively in this illustration. Although such different initial SoCs is not quite realistic in most operating conditions, it is easier to distinguish for demonstration purposes. Moreover, such conditions may exist, for instance, in second life applications for used EV battery modules.

The SoC threshold for discharge is set to 10%, hence the current of each module is determined by (4.7) with available SoC. Furthermore, the OCV and internal resistance of each module is assumed to vary linearly with the SoC in the simulation. Specifically, the OCV decreases and the internal resistance increases as the battery discharges. As expected, all the modules are completely discharged at the same time, and the proportion of SoC between each module is the same along the battery discharge.

4.3.2 Sequential Discharge (SeqD) Scheduling

Battery modules do not necessarily have to be discharged in a simultaneous pattern and an alternative SeqD scheduling can be used to discharge battery modules sequentially. Such algorithm aims to deplete the battery modules one by one. Specifically, SeqD scheduling starts depleting the module with the lowest SoC. If the output current of the module with the lowest SoC is lower than the required bus current, then the modules are iteratively implemented one after another till the current demand is fulfilled.

The SeqD scheduling is also demonstrated by a constant current demand simulation as shown in Fig. 4.4. The conditions of each module are the same as in the simulation for SimD. The desired bus current is still 100A. Since the maximum output current of the modules is set to 70A, one module is not able to fulfil the current demand. Starting with the discharging of Module 4, the modules are discharged one by one. For instance, at 350 seconds, Module 4 and Module 2 are discharged to the minimum level of 10% SoC while Module 3 has relatively high SoC and Module 1 is still fully-charged. Therefore, by replacing two out of four modules, a fully charged battery pack is obtained, demonstrating the usefulness of the SeqD scheduling.

However, the number of functioning modules decreases as more modules are completely discharged, which results in the infeasibility of fulfilling high current demand. In the constant current demand simulation, three modules stop functioning after approximately 680 seconds. Although the remaining module operates at the maximum output current, the bus current demand cannot be achieved. Therefore the operation of battery system is terminated. This is considered to be the drawback of such scheduling algorithm, since it sacrifices the power capability, especially when

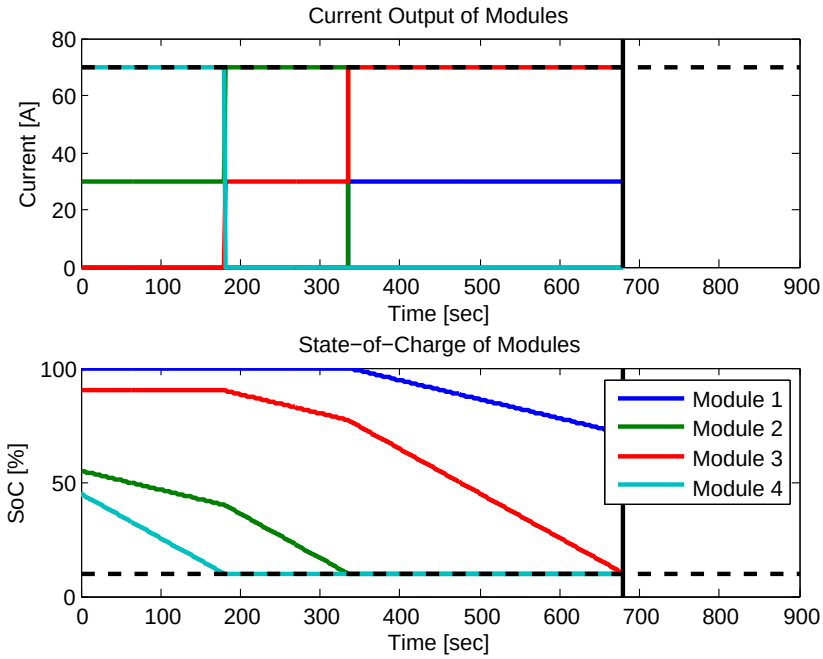

Figure 4.4: SeqD scheduling for constant current demand with current in each module in top figure and SoC in bottom figure. Dashed lines indicate constraints.

a large portion of modules are out of service. But the SeqD algorithm is still useful for some applications with relatively low power demand and the possibility of frequent exchange of battery modules, such as the daily urban transportation by BEV, since a fully-charged battery pack can be obtained by exchanging a portion of the modules rather than all of them.

4.3.3 Hybrid Discharge (HybD) Scheduling

Since there exists power loss due to internal resistance:

$$P_{\text{loss}} = \sum_i (I_i^2 R_i) \tag{4.10}$$

the current scheduling can take account of such power loss to motivate a scheduling that aims to minimize the power loss in (4.10).

Introducing slack variables u_i, l_i, w_1, w_2, (4.4), (4.5), and (4.6) can be rewritten as:

$$V_i + u_i = V_{OC,i}, \quad V_i \geqslant 0, \quad u_i \geqslant 0$$

$$I_i + l_i = I_i^{\max}, \quad I_i \geqslant 0, \quad l_i \geqslant 0$$

$$V_{bus} + w_1 = V_{bus}^{\max}, \quad w_1 \geqslant 0$$

$$V_{bus} - w_2 = V_{bus}^{\min}, \quad w_2 \geqslant 0$$

where $i \in \{1, 2, \ldots, n\}$. The unknowns can be grouped into $x \in \mathbb{R}^{4n+3}$: $x = \begin{bmatrix} x_1^T & x_2^T & x_3^T & x_4^T & x_5^T \end{bmatrix}^T$, where

$$x_1 = \begin{bmatrix} V_1 & V_2 & \cdots & V_n \end{bmatrix}^T, \quad x_2 = \begin{bmatrix} I_1 & I_2 & \cdots & I_n \end{bmatrix}^T$$
$$x_3 = \begin{bmatrix} u_1 & u_2 & \cdots & u_n \end{bmatrix}^T, \quad x_4 = \begin{bmatrix} l_1 & l_2 & \cdots & l_n \end{bmatrix}^T$$
$$x_5 = \begin{bmatrix} V_{bus} & w_1 & w_2 \end{bmatrix}^T$$

Thus, all the equality and inequality constraints for the system can be formulated into:

$$Ax = b, \quad x \geqslant 0$$

where $A \in \mathbb{R}^{(3n+3)\times(4n+3)}$:

$$A = \begin{bmatrix} A_1 & A_2 & 0 & 0 & A_3 \\ I & 0 & I & 0 & 0 \\ 0 & I & 0 & I & 0 \\ 0 & 0 & 0 & 0 & A_4 \end{bmatrix}$$

and

$$A_1 = \begin{bmatrix} 1 & -1 & 0 & \cdots & 0 \\ 0 & 1 & -1 & \cdots & 0 \\ \vdots & \vdots & \ddots & \ddots & \vdots \\ 0 & 0 & \cdots & 1 & -1 \\ 0 & 0 & \cdots & 0 & 1 \\ 0 & 0 & \cdots & 0 & 0 \end{bmatrix}$$

$$A_2 = \begin{bmatrix} -R_1 & R_2 & 0 & \cdots & 0 \\ 0 & -R_2 & R_3 & \cdots & 0 \\ \vdots & \vdots & \ddots & \ddots & \vdots \\ 0 & 0 & \cdots & -R_{n-1} & R_n \\ 0 & 0 & \cdots & 0 & -R_n \\ 1 & 1 & \cdots & 1 & 1 \end{bmatrix}$$

$$A_3 = \begin{bmatrix} 0 & \cdots & 0 & -1 & 0 \\ 0 & \cdots & \cdots & \cdots & 0 \\ 0 & \cdots & \cdots & \cdots & 0 \end{bmatrix}^T$$

$$A_4 = \begin{bmatrix} 1 & 1 & 0 \\ 1 & 0 & -1 \end{bmatrix}$$

The internal resistance of each module $R_i \in \mathbb{R}_+$, therefore it can be verified that A has full rank. Furthermore, since $R_i \in \mathbb{R}_+$, Q is positive semidefinite, the current scheduling can be formulated as a Quadratic Programming (QP) problem:

$$\begin{aligned} \text{minimize} \quad & q(x) = \frac{1}{2} P_{\text{loss}} = \frac{1}{2} x^T Q x \\ \text{subject to} \quad & Ax = b, \\ & x \geqslant 0. \end{aligned}$$

where $Q \in \mathbb{S}^{4n+3}$:

$$Q = \begin{bmatrix} 0 & & & & \\ & R & & & \\ & & 0 & & \\ & & & 0 & \\ & & & & 0 \end{bmatrix}$$

and

$$R = \begin{bmatrix} R_1 & 0 & \cdots & 0 \\ 0 & R_2 & \cdots & 0 \\ \vdots & \vdots & \ddots & \vdots \\ 0 & 0 & \cdots & R_n \end{bmatrix}$$

Due to the convexity of the QP, the minimization of (4.10) under constraints is solvable by algorithms such as Path-Following algorithm, Potential-Reduction algorithm [65], or Reflective Newton method [72].

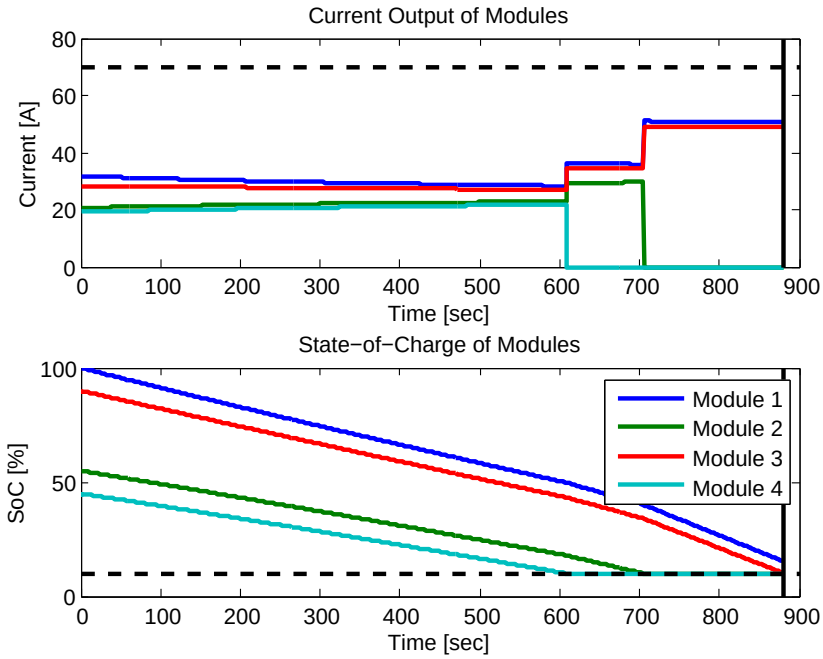

Figure 4.5: HybD scheduling for constant current demand with current in each module in top figure and SoC in bottom figure. Dashed lines indicate constraints.

The constant current demand simulation is executed with the scheduling introduced above and results are shown in Fig. 4.5. It is observed that the battery modules deplete in a sequential pattern and the range increases by 29% comparing with the terminate time of SeqD scheduling. Such scheduling algorithm balances the range and the depleting mode, hence it is called Hybrid Discharge (HybD) scheduling. On the basis of all the constant current demand simulations, the total energy losses due to internal resistance for the first 600 seconds are listed in Table 4.1. SeqD scheduling results in the largest energy loss since at least one module is operating at the maximum output current at a time. The energy loss is decreased from SimD scheduling to HybD scheduling. Considering that the internal resistance given in the simulation is in the order of several mΩ, the decrease of approximately 7% is noteworthy.

Table 4.1: Comparison of Energy Losses

Current Scheduling Algorithm	Energy Loss (kJ)
SimD scheduling	177.67
SeqD scheduling	417.67
HybD scheduling	165.36

4.4 Dynamic Power Demand Simulation for Current Scheduling Algorithms

In the previous section, a constant current demand test is utilized for demonstration of the different current scheduling algorithms. Even for dynamic current demand cases, the three proposed algorithms are solvable. For that purpose, we also consider applying these algorithms to dynamic power demand cases, which are required in applications with intermittent power delivery demands such as BEVs.

The EPA Urban Dynamometer Driving Schedule (UDDS) is applied to demonstrate the current scheduling for a variable power demand as indicated in Fig 4.6. The driving schedule includes the vehicle speed information along a virtual urban route, the derivative of which can be considered as the sum of vehicle accelerations driven by powertrain and slope. Given the acceleration, the power demanded by the vehicle can be calculated by the propulsion equation of vehicles:

$$P_{des} = (M \cdot a + C_r \cdot M \cdot g + C_a \cdot \frac{A}{21.15} \cdot v^2) \cdot v \tag{4.11}$$

where M is the mass of the vehicle, a is the required acceleration, C_r is the coefficient of rolling, g is the gravity constant, C_a is the coefficient of air resistance, A is the frontal area of the vehicle, v is the required velocity of the vehicle.

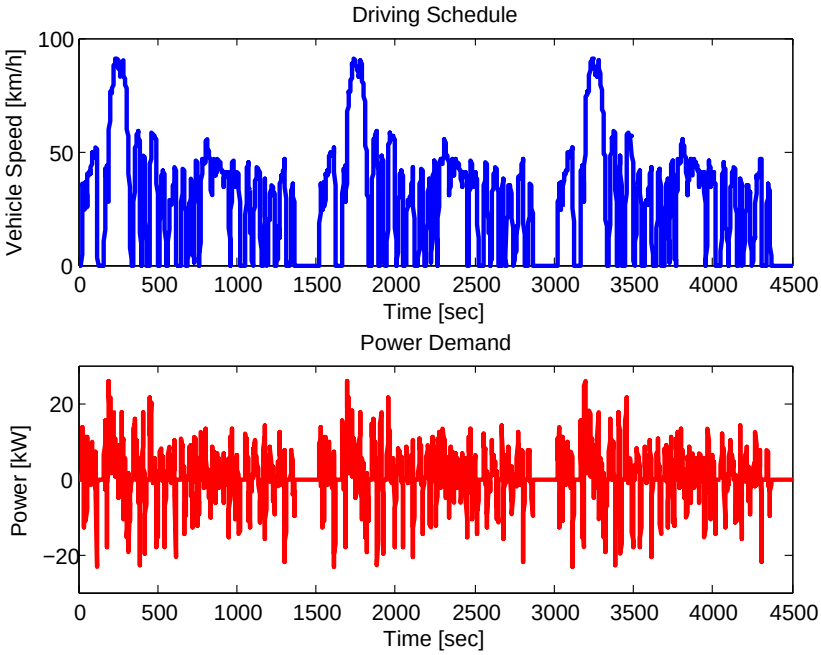

Figure 4.6: Driving profile and power demand (UDDS).

The desired power demand is for the entire battery system, since V_{bus} and I_{bus} are uncertain, we have:

$$V_{bus} \cdot I_{bus} = P_{bus} = P_{des} \tag{4.12}$$

Due to the product of the unknown bus voltage and current, current scheduling is more challenging, but can be solved for the SimD and SeqD scheduling trivially.

For SimD scheduling, by (4.2) and (4.7), assuming $V_n = V_{OC,n}$ yields:

$$V_{OC,n} - \alpha_n \cdot R_n \cdot I_{bus} = V_{bus} \tag{4.13}$$

Combining (4.12) and (4.13), the bus current can be obtained by solving a quadratic equation:

$$I_{bus} = \frac{V_{OC,n} \pm \sqrt{V_{OC,n}^2 - 4 \cdot P_{des} \cdot \alpha_n \cdot R_n}}{2 \cdot \alpha_n \cdot R_n} \tag{4.14}$$

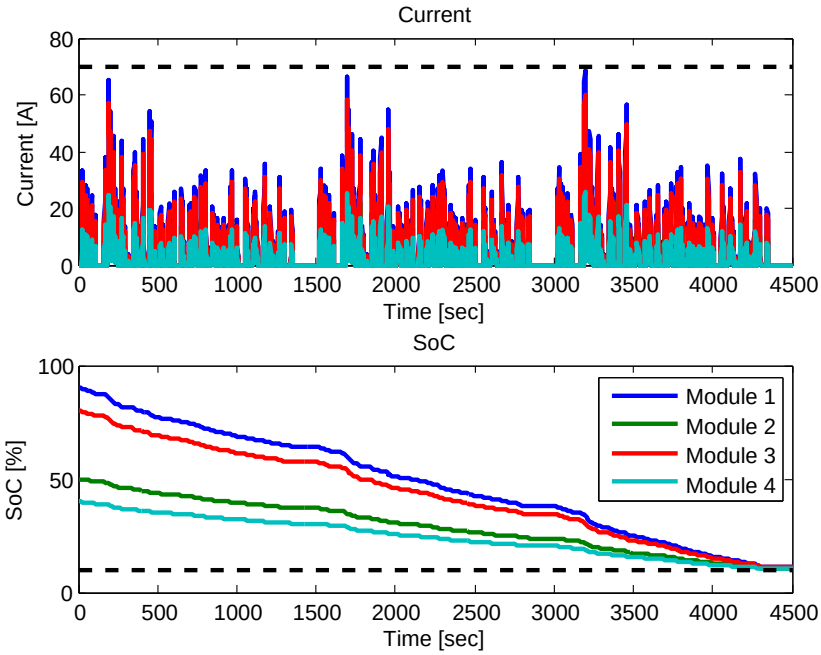

Figure 4.7: SimD Scheduling for Dynamic Power Demand.

Thus, the bus voltage V_{bus} can also be determined. If there exists no feasible solution due to the inequality constraints (4.4) - (4.6), then it is assumed that other modules operate at the full duty cycle and resolve (4.14) iteratively.

For SeqD scheduling, when one battery module with the lowest SoC cannot fulfil the power demand, more modules can be iteratively implemented. For the implemented modules, the current of each module can also be determined by (4.14).

The simulation results for the SimD and SeqD scheduling algorithms are summerized in Fig 4.7 and Fig 4.8. The results indicate the feasibility of the scheduling algorithms, where the SimD scheduling depletes all the modules at the same time, while the SeqD scheduling discharges the modules in a sequential manner.

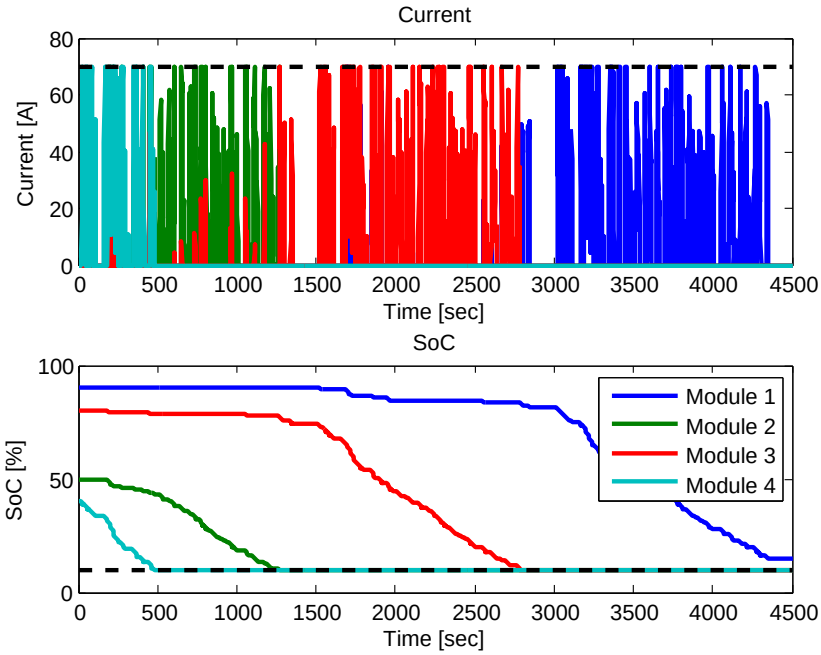

Figure 4.8: SeqD Scheduling for Dynamic Power Demand.

4.5 Development of Parallel-Connected Modular Battery System for Electric Vehicle

A parallel-connected modular battery system for Electric Vehicle (EV), named Modular Battery Exchange and Active Management (M-BEAM) system, is developed for experimental validation purposes of the proposed scheduling algorithms and future research. As stated in its name, M-BEAM system is a battery system which is composed by modular batteries [73]. The output power flow of each battery module is controlled to optimize the entire system performance.

The circuit architecture of M-BEAM system is the same as the topology shown in Fig. 4.1. In each module, 48 lithium iron phosphate cells are connected in series. The specifications of a single cell and a module are summarized in Table 4.2. When operating at its nominal voltage, a battery module can have a continuous power

Table 4.2: Specifications of battery cell and module in M-BEAM system

Item	Specification (Cell)	Specification (Module)
Nominal Voltage	3.2V	153.6V
Internal Impedance	8mΩ	384mΩ
Max. Continuous Discharge Current	20A	20A
Max. Instant Discharge Current	50A	50A
Charge Cut-Off Voltage	3.65V	175.2V
Discharge Cut-Off Voltage	2.0V	96.0V

output up to 3kW and an instant power output up to 7.68kW.

4.5.1 Battery Management System

In the operation of a battery system, several critical parameters, including cell voltages, current, and temperatures, need to be monitored to ensure:

- Battery cells are not under-charged or over-charged;
- The charge or discharge rate of battery cells are within the nominal range;
- There is no thermal runaway occurring in the system.

These parameters can be monitored by a Battery Management System (BMS) as shown in Fig. 4.9 in real-time. To decrease the tolerance requirement for drain-to-source breakdown voltage of power switches, i.e. power MOSFETs, the battery cells are grouped into two banks. Therefore a pair of master-slave microprocessors is implemented to supervise the bottom and the upper bank, respectively. The cell voltages are measured then fused through multiplexers to maximize the usage of finite Analog-To-Digital (ADC) channels of microprocessors. Since all the battery cells in the module is in series, only the current measurement at the terminal is required.

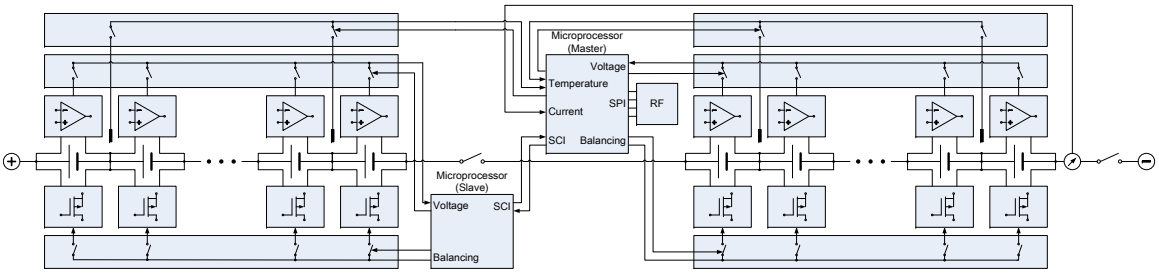

Figure 4.9: Circuit diagram of M-BEAM battery management system (BMS).

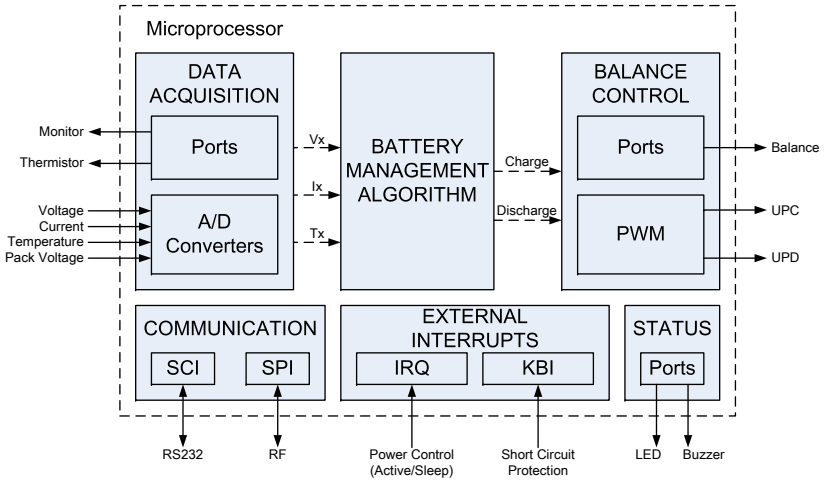

Figure 4.10: Functions and signals of master microprocessor in BMS.

The temperature is measured by thermistors located between battery cells.

The BMS also integrates a balancing circuit to adjust the charge current through individual cell so that the state-of-charge (SOC) of each cell can be balanced.

The battery management algorithm is executed in the master microprocessor. As depicted in Fig. 4.10, the processor acquires real-time measurements of voltages, current, and temperatures, then sends out charge and discharge control signals through digital output ports and PWM outputs.

An assembled battery module is shown in Fig. 4.11. The BMS is separated onto two boards for safety, quick assembly and design robustness.

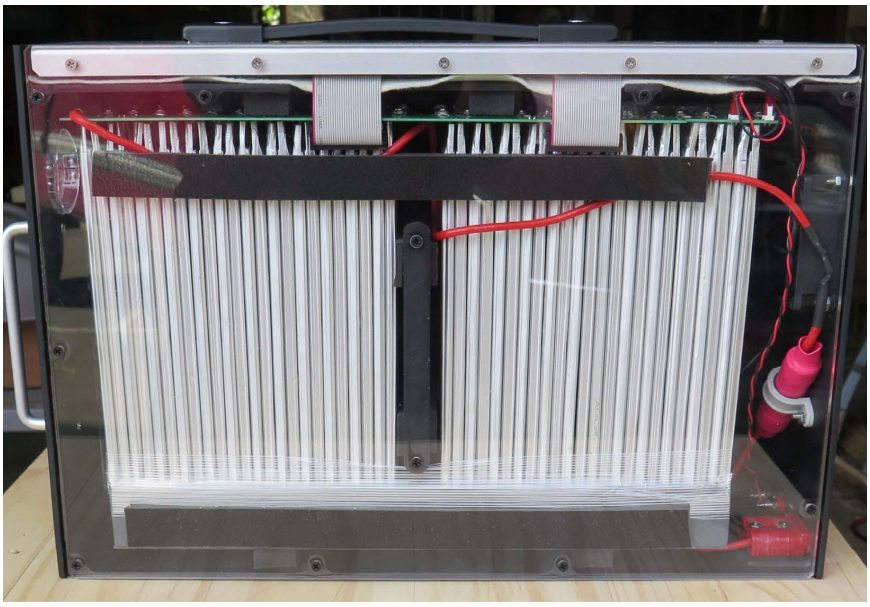

Figure 4.11: Photo of a M-BEAM battery module.

The BMS functionality and the performance of battery modules are tested through discharge-charge cycles after calibration. Fig. 4.12 shows a group of test results. The results indicate:

- All the cell voltages are close to each other in most of the SOC range, but deviate in the low and high SOC range.
- The temperatures measured during the entire cycle are moderate. Although the heat is accumulated during the discharge process, it is distributed evenly in the module and doesn't exceed 35°C at any location. The temperatures slowly converge to lower equilibrium along the charge process.

4.5.2 In-Vehicle Wireless Communication System

While several battery modules are connected, a communication network is required for monitoring the entire system and further coordinating output of each

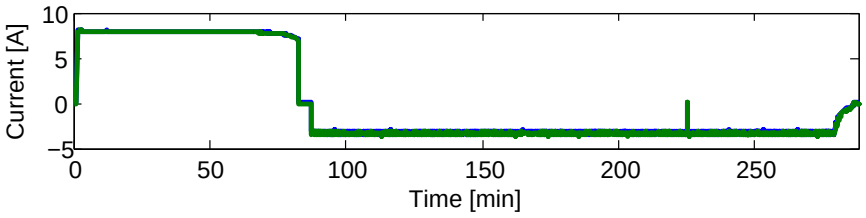

(a) 2 channels of current measurements (low/high resolution).

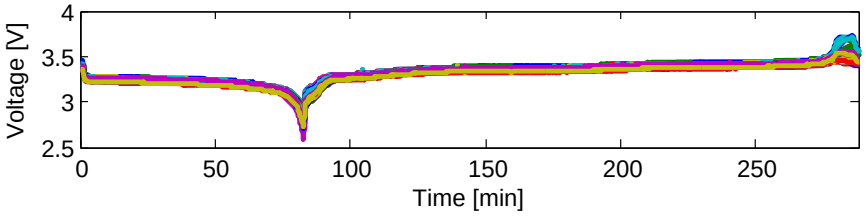

(b) 48 channels of cell voltage measurements.

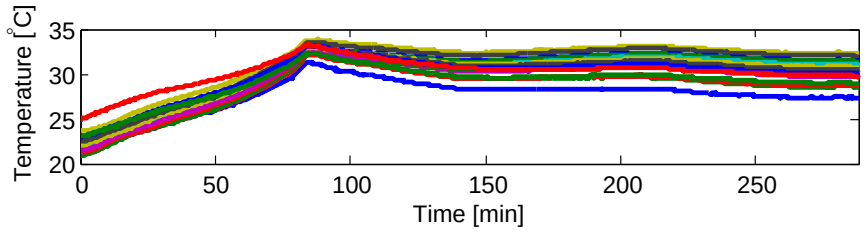

(c) 24 channels of temperature measurements.

Figure 4.12: The current, cell voltage, and temperature measurements of a M-BEAM battery module in a discharge-charge cycle.

module. In M-BEAM system, wireless communication is introduced to enhance the mobility of battery modules, since the physical wire connection for communication is eliminated. In particular, a star network based on IEEE 802.15.4 standard is developed to accommodate the cost. The transceiver employed can support 250kbps Offset-Quadrature Phase Shift Keying (O-QPSK) data transfer. To drive the transceivers within the network, Simple Media Access Controller (SMAC) is utilized in the firmware. Therefore each data packet has a maximum data length of 123 bytes.

Since the performance of in-vehicle wireless communication is crucial especially for coordinating distributed control, experiments are conducted on acquired data during test drives. To achieve that, the M-BEAM system is integrated into a

Figure 4.13: Photo of M-BEAM system being integrated into a converted EV.

converted EV as shown in Fig. 4.13.

To quantify the performance of wireless communication, the wireless data transmission success rate (WDTSR) of a battery module is defined as

$$\text{WDTSR} = \frac{N_s}{N_t}, \tag{4.15}$$

where N_s is the number of successfully delivered data packets, N_t is the number of total data packets expected to be delivered.

As depicted in Fig. 4.14, although most of the battery modules achieve a WDTSR above 85% at a low refreshing rate of 0.4Hz, some still suffer a low success rate. For instance, Module # 6 has a WDTSR as low as 78% in Test Drive No. 2, 5, and 6.

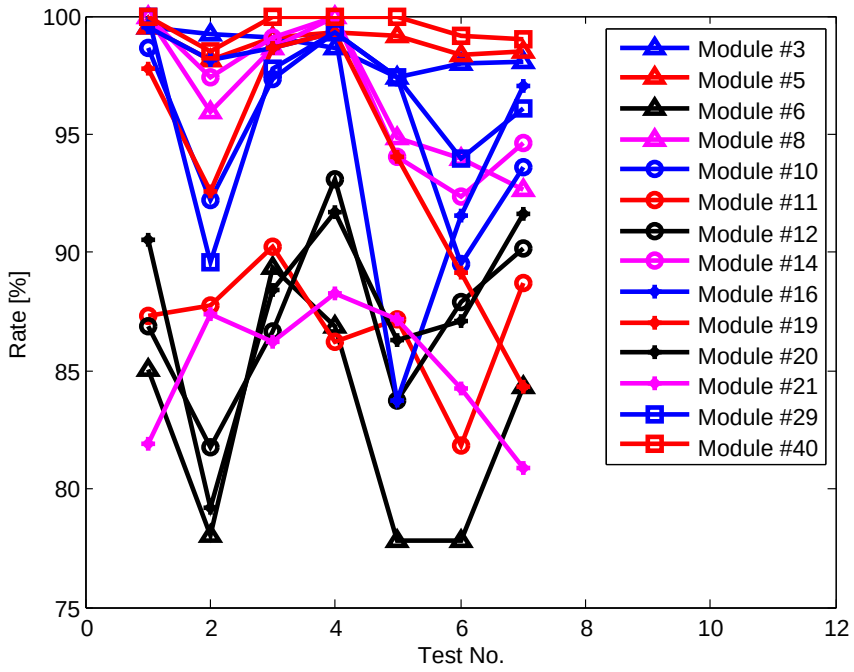

Figure 4.14: WDTSR of 14 M-BEAM battery modules during 7 test drives.

4.6 Open Problems

Although extensive work has been conducted to develop the experimental setup, the following research tasks are expected to be completed in the next phase.

- Power scheduling for parallel-connected battery systems, instead of only current scheduling, needs to be addressed, since the entire energy transformation is essentially of interest. In Section 4.4 two scheduling algorithms SimD and SeqD have been extended to be applied for power scheduling. The HybD scheduling needs to be re-formulated and solved by a different programming algorithm in order to be applied for power scheduling.

- The feasibility and performance of executing the proposed scheduling algorithms in an actual system with the given topology depends on proper control of the actuator, which is done by the PWM signal applied to MOSFETs in buck

regulation circuits of each module. As a typical control design cycle, first the possibility of an open-loop control law needs to be addressed, then a closed-loop control should be considered if either the open-loop control is unfeasible or the control performance needs to be improved. Since the actuators in such system are distributed, some issues such as synchronization in the controller design of a distributed control system should be addressed. This can be done through simulations first, then validation by bench tests on a small-scale experimental setup, and finally in-vehicle tests.

- The wireless communication performance of the system needs to be improved. It can be achieved by up-to-date wireless communication platforms and/or optimizing the physical locations of the base station and battery modules.

4.7 Acknowledgment

Chapter 4, in part, is a reprint of the material as it appears in Proceedings of IFAC World Congress 2014, Pages 2112–2117. Zhao, Xin; de Callafon, Raymond A.; Shrinkle Lou. "Current Scheduling for Parallel Buck Regulated Battery Modules." The dissertation author was the primary author of this paper.

Chapter 5

Control for Mitigation of AC Power Flow Fluctuations

5.1 Motivation

As more renewable energy generation is added to the utility grid, less conventional generation will be required to meet the power demand. Photovoltaics (PV), the major way of converting sunlight into electricity, is a fast-growing technology doubling its worldwide installed capacity every couple of years due to its scalability from small, residential and commercial rooftop or building integrated installations, to large utility-scale solar plants. Typically, solar energy generation uses (3 phase) inverters that have fast dynamics and exhibit very little inertia in terms of power delivery onto the utility grid.

Utilizing more renewable energy generation leads to inherent variability in energy production. However, it also reduces the rotational inertia in the form of spinning rotational mass from conventional generation that tends to stabilize and

maintain synchronous operation of the system [74]. This could result in increasing instability and poorly damped oscillations in AC frequency and power, unless additional conventional generating sources are placed on-line or less renewable resources are installed.

Such circumstances have been detected in practice and installation of Phasor Masurement Units (PMU) facilitate real-time measurements of power quality and power oscillations in an electricity grid. An example of such power oscillations can be observed in Fig. 5.1, where oscillations in real power were observed in the 12kV connections at the University of California during a particular load switching [75].

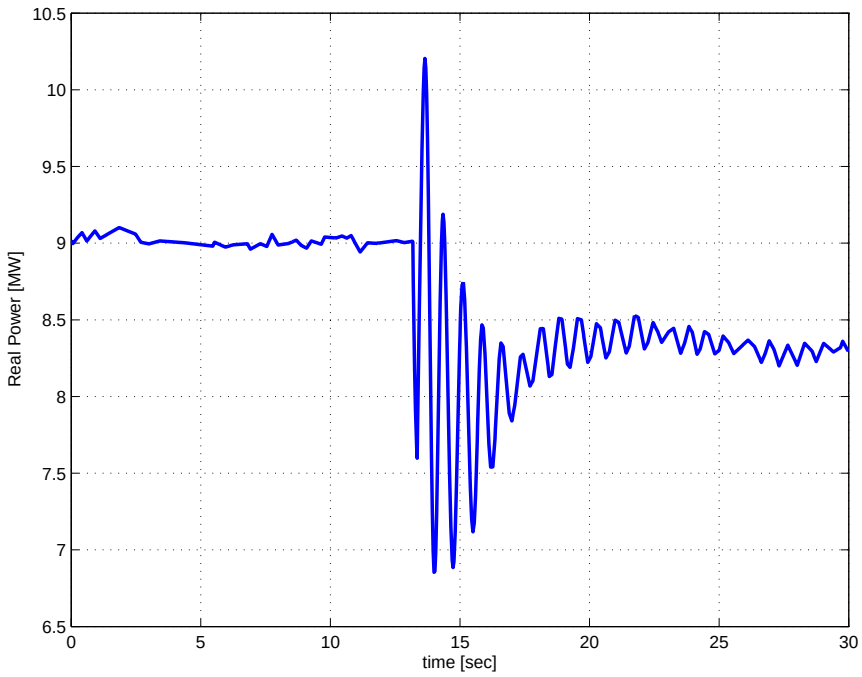

Figure 5.1: Measured real power oscillation on the main 3 phase interconnect of the UCSD Micro-Grid during a step-wise load demand change.

In general, electric power systems are subjected to power oscillations due to the inherent inertia of generators and loads connected on the electric grid [74, 18]. Such power oscillations are typically in the 0.2-3 Hz range, depending on the size of the

(micro)grid and the characteristics of the interconnected power systems [76, 77]. Detecting fluctuations in power flow in an electric grid has been an active field of study to improve the resiliency of electric networks. Power swing detectors that can detect unstable power swings in several milli-seconds are crucial for relay operation [78]. In case of stable power oscillations, frequency and damping of electro-mechanical oscillations can be performed with a ring down analysis or a normal operation analysis. Assuming an unknown non-zero initial condition, eigenvalues or the frequency/damping of the observed power oscillations can be computed using the Pronys method for ring down analysis [79, 80, 81] assuming the power oscillation is a sum of sinusoids [82] or more advanced methods using wavelet transforms [83]. In these methods, power oscillation dynamics is found by fitting models on the free response of an observed stable power oscillation.

The disturbance causing power oscillations can be a line switching, load switching, a fault or anything else that may have a large impact on the power flow through the power system. As these disturbances are typically step disturbances, explicit information on the shape of the input signal that caused the power oscillation will be beneficial, especially when multiple step signals occur in close proximity in time. Explicit use of input and observed output signals via a system identification procedure [81, 84] will improve the quality of the models that capture the power oscillations.

Once disturbances occurred in the grid can be characterized by dynamic models, a feedback control can be designed and implemented to mitigate power oscillations caused by those disturbances. In this chapter, based on an experimental setup created to mimic a local grid network, a demonstrated feedback control design and implementation is completed through formulating control variables, characterizing components

by open-loop tests, standard optimal controller design, and closed-loop experiments.

5.2 Experimental Setup

In a PV generation system, PV panels are connected to the grid via an inverter to convert the generated DC power to AC power. A grid-tied inverter is usually applied to synchronize the output with the grid. According to such circuit topology, an experimental setup is built as shown in Fig. 5.2. For testing purposes, the PhotoVoltaic (PV) power source is temporarily replaced by a programmable DC power source. An EMI filter to reduce AC ground coupling and a Grid-Tied Inverter (GTI) to provide 3 phase AC power. The GTI is controlled by an external controller that can control the four quadrant power flow through the GTI, while the controller also digitally switches an auxiliary relay to switch in a three phase Resistor-Inductor-Capacitor (RLC) circuit to initiate three phase power oscillations in the circuit. Three phase voltage and current measurements (sensors) are processed by the controller to compute real-time power oscillation in the circuit. The Grid Tied Inverter (GTI) is a GTI3100A6208/3652IR-PQ manufactured by One-Cycle Control Incorporation. It is a four-quadrant inverter, which is capable to accept external control signals for implementation of feedback control to control or damped power oscillations. Additional EMI filters FN2200B are placed between the DC source and the inverter to eliminate the effect of common AC mode currents due to the high frequency Pulse Width Modulation (PWM) of the GTI. The output of the inverter is connected to the grid through a three-phase switch and a circuit breaker to limit the current for protection.

A three-phase RLC load circuit is designed and integrated into the testbed to

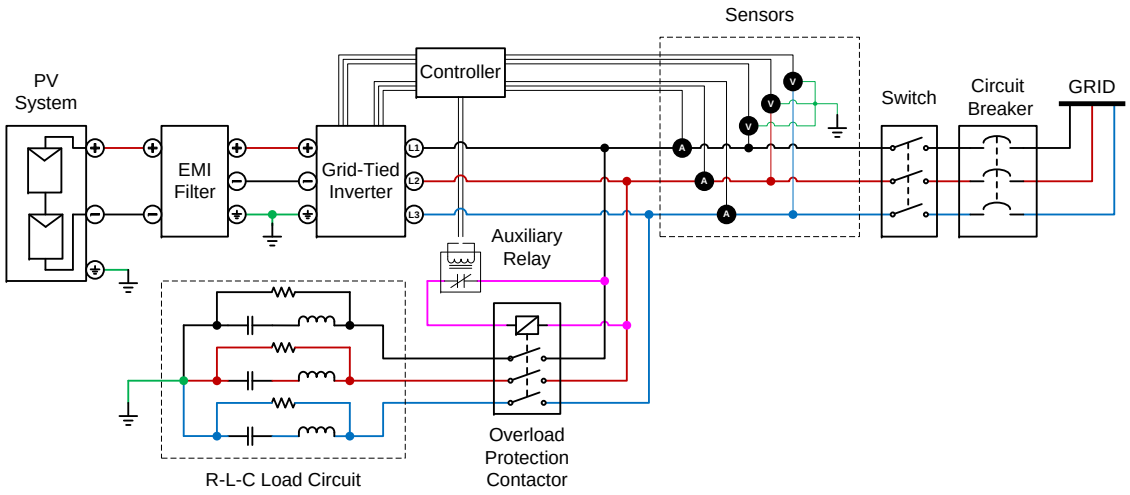

Figure 5.2: Diagram of experimental setup.

act as a real power disturbance. As depicted in Fig. 5.2, each phase is composed by a bypass resistor of 100Ω that is in parallel with a series connection of a capacitor of 0.01F and an inductor of 0.1H. The Inductor-Capacitor (LC) circuit is to generate a resonance; the bypass resistor is to consume real power and also discharge the LC circuit while it is not energized. The circuit is connected to the output of the grid-tied inverter through an overload protection relay.

A controller with National Instruments (NI) myRIO is integrated into the testbed for data acquisition and controlling the grid-tied inverter. The three-phase AC voltage and current signal of grid-tied inverter is measured, conditioned, and sent into the controller. The controller can also send out control signals via signal conditioning circuit to drive the grid-tied inverter and moreover, to switch in the load circuit to the system by energizing the overload protection contactor via an auxiliary relay.

The description of the testbed is completed by a photo as shown in Fig. 5.10. The parts are aligned and mounted in a cabinet for safety consideration. In the RLC

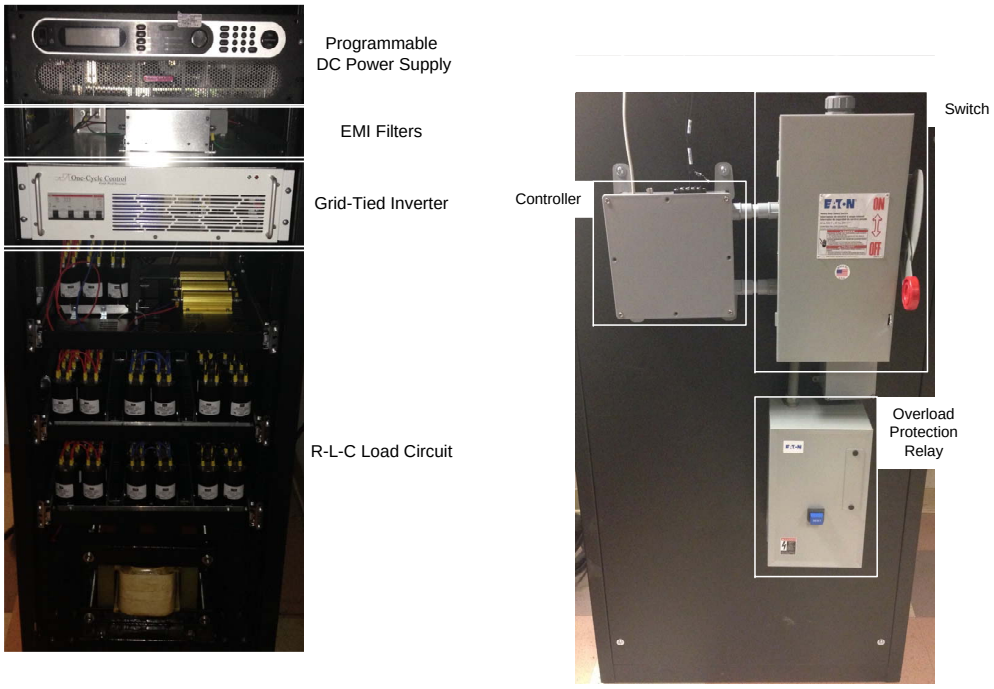

(a) (b)

Figure 5.3: Front and side of the testbed housing the components for real-time analysis and identification of real power oscillations.

load circuit, an array of AC capacitors is formed as a capacitive load.

The control diagram of the testbed is depicted in Fig. 5.4. The model G represents the grid-tied inverter, while H is the dynamic model of the RLC load circuit. The objective is to design a controller C which can mitigate fluctuations observed in $p(t)$.

5.3 Characterizing System Dynamics

5.3.1 Disturbance Dynamics

A key assumption that could be made when a power oscillation occurs is to assume that the power oscillation is due to a step-wise change in load demand.

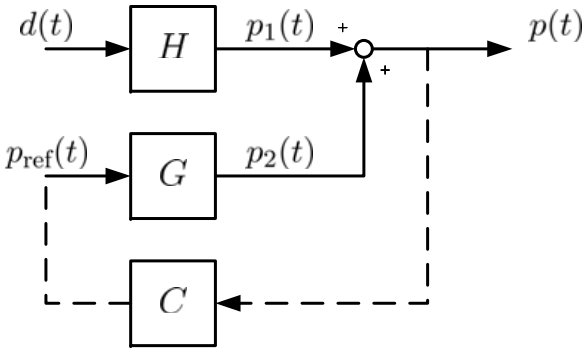

Figure 5.4: Schematic diagram of feedback control configuration implemented in the testbed for disturbance rejection control.

The size of the load demand may not be known, but the *a priori* knowledge of the step-wise load demand can be exploited to formulate a low order state space model to model the dynamics of any observed power oscillations. In particular, the low order state space model can be realized on the basis of a real-time measurements of three phase real power oscillations to accurately model frequency and damping of the power oscillations. Although the approach is similar to the modal analysis approach in [77], the proposed realization method in this paper allows the low order models to be formulated directly on the basis of real-time measurements of power oscillations. More details on the step-based realization algorithms in included below.

The Step-Based Realization Algorithm

Let $\{y(0), y(1), ..., y(N)\}$ be a measured response of an LTI, single-input-multi-output (SIMO) system to a unit-step input applied at $t = 0$ that is corrupted by some possibly-colored measurement noise $v(t)$. To estimate a state space model of the system

$$x(t+1) = Ax(t) + Bu(t) \tag{5.1}$$

$$y(t) = Cx(t) + Du(t) + v(t), \tag{5.2}$$

one may follow the following steps:

- Step I

  Construct the block-Hankel data matrices

$$Y = \begin{bmatrix} y(1) & y(2) & \cdots & y(l) \\ y(2) & y(3) & \cdots & y(l+1) \\ \vdots & \vdots & & \vdots \\ y(r) & y(r+1) & \cdots & y(N-1) \end{bmatrix}$$

$$\bar{Y} = \begin{bmatrix} y(2) & y(3) & \cdots & y(l+1) \\ y(3) & y(4) & \cdots & y(l+2) \\ \vdots & \vdots & & \vdots \\ y(r+1) & y(r+2) & \cdots & y(N) \end{bmatrix},$$

  and matrices

$$M = \begin{bmatrix} y(0) & y(0) & \cdots \\ y(1) & y(1) & \cdots \\ \vdots & \vdots & \\ y(r-1) & y(r-1) & \cdots \end{bmatrix}, \; \bar{M} = \begin{bmatrix} y(1) & y(1) & \cdots \\ y(2) & y(2) & \cdots \\ \vdots & \vdots & \\ y(r) & y(r) & \cdots \end{bmatrix}.$$

- Step II

  Construct matrices

$$\begin{aligned} R &= Y - M \\ \bar{R} &= \bar{Y} - \bar{M} \end{aligned}$$

then take the singular value decomposition (SVD) of the matrix R:

$$R = \begin{bmatrix} U_n & U_s \end{bmatrix} \begin{bmatrix} \Sigma_n & 0 \\ 0 & \Sigma_s \end{bmatrix} \begin{bmatrix} V_n & V_s \end{bmatrix} \tag{5.3}$$

An appropriate system order n may be found from the range of the singular values in (5.3).

- Step III

  Estimate A as

  $$\hat{A} = \Sigma_n^{-1/2} U_n^T \bar{R} V_n \Sigma_n^{-1/2}.$$

  C is estimated as

  $$\hat{C} = (U_n \Sigma_n^{1/2})_{(1:n_y,:)}.$$

  A possible estimate for B is

  $$\hat{B} = (\Sigma_n^{1/2} V_n^T)_{(:,1)},$$

  then D is estimated as

  $$\hat{D} = y(0).$$

  Improved estimates of B and D may also be found via a least-squares mini-

mization. Given estimates $\hat{A}$ and $\hat{C}$, let $\hat{B}$ and $\hat{D}$ be the solution of

$$\hat{B}, \hat{D} = \arg\min ||y - \hat{y}||_2$$

$$y = \begin{bmatrix} y(0) \\ y(1) \\ \vdots \\ y(N+i) \end{bmatrix}, \ \hat{y} = \begin{bmatrix} \hat{y}(0) \\ \hat{y}(1) \\ \vdots \\ \hat{y}(N+i) \end{bmatrix} \text{ where}$$

$$\hat{y}(t) = \left[\sum_{k=0}^{t-1} \hat{C}\hat{A}^{t-k-1}\mathbf{1} \right] \hat{\theta}, \ \hat{\theta} = \begin{bmatrix} \hat{B} \\ \hat{D} \end{bmatrix}$$

One is referred to [85] for additional details on the step realization method.

Identification of Disturbance Model

In the experimental verification of the real-time real power demodulation and application of the step-based realization algorithm, power oscillations are induced by step-wise excitation of the auxiliary relay depicted earlier in Fig. 5.2 to switch in a three phase Resistor-Inductor-Capacitor (RLC) circuit to initiate three phase power oscillations in the circuit. The input $u(t)$ is used to denote the digital signal sent to the auxiliary relay; the output $y(t)$ is the real-time demodulated real power calculated by the method described in Section 2.3.

In Fig. 5.5, $u(t)$ stepped from 0 to 1 at $t = 0$, the upper plot shows the demodulated real power of each phase; the bottom plot shows the demodulated three-phase real power.

The step-based realization algorithm is applied to verify the proposed method of real power demodulation. The RLC circuit depicted in Fig. 5.2 is a second-order

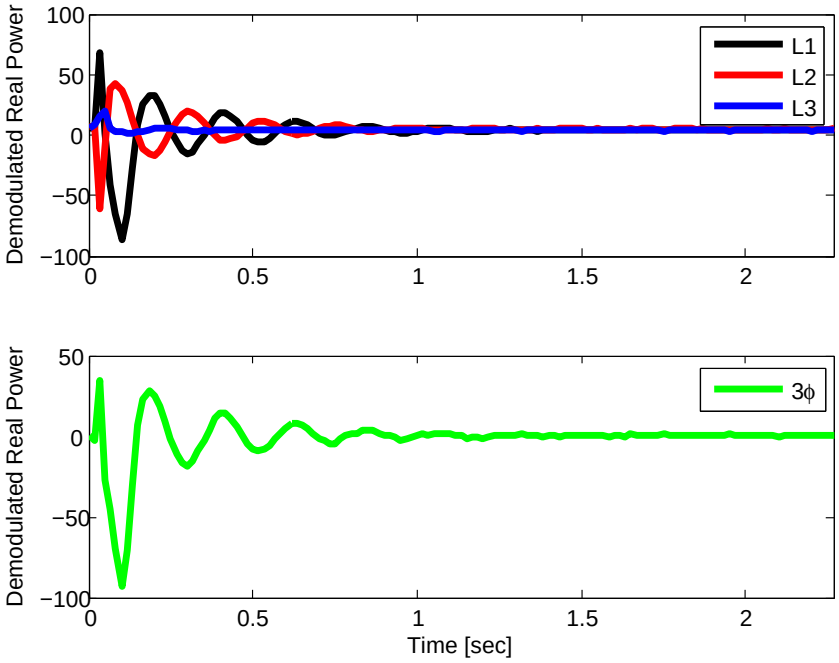

Figure 5.5: Demodulated real power signal oscillations in each phase (top figure) and three phase (bottom figure) of the RLC circuit induced by a step-wise load change.

system. With $L = 0.1\text{H}$, $C = 0.01\text{F}$, we know that the (undamped) oscillation frequency of such an RLC circuit is given by

$$f = \frac{1}{2\pi\sqrt{LC}} = 5.03\text{Hz} \tag{5.4}$$

In practice, the contactor cannot be fully energized rapidly, thus it results in additional dynamics in the system. This can be observed by the irregular oscillation from $t = 0$ to $t = 0.15\text{s}$ in Fig. 5.5. To further verify this, the segment starting from $t = 0.15\text{s}$ is selected to estimate a model. With a second-order state space model, the step response of the RLC circuit can be reconstructed. By comparison with the raw demodulated real power as shown in Fig. 5.6a, it is verified that the model captures very well the dynamics of the 3 phase RLC system. It also validates the proposed

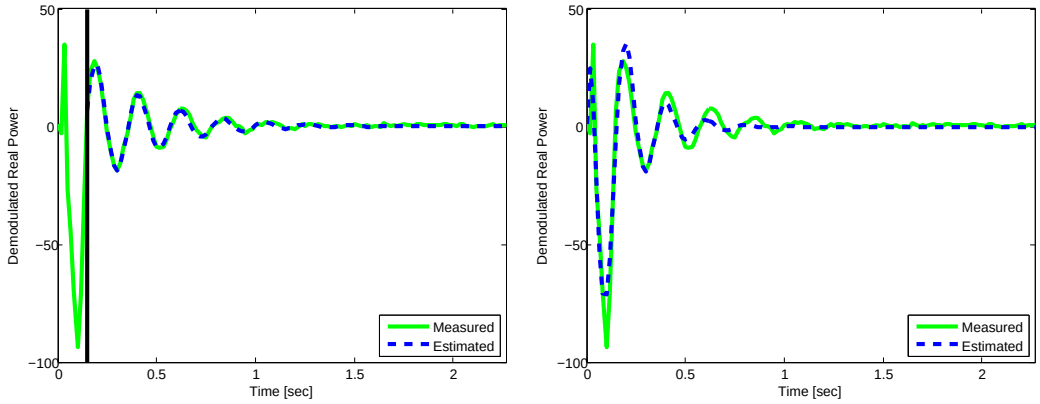

Figure 5.6: Comparison between measured and modeled/estimated real power oscillations.

method of real-time demodulation of real power oscillation.

If the contactor dynamics is taken into account, a higher-order model can be used to capture this dynamics. As shown in Fig. 5.6b, a third-order state space model is realized. The dynamics of the three phase RLC system including the contactor are both captured by the model.

Thus, the disturbance model H in the control diagram shown in Fig. 5.4 is obtained.

5.3.2 Actuator Dynamics

The actuator of the feedback control in the system, which is the GTI, also can be modeled from a step input response. In particular, an output-error (OE) model is applied to characterize the GTI's output. The obtained model G is shown as in Fig. 5.7 compared with the actual step response.

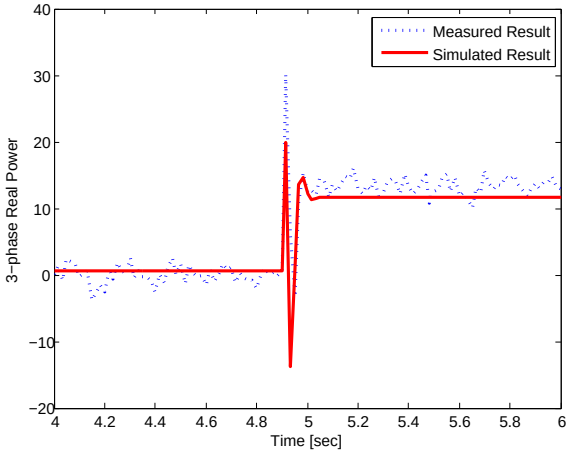

Figure 5.7: Comparison between measured and modeled GTI output.

5.4 Controller Design

Multiple controller design approaches can be applied to obtain a proper disturbance rejection for the system. In this section, an approach combining the internal model principle [86] and H_2 optimal control [87, 88, 89] is introduced. The objective of such approach is to obtain a controller that can not only reject known disturbances but also balance the trade-off between minimizing the output fluctuation caused by disturbance and required energy of control input. The diagram for controller design is shown as in Fig. 5.8.

First, the system P is formulated into the transfer function matrix form

$$\begin{bmatrix} z_1 \\ z_2 \\ p \end{bmatrix} = \begin{bmatrix} H & G \cdot H \cdot F \\ 0 & \gamma H \cdot F \\ H & G \cdot H \cdot F \end{bmatrix} \begin{bmatrix} d \\ u \end{bmatrix} \tag{5.5}$$

Through proper realization and pole-zero cancellation, the plant described by

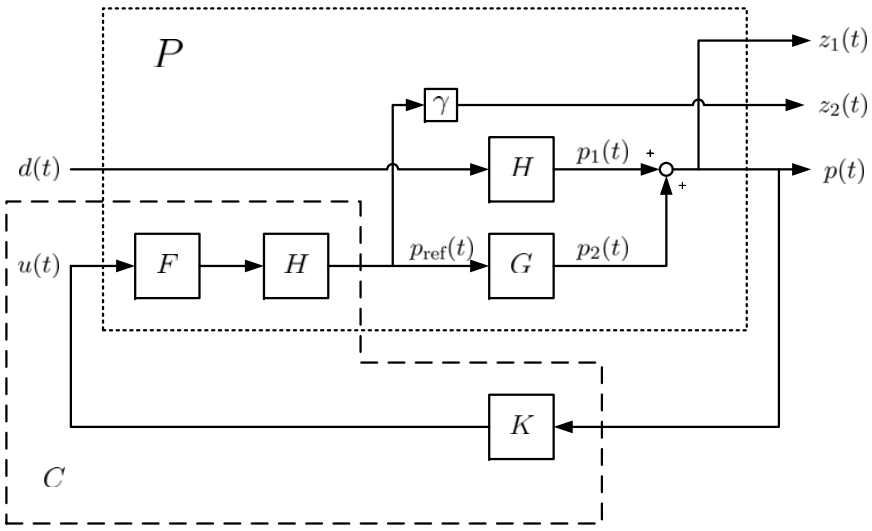

Figure 5.8: Diagram of the system configured for optimal controller design.

(5.5) can be converted to a standard state-space form

$$\begin{aligned} \dot{x} &= Ax + B_1 d + B_2 u \\ z &= C_1 x + D_{11} d + D_{12} u \\ p &= C_2 x + D_{21} d + D_{22} u \end{aligned} \tag{5.6}$$

where $z = \begin{bmatrix} z_1 & z_2 \end{bmatrix}^T$. The Bode plot of P is shown as in Fig. 5.9.

Then the controller K can be obtained through finding a stabilizing positivie-feedback controller for the above system such that the H_2-norm of the closed-loop transfer function matrix $T_{z,d}$ is minimized [87, 88, 89]:

$$\min_K ||T_{z,d}||_2 = \min_K \left(\frac{1}{\pi} \int_0^\infty \text{trace}(T_{z,d}^*(j\omega) T_{z,d}(j\omega)) d\omega \right) \tag{5.7}$$

Finally, the feedback controller C in Fig. 5.4 can be obtained by

$$C = -K \cdot H \tag{5.8}$$

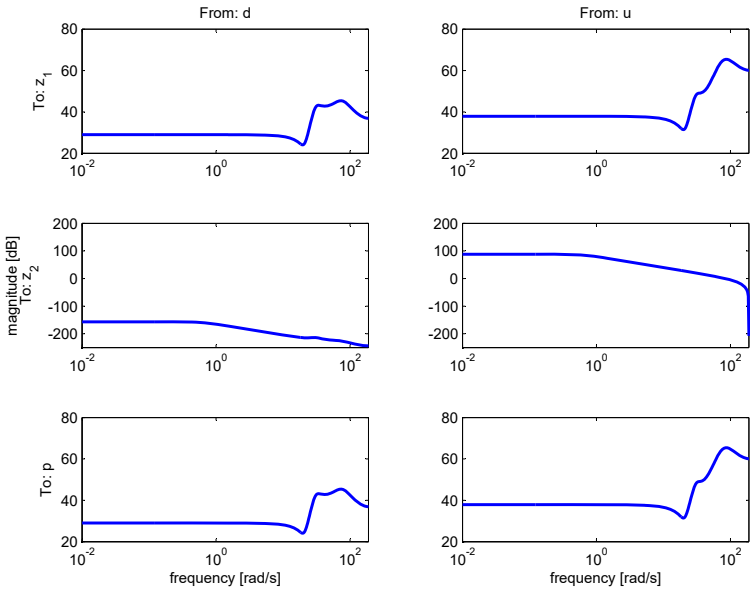

Figure 5.9: Bode plot of the Two-Input Three-Output plant P.

The frequency response of C is further verified as shown in Fig. 5.10a. And the frequency response of the open-loop sensitivity H and the closed-loop sensitivity $H/(1+GC)$ is given in Fig. 5.10b. From Fig. 5.10b, it can be observed that the mitigation is achieved in the frequency range of 25–36 rad/s, i.e. approximately 4–5.7Hz.

The performance of the designed controller is as shown in Fig. 5.11. The step response of the closed-loop system is mitigated by comparing with the open-loop system's response.

5.5 Experimental Results and Analysis

Experiments on implementing closed-loop controller in the system have been conducted. A set of experimental results are shown in Fig. 5.12 by comparing system output without feedback control (blue line) and with feedback control (green line).

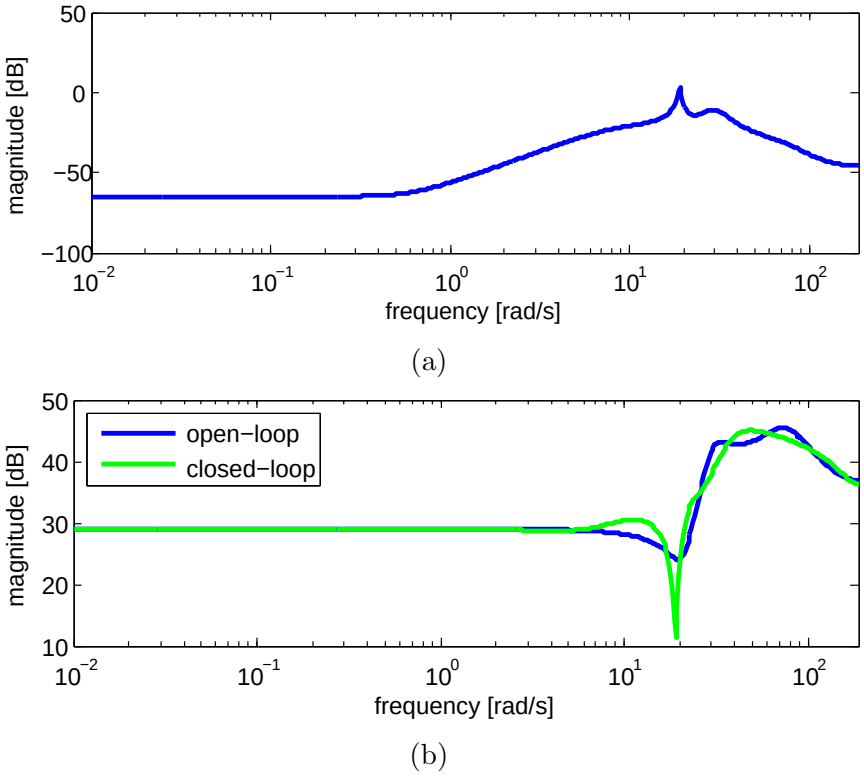

Figure 5.10: Frequency response of (a) controller C; (b) open-loop sensitivity and closed-loop sensitivity.

The experimental result matches the simulated results given in Fig. 5.11. It can be observed from Fig. 5.12 that the oscillation due to the switching of the inductive load, normally results in a oscillation of around 5Hz that persists for several oscillation periods. With damping control that only uses information of measurements of real power in a feedback configuration reduces the oscillations down to only a single or perhaps 2 periods. These results indicate that disturbance is rejected by about 15 %.

One remark must be given to the results depicted in Fig. 5.12. The real power measurements are more noisy when the OCC-GTI is used to modulate real power. The noisy behavior of the real power measurements are due to the high frequency switching of the 42kW OCC-GTI that is only used over a very small range to mitigate real power oscillations. Such noise is anticipated to become negligible

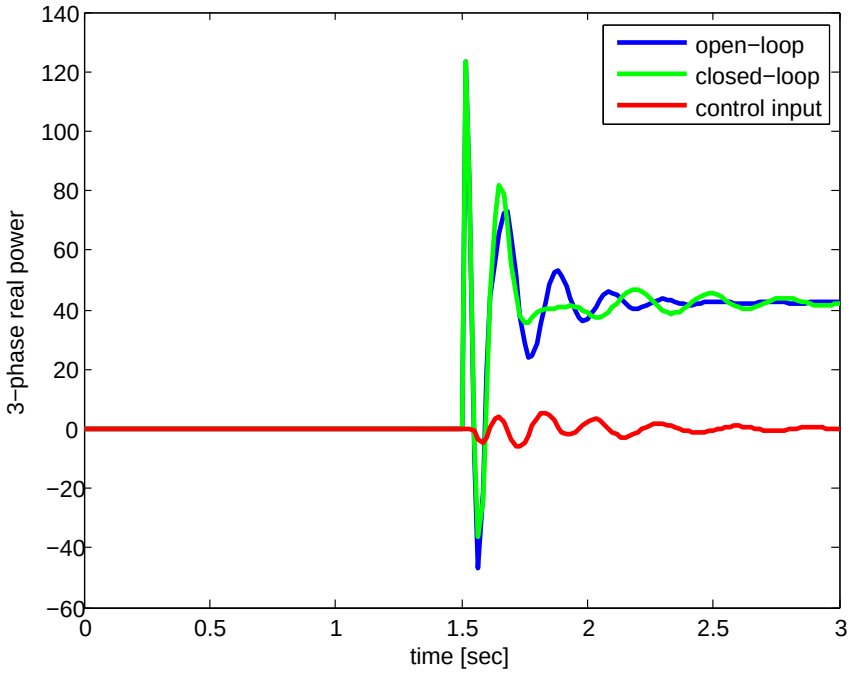

Figure 5.11: Comparison between simulated open-loop and closed-loop responses to verify the control performance.

when the disturbance rejection control is performed on a larger scale where (multiple) OCC-GTIs can be modulated for control over the full 42kW range.

5.6 Acknowledgment

Chapter 5, in part, is based on the material that appears in Proceedings of IFAC Symposium on System Identification (SYSID) 2015, Pages 63–68. Zhao, Xin; van de Ven, Maurice L. J.; de Callafon, Raymond A.; Torre, William. "Real-Time Demodulation of Real Power Oscillations." The dissertation author was the primary author of this paper.

Chapter 5, in part, is based on the material that is currently being prepared for submission for publication. Zhao, Xin; Gwynn, Benjamin T.; de Callafon, Raymond A.; Torre, William. "Power Flow Disturbance Rejection Control on Micro-Grid." The

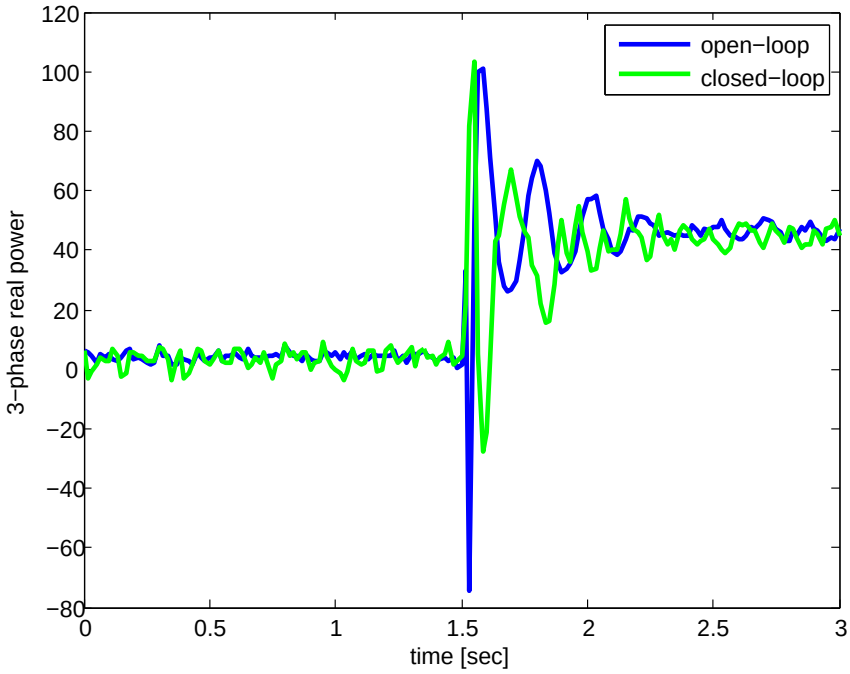

Figure 5.12: Comparison between experimental open-loop and closed-loop system output subject to a disturbance.

dissertation author is the primary author of this paper.

Chapter 6

Conclusions and Future Work

In order to meet emerging requirements for better utilization of electrical energy, systematic research on applying advanced modeling and control technology to Electrical Energy Storage and Delivery System (EESDS) is required. In this dissertation, three main problems are studied: a) modeling of a battery system; b) scheduling of parallel-connected battery systems; c) mitigation of AC power flow fluctuations by controllable inverter. The summary for completed and future work is as follows.

- **Battery Modeling for Power Delivery Dynamics Prediction and SOC Estimation:** A battery modeling approach is proposed to characterize power delivery dynamics, given charge and discharge demand as an input, and also to estimate the state-of-charge of a battery, not only in normal operating range, but also in extreme cases, such as battery over-charging. This is a control-oriented modeling approach which is different from the conventional equivalent circuit models and electrochemical models. In particular, the model is composed of separated voltage and current models. Several non-linear models, including Hammerstein model, open-circuit voltage characteristics, and Takacs hysteresis

model are combined in the voltage and the current model, respectively. The state-of-charge of the battery is estimated in a recursive optimization fashion. The parameterization and estimation methods of the model are described and also validated on experimental data from a lithium iron phosphate cell. By utilizing the proposed model, the energy delivery capability and available energy of a single battery system can be understood.

For future research, the proposed modeling approach is expected to be first validated on experimental data from a larger-scale battery system, such as a battery bank connected to electric grid. The parameterization and estimation of the components in the formulated model framework needs to be further improved. For instance, the static non-linearities included in Hammerstein models can stem from the circuitry executing charge and discharge, therefore more advanced identification methods need to be applied for the estimation.

- **Current Scheduling for Parallel-Connected Modular Batteries:** Three current scheduling strategies are proposed to coordinate the output of each battery system in a parallel-connected network which is usually for expanding the total capacity. Besides simultaneous and sequential discharge scheduling algorithms, a hybrid algorithm is formulated by solving a Quadratic Programming problem. The simulation results indicate the feasibility of the proposed scheduling algorithms and motivate the use of parallel connected battery modules despite changes in battery operating parameters. The simultaneous and sequential discharge scheduling algorithms are then extended to power scheduling.

  A complete modular battery system for Electric Vehicle with the same topol-

ogy is developed for experimental validation. Each battery module integrates a Battery Management System (BMS) for real-time monitoring and charge balancing, and a buck regulator for controlling the power output. To execute real-time feedback control, a 2.4GHz wireless star network is integrated in the system with a base station collecting real-time information from each battery module and coordinating the output of each module.

In the future, power scheduling for parallel-connected battery systems, instead of only current scheduling, needs to be addressed to optimize energy transformation. The HybD scheduling needs to be re-formulated and solved by a different programming algorithm in order to be applied for power scheduling. Moreover, the feasibility and performance of executing the proposed scheduling algorithms in practice depends on proper control of the actuator, which is done by the PWM signal applied to MOSFETs in buck regulation circuits of each module. As a typical control design cycle, first the possibility of an open-loop control law needs to be addressed, then a closed-loop control should be considered if either the open-loop control is unfeasible or the control performance needs to be improved. Since the actuators in such system are distributed, some issues such as synchronization in the controller design of a distributed control system should be also addressed. In order to achieve that, the WDTSR tests introduced is one of the bench tests that need to be extensively conducted for improving the wireless communication performance of the system. The improvement is expected to be achieved by up-to-date wireless communication platforms.

- **Disturbance Rejection Control for Mitigation of AC Power Flow Fluc-**

tuations: A disturbance rejection control law is designed to mitigate the fluctuation of AC power flow in order to maintain the stability of the entire grid. An experimental setup integrating grid-tied inverter (GTI), a three-phase Resistor-Inductor-Capacitor (RLC) network, sensors and embedded controller is created. Based on that, a complete control design process is done by demodulating real power oscillations, modeling of actuator and disturbance, and controller design by combining the internal model principle and H_2 control.

In practice, different control objectives may be proposed for maintaining the stability of an electric grid. But the design process demonstrated in this dissertation provides some references for future research. The created experimental setup can be the fundamental for future research on implementation of advanced control for power flow. The achieved experiences in the small-scale experiments are then expected to be applied for a larger-scale system, such as a micro-grid, in the future.

Bibliography

[1] S. Øvergaard, "Issue paper: Definition of primary and secondary energy," *Statistics Norway, Oslo*, 2008.

[2] M. Faraday, *Experimental researches in electricity.* Bernard Quaritch, 1855, vol. 3.

[3] S.-K. Kim, J.-H. Jeon, C.-H. Cho, J.-B. Ahn, and S.-H. Kwon, "Dynamic modeling and control of a grid-connected hybrid generation system with versatile power transfer," *IEEE Transactions on Industrial Electronics*, vol. 55, no. 4, pp. 1677–1688, Apr. 2008.

[4] H. Karimi, H. Nikkhajoei, and R. Iravani, "Control of an electronically-coupled distributed resource unit subsequent to an islanding event," *IEEE Transactions on Power Delivery*, vol. 23, no. 1, pp. 493–501, Jan. 2008.

[5] I. Husain, *Electric and Hybrid Vehicles: Design Fundamentals, Second Edition.* CRC Press, Jun. 2011.

[6] I. Aharon and A. Kuperman, "Topological overview of powertrains for battery-powered vehicles with range extenders," *IEEE Transactions on Power Electronics*, vol. 26, no. 3, pp. 868–876, Mar. 2011.

[7] M. Armand and J.-M. Tarascon, "Building better batteries," *Nature*, vol. 451, no. 7179, pp. 652–657, Feb. 2008.

[8] B. Kang and G. Ceder, "Battery materials for ultrafast charging and discharging," *Nature*, vol. 458, no. 7235, pp. 190–193, Mar. 2009.

[9] B. Dunn, H. Kamath, and J.-M. Tarascon, "Electrical energy storage for the grid: A battery of choices," *Science*, vol. 334, no. 6058, pp. 928–935, Nov. 2011.

[10] B. K. Bose, *Modern Power Electronics and AC Drives*, 1st ed. Upper Saddle River, NJ: Prentice Hall, Oct. 2001.

[11] J. Carrasco, L. Franquelo, J. Bialasiewicz, E. Galvan, R. Guisado, M. Prats, J. Leon, and N. Moreno-Alfonso, "Power-electronic systems for the grid integration of renewable energy sources: A survey," *IEEE Transactions on Industrial Electronics*, vol. 53, no. 4, pp. 1002–1016, Jun. 2006.

[12] A. S. Dobakhshari, S. Azizi, and A. M. Ranjbar, "Control of microgrids: Aspects and prospects," in *2011 IEEE International Conference on Networking, Sensing and Control (ICNSC)*, Apr. 2011, pp. 38–43.

[13] H. Kanchev, D. Lu, F. Colas, V. Lazarov, and B. Francois, "Energy management and operational planning of a microgrid with a PV-based active generator for smart grid applications," *IEEE Transactions on Industrial Electronics*, vol. 58, no. 10, pp. 4583–4592, Oct. 2011.

[14] A. E. Emanuel, *Power Definitions and the Physical Mechanism of Power Flow*. John Wiley & Sons, 2011, vol. 22.

[15] "IEEE Standard Definitions for the Measurement of Electric Power Quantities Under Sinusoidal, Nonsinusoidal, Balanced, or Unbalanced Conditions," *IEEE Std 1459-2010 (Revision of IEEE Std 1459-2000)*, pp. 1–50, Mar. 2010.

[16] A. G. Phadke and J. S. Thorp, *Synchronized Phasor Measurements and Their Applications*. Springer Science & Business Media, 2008.

[17] H. Akagi, Y. Kanazawa, and A. Nabae, "Principles and compensation effectiveness of instantaneous reactive power compensator devices," in *Meeting of the power semiconductor converters researchers-IEE-Japan, SPC-82-16*, 1982.

[18] H. Akagi, E. H. Watanabe, and M. Aredes, *Instantaneous Power Theory and Applications to Power Conditioning*. John Wiley & Sons, 2007, vol. 31.

[19] L. S. Czarnecki, "Instantaneous reactive power p-q theory and power properties of three-phase systems," *IEEE Transactions on Power Delivery*, vol. 21, no. 1, pp. 362–367, Jan. 2006.

[20] M. Lave, J. Kleissl, and J. S. Stein, "A wavelet-based variability model (WVM) for solar PV power plants," *IEEE Transactions on Sustainable Energy*, vol. 4, no. 2, pp. 501–509, Apr. 2013.

[21] H. Zhou, T. Bhattacharya, D. Tran, T. S. T. Siew, and A. M. Khambadkone, "Composite energy storage system involving battery and ultracapacitor with dynamic energy management in microgrid applications," *IEEE Transactions on Power Electronics*, vol. 26, no. 3, pp. 923–930, Mar. 2011.

[22] F. Sun, R. Xiong, H. He, W. Li, and J. E. E. Aussems, "Model-based dynamic multi-parameter method for peak power estimation of lithium–ion batteries," *Applied Energy*, vol. 96, pp. 378–386, Aug. 2012.

[23] L. Lu, X. Han, J. Li, J. Hua, and M. Ouyang, "A review on the key issues for lithium-ion battery management in electric vehicles," *Journal of Power Sources*, vol. 226, pp. 272–288, Mar. 2013.

[24] B. G. Kim, S. Ren, M. van der Schaar, and J. W. Lee, "Bidirectional energy trading and residential load scheduling with electric vehicles in the smart grid," *IEEE Journal on Selected Areas in Communications*, vol. 31, no. 7, pp. 1219–1234, Jul. 2013.

[25] A. V. Savkin, M. Khalid, and V. G. Agelidis, "Optimal size of battery energy storage and monotonic charging/discharging strategies for wind farms," in *2014 IEEE Conference on Control Applications (CCA)*, Oct. 2014, pp. 1372–1376.

[26] Y. Lin, P. Barooah, and J. L. Mathieu, "Ancillary services to the grid from commercial buildings through demand scheduling and control," in *2015 American Control Conference (ACC)*, Jul. 2015, pp. 3007–3012.

[27] M. Doyle, T. F. Fuller, and J. Newman, "Modeling of galvanostatic charge and discharge of the lithium/polymer/insertion cell," *Journal of The Electrochemical Society*, vol. 140, no. 6, pp. 1526–1533, Jun. 1993.

[28] T. F. Fuller, M. Doyle, and J. Newman, "Simulation and optimization of the dual lithium ion insertion cell," *Journal of The Electrochemical Society*, vol. 141, no. 1, pp. 1–10, Jan. 1994.

[29] J. C. Forman, S. J. Moura, J. L. Stein, and H. K. Fathy, "Genetic identification and fisher identifiability analysis of the Doyle–Fuller–Newman model from experimental cycling of a LiFePO4 cell," *Journal of Power Sources*, vol. 210, pp. 263–275, Jul. 2012.

[30] N. Chaturvedi, R. Klein, J. Christensen, J. Ahmed, and A. Kojic, "Algorithms for advanced battery-management systems," *IEEE Control Systems*, vol. 30, no. 3, pp. 49–68, Jun. 2010.

[31] S. J. Moura, N. A. Chaturvedi, and M. Krstić, "Adaptive partial differential equation observer for battery state-of-charge/state-of-health estimation via an electrochemical model," *Journal of Dynamic Systems, Measurement, and Control*, vol. 136, no. 1, p. 011015, 2014.

[32] W. Waag, C. Fleischer, and D. U. Sauer, "Critical review of the methods for monitoring of lithium-ion batteries in electric and hybrid vehicles," *Journal of Power Sources*, vol. 258, pp. 321–339, Jul. 2014.

[33] X. Hu, S. Li, and H. Peng, "A comparative study of equivalent circuit models for Li-ion batteries," *Journal of Power Sources*, vol. 198, pp. 359–367, 2012.

[34] Z. Wei, T. M. Lim, M. Skyllas-Kazacos, N. Wai, and K. J. Tseng, "Online state of charge and model parameter co-estimation based on a novel multi-timescale estimator for vanadium redox flow battery," *Applied Energy*, vol. 172, pp. 169–179, Jun. 2016.

[35] Z. Chen, B. Xia, C. C. Mi, and R. Xiong, "Loss-minimization-based charging strategy for lithium-ion battery," *Industry Applications, IEEE Transactions on*, vol. 51, no. 5, pp. 4121–4129, 2015.

[36] J. Lee, O. Nam, and B. H. Cho, "Li-ion battery SOC estimation method based on the reduced order extended Kalman filtering," *Journal of Power Sources*, vol. 174, no. 1, pp. 9–15, Nov. 2007.

[37] Y. Zou, S. E. Li, B. Shao, and B. Wang, "State-space model with non-integer order derivatives for lithium-ion battery," *Applied Energy*, vol. 161, pp. 330–336, Jan. 2016.

[38] Y. Jiang, X. Zhao, A. Valibeygi, and R. A. de Callafon, "Dynamic prediction of power storage and delivery by data-based fractional differential models of a lithium iron phosphate battery," *Energies*, vol. 9, no. 8, p. 590, Jul. 2016.

[39] O. Tremblay and L.-A. Dessaint, "Experimental validation of a battery dynamic model for EV applications," *World Electric Vehicle Journal*, vol. 3, no. 1, pp. 1–10, 2009.

[40] R. Xiong, F. Sun, Z. Chen, and H. He, "A data-driven multi-scale extended Kalman filtering based parameter and state estimation approach of lithium-ion olymer battery in electric vehicles," *Applied Energy*, vol. 113, pp. 463–476, Jan. 2014.

[41] M. W. Verbrugge and P. Liu, "Electrochemical characterization of high-power lithium ion batteries using triangular voltage and current excitation sources," *Journal of Power Sources*, vol. 174, no. 1, pp. 2–8, Nov. 2007.

[42] F. Yang, Y. Xing, D. Wang, and K.-L. Tsui, "A comparative study of three model-based algorithms for estimating state-of-charge of lithium-ion batteries under a new combined dynamic loading profile," *Applied Energy*, vol. 164, pp. 387–399, Feb. 2016.

[43] H. Fang, X. Zhao, Y. Wang, Z. Sahinoglu, T. Wada, S. Hara, and R. A. de Callafon, "Improved adaptive state-of-charge estimation for batteries using a multi-model approach," *Journal of Power Sources*, vol. 254, pp. 258–267, May 2014.

[44] C. Lin, H. Mu, R. Xiong, and W. Shen, "A novel multi-model probability battery state of charge estimation approach for electric vehicles using H-infinity algorithm," *Applied Energy*, vol. 166, pp. 76–83, Mar. 2016.

[45] M. A. Roscher, O. Bohlen, and J. Vetter, "OCV hysteresis in Li-ion batteries including two-phase transition materials," *International Journal of Electrochemistry*, vol. 2011, p. e984320, May 2011.

[46] A. Marongiu, F. G. W. Nußbaum, W. Waag, M. Garmendia, and D. U. Sauer, "Comprehensive study of the influence of aging on the hysteresis behavior of a lithium iron phosphate cathode-based lithium ion battery – An experimental investigation of the hysteresis," *Applied Energy*, vol. 171, pp. 629–645, Jun. 2016.

[47] H. Zhang and M.-Y. Chow, "On-line PHEV battery hysteresis effect dynamics modeling," in *IECON 2010 - 36th Annual Conference on IEEE Industrial Electronics Society*, Nov. 2010, pp. 1844–1849.

[48] T. Kim, W. Qiao, and L. Qu, "Hysteresis modeling for model-based condition monitoring of lithium-ion batteries," in *2015 IEEE Energy Conversion Congress and Exposition (ECCE)*, Sep. 2015, pp. 5068–5073.

[49] X. Tang, X. Zhang, B. Koch, and D. Frisch, "Modeling and estimation of Nickel Metal Hydride battery hysteresis for SOC estimation," in *International Conference on Prognostics and Health Management, 2008. PHM 2008*, Oct. 2008, pp. 1–12.

[50] L. Zhu, Z. Sun, H. Dai, and X. Wei, "A novel modeling methodology of open circuit voltage hysteresis for $LiFePO_4$ batteries based on an adaptive discrete Preisach model," *Applied Energy*, vol. 155, pp. 91–109, Oct. 2015.

[51] J. Takacs, *Mathematics of Hysteretic Phenomena: The T(x) Model for the Description of Hysteresis*, Sep. 2003.

[52] K. Chwastek, "Modelling hysteresis loops in thick steel sheet with the dynamic Takács model," *Physica B: Condensed Matter*, vol. 407, no. 17, pp. 3632–3634, Sep. 2012.

[53] D. Herceg, D. Herceg, and M. Prša, "Using Padé approximation in Takács hysteresis model," *IEEE Transactions on Magnetics*, vol. 51, no. 7, pp. 1–4, Jul. 2015.

[54] N. Windarko and J. Choi, "Hysteresis modeling for estimation of State-of-Charge in NiMH battery based on improved Takacs model," in *Telecommunications Energy Conference, 2009. INTELEC 2009. 31st International*, Oct. 2009, pp. 1–6.

[55] L. Ljung, *System Identification: Theory for the User*, 2nd ed. Upper Saddle River, NJ: Prentice Hall, Jan. 1999.

[56] A. Wills, T. B. Schön, L. Ljung, and B. Ninness, "Identification of Hammerstein–Wiener models," *Automatica*, vol. 49, no. 1, pp. 70–81, Jan. 2013.

[57] T. Söderström and P. G. Stoica, *Instrumental Variable Methods for System Identification*, 1st ed. Berlin; New York: Springer, 1983.

[58] M. Bragard, N. Soltau, S. Thomas, and R. W. D. Doncker, "The balance of renewable sources and user demands in grids: Power electronics for modular battery energy storage systems," *IEEE Transactions on Power Electronics*, vol. 25, no. 12, pp. 3049–3056, Dec. 2010.

[59] K. Smith and C.-Y. Wang, "Power and thermal characterization of a lithium-ion battery pack for hybrid-electric vehicles," *Journal of Power Sources*, vol. 160, no. 1, pp. 662–673, Sep. 2006.

[60] G. Lacey, G. Putrus, and A. Salim, "The use of second life electric vehicle batteries for grid support," in *2013 IEEE EUROCON*, Jul. 2013, pp. 1255–1261.

[61] A. Khaligh and Z. Li, "Battery, ultracapacitor, fuel cell, and hybrid energy storage systems for electric, hybrid electric, fuel cell, and plug-in hybrid electric vehicles: State of the art," *IEEE Transactions on Vehicular Technology*, vol. 59, no. 6, pp. 2806–2814, Jul. 2010.

[62] C. Botsford and A. Szczepanek, "Fast charging vs. slow charging: Pros and cons for the new age of electric vehicles," in *International Battery Hybrid Fuel Cell Electric Vehicle Symposium*, 2009.

[63] Y. Nishi, "Lithium ion secondary batteries; Past 10 years and the future," *Journal of Power Sources*, vol. 100, no. 1–2, pp. 101–106, Nov. 2001.

[64] S. Mehrotra, "On the implementation of a primal-dual interior point method," *SIAM Journal on Optimization*, vol. 2, no. 4, pp. 575–601, Nov. 1992.

[65] P. M. Pardalos and M. G. Resende, *Handbook of Applied Optimization*. Oxford university press, 2001.

[66] X. Bai, H. Wei, K. Fujisawa, and Y. Wang, "Semidefinite programming for optimal power flow problems," *International Journal of Electrical Power & Energy Systems*, vol. 30, no. 6–7, pp. 383–392, Jul. 2008.

[67] R. Kaiser, "Optimized battery-management system to improve storage lifetime in renewable energy systems," *Journal of Power Sources*, vol. 168, no. 1, pp. 58–65, May 2007.

[68] L. Gao, S. Liu, and R. Dougal, "Dynamic lithium-ion battery model for system simulation," *IEEE Transactions on Components and Packaging Technologies*, vol. 25, no. 3, pp. 495–505, Sep. 2002.

[69] X. Lin, A. G. Stefanopoulou, Y. Li, and R. D. Anderson, "State of charge estimation of cells in series connection by using only the total voltage measurement," in *2013 American Control Conference*, Jun. 2013, pp. 704–709.

[70] S. Moura, N. Chaturvedi, and M. Krstic, "PDE estimation techniques for advanced battery management systems – Part I: SOC estimation," in *American Control Conference (ACC), 2012*, Jun. 2012, pp. 559–565.

[71] M. Sitterly, L. Y. Wang, G. G. Yin, and C. Wang, "Enhanced identification of battery models for real-time battery management," *IEEE Transactions on Sustainable Energy*, vol. 2, no. 3, pp. 300–308, Jul. 2011.

[72] T. Coleman and Y. Li, "A reflective newton method for minimizing a quadratic function subject to bounds on some of the variables," *SIAM Journal on Optimization*, vol. 6, no. 4, pp. 1040–1058, Nov. 1996.

[73] L. J. Shrinkle, "United States Patent: 9315113 - Electric vehicle battery systems with exchangeable parallel electric vehicle battery modules," Patent 9 315 113, Apr., 2016.

[74] O. I. Elgerd, *Electric Energy Systems Theory: An Introduction*. McGraw-Hill Book Company, New York, NY, 1982.

[75] R. A. de Callafon and C. Wells, "Distributed realtime electric power grid event detection and dynamic characterization," in *Proc. of CIGRE US National Committee 2014 Grid of the Future Symposium*, 2014.

[76] P. Kundur, N. J. Balu, and M. G. Lauby, *Power System Stability and Control*. McGraw-hill New York, 1994, vol. 7.

[77] G. Rogers, *Power System Oscillations*. Boston, MA: Springer US, 2000.

[78] M. Hemmingsson, *Power System Oscillations - Detection, Estimation and Control*. Lund University, 2003.

[79] J. Hauer, C. Demeure, and L. Scharf, "Initial results in Prony analysis of power system response signals," *IEEE Transactions on Power Systems*, vol. 5, no. 1, pp. 80–89, Feb. 1990.

[80] D. Pierre, D. Trudnowski, and J. Hauer, "Identifying linear reduced-order models for systems with arbitrary initial conditions using Prony signal analysis," *IEEE Transactions on Automatic Control*, vol. 37, no. 6, pp. 831–835, Jun. 1992.

[81] J. J. Sanchez-Gasca and J. H. Chow, "Performance comparison of three identification methods for the analysis of electromechanical oscillations," *IEEE Transactions on Power Systems*, vol. 14, no. 3, pp. 995–1002, Aug. 1999.

[82] D. Trudnowski and J. Pierre, "Overview of algorithms for estimating swing modes from measured responses," in *IEEE Power Energy Society General Meeting, 2009. PES '09*, Jul. 2009, pp. 1–8.

[83] J. Rueda, C. Juarez, and I. Erlich, "Wavelet-based analysis of power system low-frequency electromechanical oscillations," *IEEE Transactions on Power Systems*, vol. 26, no. 3, pp. 1733–1743, Aug. 2011.

[84] H. Ghasemi, "On-line monitoring and oscillatory stability margin prediction in power systems based on system identification," 2006.

[85] D. N. Miller and R. A. de Callafon, "Identification of linear time-invariant systems via constrained step-based realization," in *16th IFAC Symposium on System Identification (SYSID)*, 2012.

[86] B. A. Francis and W. M. Wonham, "The internal model principle of control theory," *Automatica*, vol. 12, no. 5, pp. 457–465, Sep. 1976.

[87] J. C. Doyle and G. Stein, "Multivariable feedback design: Concepts for a classical/modern synthesis," *IEEE Trans. on Auto. Control*, pp. 4–16, 1981.

[88] M. Safonov, A. Laub, and G. Hartmann, "Feedback properties of multivariable systems: The role and use of the return difference matrix," *IEEE Transactions on Automatic Control*, vol. 26, no. 1, pp. 47–65, Feb. 1981.

[89] G. Stein and M. Athans, "The LQG/LTR procedure for multivariable feedback control design," *IEEE Transactions on Automatic Control*, vol. 32, no. 2, pp. 105–114, Feb. 1987.